Experimental studies on polarization correlations in hard x-ray Rayleigh scattering

seit 1558

Dissertation

zur Erlangung des akademischen Grades
doctor rerum naturalium (Dr. rer. nat.)

vorgelegt dem Rat der Physikalisch-Astronomischen Fakultät
der Friedrich-Schiller-Universität Jena

von Dipl.-Phys. Karl-Heinz Blumenhagen

geboren am 30. September 1985 in Frankfurt a.M.

Gutachter

1. Prof. Dr. Thomas Stöhlker, Friedrich-Schiller-Universität Jena
2. Prof. Dr. Reinhard Dörner, Goethe-Universität, Frankfurt am Main
3. Prof. Dr. Christian Enss, Universität Heidelberg

Tag der Disputation: 5. Juli 2016

Contents

1 Introduction

Elastic photon scattering is one of the fundamental interactions between electromagnetic radiation and matter. While this already makes it an interesting subject for investigations, a detailed understanding of elastic scattering is essential for a variety of applications such as medical diagnostics [1–4], materials science [5], structure analysis of complex systems like molecules [6] or nano particles [7] and also in industry [8]. When small structures are probed by means of scattering, the wavelength of the photons to be scattered should be on the order of the size of the structure [9]. If atoms or other objects at that length scale are investigated, one needs to use photons in the hard x-ray regime and even smaller systems such as nuclei require γ-rays as a probe. It has therefore been of particular interest in the past decades to study elastic scattering at such high photon energies.

A common approach to describe elastic photon–atom scattering is to write the total scattering amplitude A as a coherent sum of individual amplitudes which correspond to scattering from different constituents of the atom [10]. For low energies from a few keV to about 1 MeV, Rayleigh scattering – the scattering from bound electrons – is the dominant contribution. This process was named after J. W. Strutt, Lord Rayleigh III, who published a theory of light scattering by small particles already in 1871 and used this to explain the blue sky and red sunsets [11–13]. While this is quite a famous example of elastic scattering, it was pointed out recently, that it is in fact not the primary reason for the blue sky – more important aspects are the higher sensitivity of the human eye to blue and the maximum of the solar spectrum in that wavelength region [14]. When the photon energy is increased above 1 MeV, Rayleigh scattering remains important, but only for forward scattering angles. In addition, contributions related to the nucleus arise. Delbrück scattering denotes the scattering from virtual electron-positron pairs that are created in the atomic field (which corresponds to the nuclear field when screening is neglected). The process was named after M. Delbrück who proposed it as a comment in [15]. It is of particular interest as it is one of the nonlinear QED[1] processes that are predicted as a consequence of the vacuum polarization [16]. It is relatively well accessible experimentally – compared to the related processes, which are light-light scattering [17–19], photon splitting in

[1] Quantum Electrodynamics

an external field [20, 21] and photon coalescence in an external field [22]. Delbrück scattering has been found in experiments at energies as low as 889 keV [23] and it is the dominant elastic scattering process above ≈ 100 MeV [24]. At photon energies of several MeV, elastic scattering can also occur from the nucleus. This is usually partitioned into nuclear Thomson scattering where the nucleus is considered as a structureless point charge [25] and nuclear resonance scattering which is related to the excitation of nuclear levels [26, 27].

The most common way to investigate elastic photon scattering experimentally is the measurement of the angle-differential cross section, which is theoretically described as the square of the absolute value of the amplitude A. As the different contributions to the elastic scattering process cannot be distinguished and therefore their amplitudes are added (rather than their cross sections), disentangling them in an experiment is difficult. But since their relative strengths depend on the photon energy $\hbar\omega$, the scattering angle θ and the target nuclear charge Z, a proper choice of these parameters allows to some extent to study the individual processes separately. Furthermore, destructive interference between some contributions may lead to near isolation of the remaining one(s), examples of experiments exploiting this are given in the extensive review paper by Kane *et al.* [28], which generally provides a detailed discussion of elastic scattering and a large source of further references. For more recent results, see for example the review by Bradley *et al.* [29], a validation of the Monte Carlo code Geant4 [30] against experimental data by Batič *et al.* [31] and an exhaustive bibliography about Delbrück scattering by Hubbel and Bergstrom [32].

The majority of the experiments was performed with radioactive sources which usually emit unpolarized photons. Additional information on the elastic scattering process can be obtained when polarization effects are taken into account. This is true not only for elastic scattering, but also for the investigation of other fundamental processes that involve the emission of hard x-rays, for example REC[2] [33–38] or fluorescence [39, 40]. Another important application of x-ray polarization measurements lies in astrophysics, where such studies provide information about non-thermal emission processes, see for example [41–43]. As x-ray polarization measurements require a lot of photons, they are restricted to bright sources such as the crab [44–49].

[2]Radiative electron capture

Elastic scattering experiments with polarized hard x-rays were up to now limited due to technological shortcomings: sources of polarized hard x-rays were not intense and polarimeters not efficient enough, so that polarization measurements in that energy region generally suffered from low statistics. Experiments were therefore restricted to the following scenarios: (i) Measurement of the differential cross section when the incident beam is polarized. In the early studies [50–52] a partially (linearly) polarized beam was prepared via Compton scattering of an unpolarized beam from an auxiliary target and the asymmetry ratio between the intensities of photons scattered in and perpendicular to the scattering plane was measured. With the advent of synchrotron radiation sources, experiments with highly (linearly) polarized photon beams were carried out where absolute differential cross sections were determined [53, 54]. (ii) Measurement of the linear polarization of elastically scattered photons when the incident beam is unpolarized. The early experiments employed simple Compton polarimeters that analyzed the elastically scattered photons. They consisted of counters that measured the intensities of secondary Compton-scattered photons – in and perpendicular to the primary (elastic) scattering plane. Some papers quoted directly the measured intensity ratio [55–57], others converted it into the degree of linear polarization of the elastically scattered photons [58–62]. In addition to these scenarios which consider linear polarization effects, there were also experiments investigating circular polarization. Such studies usually require (spin-) oriented scattering targets and they are referred to as magnetic scattering [63] – a topic on its own, which is explicitly excluded in the present study.

In this thesis, a new type of experiment is presented that was not performed before: elastic scattering of highly linearly polarized hard x-rays with a linear polarization measurement of the scattered photons. The simultaneous control of the polarization state of the incident and scattered photons allows a more detailed investigation than previous experiments (where only one of the two was measured). Attention is paid in particular to relativistic effects. They are expected to most be pronounced for 90°-scattering in the polarization plane of the incident beam, as this scenario is forbidden in the non-relativistic dipole approximation. In a relativistic calculation, higher-order multipoles are taken into account, which leads to a finite scattering cross section for all angles. It is still expected to be small at 90°, which makes a measurement challenging – in particular of the polarization of the scattered beam.

Therefore a setup is chosen where relativistic effects are pronounced: a high-Z scatterer (gold, $Z = 79$) and a high photon energy $\hbar\omega = 175$ keV. The latter is available (linearly polarized with sufficient intensity) at the third-generation synchrotron radiation source PETRA III[3] at DESY[4], Hamburg. For a linear polarization measurement at that energy, a lithium-drifted silicon strip detector designed as a dedicated hard x-ray Compton polarimeter is employed. The combination of these state-of-the-art technologies (radiation source and polarimeter) enables this experiment where one can observe a "polarization transfer". In that sense it is similar to previous studies where the linear polarization of bremsstrahlung photons originating from spin-polarized electrons was measured [64–69]. For both elastic scattering and bremsstrahlung, the polarization transfer may also be applied in an inverse way: with an established theory of the interaction process and a measured polarization of the emitted photons one can reconstruct the polarization of the incident beam (electrons or photons). Such a scheme would provide a sensitive diagnostic tool for polarized beams of the corresponding particles and results for bremsstrahlung were already published [70, 71]. A similar method was also proposed for spin-polarized ion beams, in that case using the REC process as a probe [72]. The latter would be in particular relevant for the new FAIR[5] facility [73] that is currently being built at GSI[6], Darmstadt. The theory for elastic scattering in the present study can be reduced to the theory for Rayleigh scattering, as that is the dominant elastic process at 175 keV. With the new experimental possibilities regarding polarization effects in elastic scattering, several theoretical studies in that matter appeared. A relativistic framework based on the Dirac equation was employed to study effects related to both linear and circular polarization for atomic and also ionic targets [74–79]. The methods described in these papers were applied by A. Surzhykov, V. A. Yerokhin and S. Fritzsche to provide predictions to which the experimental data of the present study are compared. It shall also be mentioned that the same authors are involved in a recently started rigorous treatment of the electron-electron interaction [80], but results from that are not incorporated in the present thesis which is structured as follows:

In chapter 2, the main physical concepts that are important for this study are pre-

[3]Positron-Electron-Tandem Ring Accelerator
[4]Deutsches Elektronensynchrotron
[5]Facility for Antiproton and Ion Research
[6]GSI Helmholtzzentrum für Schwerionenforschung GmbH

sented. These include fundamental photon-matter interactions that are relevant in the conducted experiment, among them the subject of this study, namely elastic photon scattering and in particular Rayleigh scattering. Inelastic (Compton) scattering also plays an important role, as it is the analyzing process in the polarization measurements and it is used to diagnose the linear polarization of the incident beam. In addition to the fundamental processes, the basic principles of the detection systems (semiconductor detectors) and the synchrotron radiation source are outlined.

Polarization effects are described in chapter 3. Stokes parameters are introduced to characterize the polarization of a photon beam. Scattering is treated with the transfer matrix formalism, which is discussed for the special cases of Compton- and Rayleigh scattering.

Chapter 4 covers the experimental setup. Brief descriptions of the environment at the photon source PETRA III and of the used detectors are given. The setup is discussed in terms of geometry and data acquisition. An overview is given of the auxiliary measurements as well as of the parameters for the main experimental runs.

Chapter 5 provides a detailed description of the applied analysis procedures. The first step is the analysis of individual events which defines how spectra are filled. From these spectra, the final results, namely the differential cross section and the linear polarization of the scattered photons are extracted in a second step. The measured polarizations serve as input for a third step, where the polarization of the incident beam is reconstructed.

The results of the experiment are presented and discussed in chapter 6 and a summary is given in chapter 7. The thesis closes with an outlook to possible future studies in chapter 8.

2 Physical background

This chapter gives an overview of the relevant physical concepts of the present thesis. Section 2.1 describes fundamental photon-matter interactions, whereas sections 2.3 and 2.4 discuss the physics of the detection systems and the photon source, respectively.

2.1 Interaction between photons and matter

In this thesis, the relevance of photon-matter interactions is twofold: while elastic scattering is the subject that is investigated, other processes such as Compton scattering and photoabsorption are relevant for the applied measurement techniques. In this section, the main characteristics of each process are presented. The cross sections of the individual processes (in gold) are shown in figure 2.1.

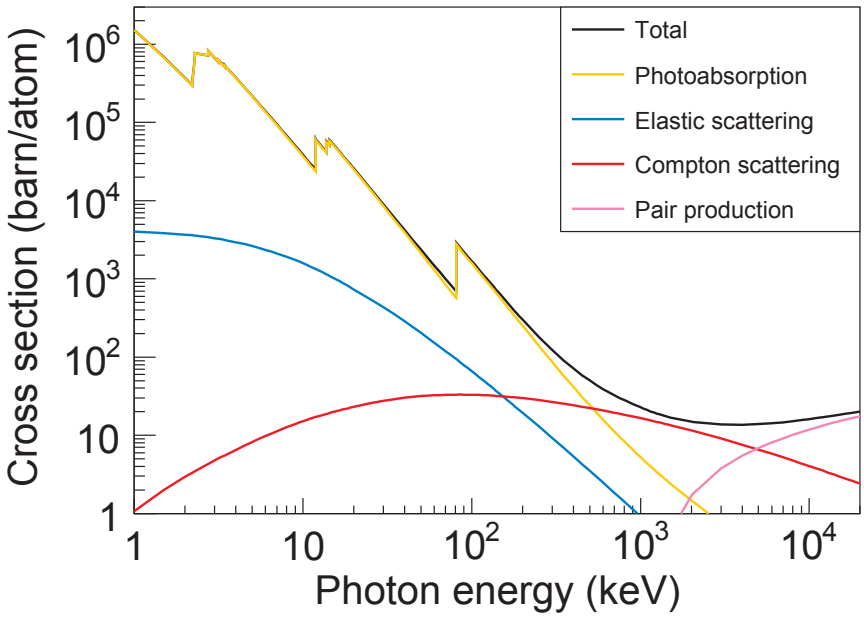

Figure 2.1: Cross sections for interactions of x-rays with gold. Data are taken from [81].

2.1.1 Photoelectric effect

The photoelectric effect (or photoabsorption) describes an interaction, where a photon transfers its entire energy $\hbar\omega$ to an electron. Due to momentum conservation, this process is only possible for bound electrons (for example by an atom). If the photon energy exceeds the (negative) binding energy E_b, the electron leaves the atom with a kinetic energy

$$E_{kin} = \hbar\omega + E_b. \tag{2.1}$$

For photon energies below this threshold the atom can be excited through the absorption of the photon. As can be seen in figure 2.1, the cross section decreases with increasing photon energy. At lower energies, also resonant structures appear. These so-called absorption edges are at the binding energies of the innermost atomic shells. If the photon energy decreases below such a binding energy, the electrons in the corresponding shell cannot contribute to the absorption cross section anymore, which results in a steep decrease. Going from higher to lower energies, one has the K-edge at $-E_K$, the L-edge at $-E_L$, etc.. For the energy region $-E_K \ll \hbar\omega \ll m_e c^2$ the Born approximation can be applied to calculate the photoabsorption cross section as [82]

$$\sigma_{photo} = \sigma_T \cdot 4\sqrt{2}\alpha^2 \cdot Z^5 \cdot \left(\frac{m_e c^2}{\hbar\omega}\right)^{\frac{7}{2}}. \tag{2.2}$$

The quantities appearing here are the nuclear charge Z, the fine structure constant $\alpha \approx 1/137$, the vacuum speed of light c, the electron rest energy $m_e c^2 \approx 511$ keV and the Thomson cross section $\sigma_T = 8\pi/3 \cdot r_e^2 \approx 0.665$ barn with the classical electron radius $r_e = e^2/(4\pi\varepsilon_0 m_e c^2) \approx 2.8 \cdot 10^{-13}$ cm which contains the elementary charge $e \approx 1.602 \cdot 10^{-19}$ C and the electric constant $\varepsilon_0 \approx 8.85 \cdot 10^{-12}$ C/(Vm). In this thesis, photoabsorption is a relevant process for x-ray detection and shielding. In both cases, a large cross section increases the efficiency and therefore materials with higher nuclear charge Z are favored. Common choices are lead ($Z = 82$) for shielding and germanium ($Z = 32$) for energy-dispersive semiconductor detectors (see section 2.3). For Compton polarimetry (see section 5.1.2) a large cross section for both photoabsorption and Compton scattering is required. For an optimization of the efficiency one has to find a compromise which depends on the photon energy. In this thesis, silicon ($Z = 14$) was used as the active material of the polarimeter

(see section 4.2.2).

2.1.2 Compton scattering

Inelastic scattering of photons from free electrons is referred to as Compton scattering, named after A. H. Compton who discovered the effect [83]. For the following description of the process, photon energies are expressed in units of $m_e c^2$:

$$k := \frac{\hbar\omega}{m_e c^2}, \qquad k' := \frac{\hbar\omega'}{m_e c^2}. \tag{2.3}$$

Quantities with a prime correspond to the scattered photon. Let θ be the angle between the propagation directions of the scattered and the incident photon. The energy of the scattered photon is then given by [84]

$$k' = \frac{k}{1 + k \cdot (1 - \cos(\theta))}. \tag{2.4}$$

The recoil electron gains kinetic energy

$$\Delta k = k - k'. \tag{2.5}$$

The differential cross section for Compton scattering, which depends on the initial and final photon polarizations and electron spins, was calculated within the QED framework by O. Klein and Y. Nishina [85]. For an initially (on average) unpolarized electron and a linearly polarized photon and when neither the final electron spin nor the final photon polarization are observed, the double-differential Klein-Nishina cross section reads

$$\left(\frac{\mathrm{d}\sigma}{\mathrm{d}\Omega}\right)_{KN} = \frac{r_e^2}{2} \cdot \left(\frac{k'}{k}\right)^2 \cdot \left(\frac{k'}{k} + \frac{k}{k'} - 2\sin^2(\theta)\cos^2(\varphi)\right). \tag{2.6}$$

In addition to the (polar) scattering angle θ, this cross section also depends on the azimuthal scattering angle φ, which is the angle between the scattering plane and the polarization direction of the incident photon. An illustration of the involved angles is shown in figure 2.2.
For an unpolarized photon beam, the cross section only depends on θ, as equation 2.6 is averaged over φ, which leads to the substitution $\cos^2(\varphi) \to \frac{1}{2}$. In the present thesis, equation 2.6 is not sufficient, as it describes neither the scattering of partially polarized photon beams nor the polarization of the scattered photons. The required

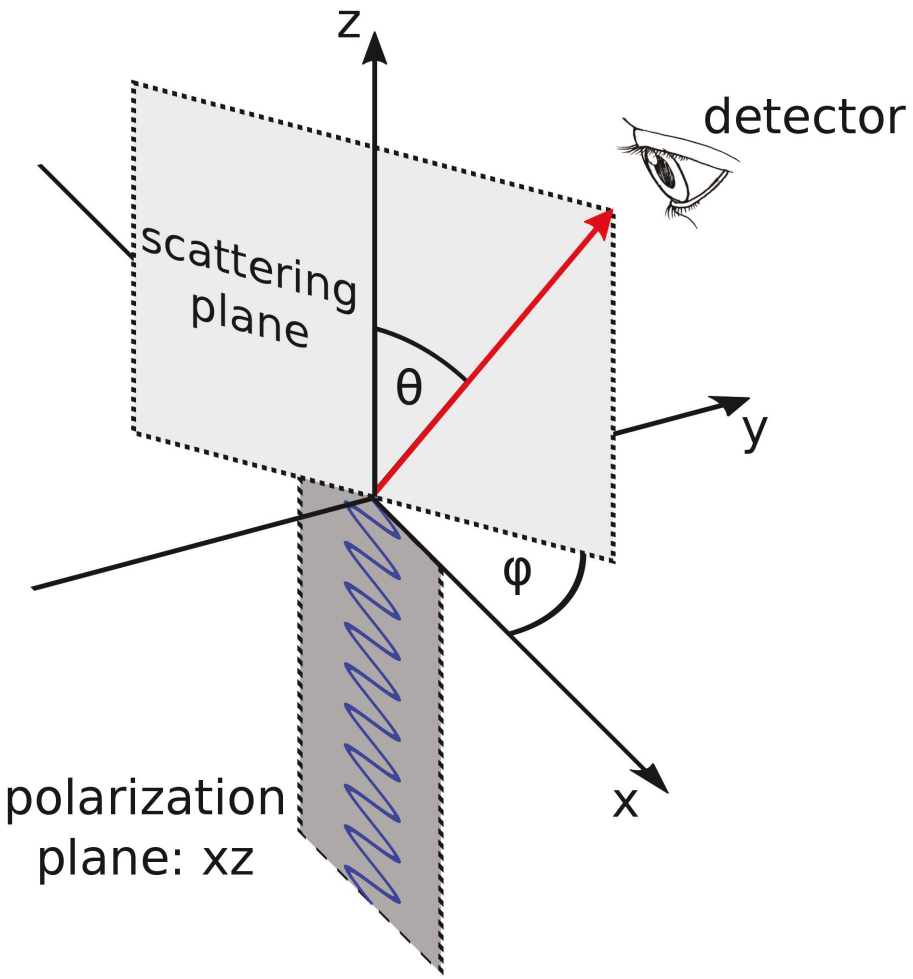

Figure 2.2: Geometry of Compton scattering: the incident photon (blue wavy line) is linearly polarized in the xz-plane and propagates in z-direction. It is scattered from a free electron at rest in the origin. The direction of the scattered photon (red arrow) is given by the polar angle θ and the azimuthal angle φ.

extensions to cover also these scenarios are discussed in chapter 3.

The considerations up to now are strictly valid only for the ideal case of free electrons. Inelastic scattering from bound electrons introduces two additional effects:

1. If the polar scattering angle θ is such, that the energy of the recoil electron given by equation 2.5 is below the binding energy of a certain atomic shell, electrons in that shell cannot contribute to Compton scattering at that angle [86]. But the energy transferred from the photon can still be enough to excite the atom, this process is usually referred to as Raman scattering [87].

2. At a given polar scattering angle θ, the energy of the scattered photon is not strictly defined by equation 2.4 because the electron moves according to the momentum distribution defined by its atomic state. This results in a Doppler-broadened energy spectrum which is described by the cross section $\frac{\mathrm{d}^2\sigma}{\mathrm{d}\Omega\mathrm{d}(\hbar\omega')}$ that is differential in θ, φ and $\hbar\omega'$.

Let $\hbar\omega_c$ be the energy of the scattered photon given by equation 2.4. The maximum of $\frac{\mathrm{d}^2\sigma}{\mathrm{d}\Omega\mathrm{d}(\hbar\omega')}$ is roughly at $\hbar\omega_c$, but for scattering from strongly bound (inner-shell) electrons, there may be a substantial shift, the so-called Compton defect [86], which is particularly pronounced for high-Z targets. On the other hand, such (neutral) targets have more electrons that can contribute to Compton scattering, so that the relative importance of the inner shells decreases. For loosely bound electrons, one can apply the impulse approximation [88, 89], which gives a good description of $\frac{\mathrm{d}^2\sigma}{\mathrm{d}\Omega\mathrm{d}(\hbar\omega')}$ in the peak region – the relevant region in the present thesis ($\hbar\omega_c \pm 5$ keV). In [89], it is shown, that within the impulse approximation, a single-differential cross section proportional to the Klein-Nishina cross section is obtained when $\frac{\mathrm{d}^2\sigma}{\mathrm{d}\Omega\mathrm{d}(\hbar\omega')}$ is integrated over the entire $\hbar\omega'$-range. The proportionality factor is the incoherent scattering function $S(q, Z)$ [89–92], which depends on the target material and the momentum transfer

$$\boldsymbol{q} = \boldsymbol{k}' - \boldsymbol{k}, \qquad q = |\boldsymbol{q}|. \tag{2.7}$$

In the present thesis, $\frac{\mathrm{d}^2\sigma}{\mathrm{d}\Omega\mathrm{d}(\hbar\omega')}$ is not integrated over the entire $\hbar\omega'$-range, but only over the small window (± 5 keV) around $\hbar\omega_c$. Using the same procedures as in [89], this integration leads again to a single-differential cross section proportional to the Klein-Nishina cross section. For the purposes of this thesis, only the angular dependence of the proportionality factor is relevant (not its absolute magnitude), but it was found to be negligible.

2.1.3 Rayleigh scattering and other elastic photon scattering processes

When a photon scatters elastically from a target, it does not change its energy in the process. This is strictly true only in the center-of-mass frame, but if the photon energy is less than some 10 MeV and scattering from atoms is considered, the distinction between center-of-mass and laboratory frame can safely be ignored [93]. Elastic scattering from a free electron is called Thomson scattering. If an atomic

system is considered, the photon can scatter from bound electrons, which is then referred to as Rayleigh (R) scattering. Other contributions, that add coherently to elastic photon-atom scattering, are nuclear Thomson- (NT), nuclear resonance- (NR) and Delbrück (D) scattering. With this partition, the total (complex) amplitude A, which describes the scattering process, reads:

$$A = A^{(R)} + A^{(NT)} + A^{(NR)} + A^{(D)}. \tag{2.8}$$

The amplitude is normalized, such that

$$\frac{\mathrm{d}\sigma}{\mathrm{d}\Omega} = |A|^2 . \tag{2.9}$$

As shown in [28], the amplitude A for arbitrary polarizations of the incident and scattered photon can be resolved into the invariant (polarization-independent) amplitudes $A_\parallel$ and $A_\perp$ which correspond to the scattering of photons that are linearly polarized in the scattering plane and perpendicular to it, respectively. The magnitudes of these amplitudes for the individual coherent contributions are shown in figure 2.3 for the experimental conditions of this thesis: a photon energy $\hbar\omega = 175$ keV and gold as a scatterer, $Z = 79$. It is clear from figure 2.3 that for the scenario con-

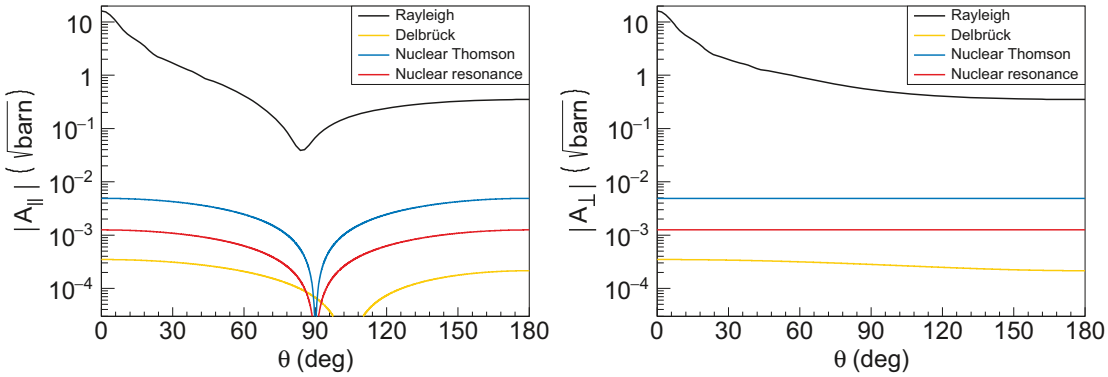

(a) (b)

Figure 2.3: Magnitudes of the complex invariant amplitudes $A_\parallel$ (a) and $A_\perp$ (b) for $Z = 79$ and $\hbar\omega = 175$ keV. See text for details on the corresponding references.

sidered in this thesis, Rayleigh scattering is dominant. The other processes can be neglected and they are therefore only described briefly in the remainder of this section, for more details see [28].

Thomson scattering

The elastic scattering scattering of a photon from a free point charge without internal structure is called Thomson scattering, named after J. J. Thomson who first described this process [94]. The classical result for the scattering cross section with linearly polarized incident radiation and an electron as a scatterer reads

$$\left(\frac{\mathrm{d}\sigma}{\mathrm{d}\Omega}\right)_T = r_e^2 \cdot \left(1 - \sin^2(\theta)\cos^2(\varphi)\right), \tag{2.10}$$

which is the low energy limit ($\hbar\omega \ll m_e c^2$, $k' \to k$) of the Klein-Nishina cross section 2.6.

Rayleigh scattering

When considering elastic photon scattering from an atomic target, the dominant contribution comes from scattering off bound electrons for photon energies up to ≈ 1 MeV. This process was investigated since the 1930s [95] and named after J. W. Strutt, Lord Rayleigh III, who had published pioneering work about light scattering by small particles [11–13]. A simple approach to describe scattering from bound electrons is the form factor approximation [90, 96, 97] which extends scattering from a point charge (Thomson) to scattering from a charge distribution:

$$\frac{\mathrm{d}\sigma}{\mathrm{d}\Omega} = \left(\frac{\mathrm{d}\sigma}{\mathrm{d}\Omega}\right)_T \cdot |f(\boldsymbol{q})|^2, \tag{2.11}$$

where $\boldsymbol{q}$ is again the momentum transfer defined in equation 2.7. The form factor $f(\boldsymbol{q})$ is the Fourier transform of the charge distribution of the atom $\rho(\boldsymbol{r})$:

$$f(\boldsymbol{q}) = \int \rho(\boldsymbol{r}) \ \exp(i\boldsymbol{q}\boldsymbol{r}) \ \mathrm{d}^3 r. \tag{2.12}$$

If Z electrons are present in the system, they are treated as individual constituents and therefore their scattering amplitudes (and with this their form factors) are added coherently:

$$f(\boldsymbol{q}) = \sum_{j=1}^{Z} f_j(\boldsymbol{q}), \tag{2.13}$$

where $f_j(\boldsymbol{q})$ is the form factor of the j^{th} electron. The individual form factors correspond to individual charge distributions ρ_j which are normalized to 1. The

total charge distribution is therefore normalized to Z. For spherical-symmetric charge distributions, f becomes independent of the direction of $\boldsymbol{q}$:

$$f(q) = 4\pi \int \rho(r) \, \frac{\sin(qr)}{qr} r^2 \, \mathrm{d}r. \tag{2.14}$$

Different variations of the form factor approximation and their regions of validity are reviewed in [93, 98]. The simple form factor given by equation 2.14 does not describe the differential cross section well for large angles, especially for high-Z elements and at higher energies [98]. It is therefore not suitable for the scenario considered in the present thesis, but it provides some qualitative insights about the cross section dependence on photon energy, scattering angle and target Z: the function $\sin(qr)/(qr)$ is ≈ 1 for $qr \ll 1$ and decreases to 0 for larger qr. The r-region (near $r = 0$), where $\sin(qr)/(qr)$ is non-negligible, decreases for higher q, i.e. for higher photon energies and larger scattering angles. For these cases only inner-shell electrons contribute to $f(q)$ as their $\rho(r)$ is non-zero for small r. For small angles where $q \to 0$, the form factor of each electron f_j becomes 1. Therefore the form factor of a certain shell is then equal to the number of electrons in that shell. Higher shells with more electrons provide the dominant contribution to the total form factor when the scattering angle is small enough. If neutral systems are considered, an increase of Z leads to an increase of the total number of electrons and therefore an increase of the form factor. But this argument is only valid for small momentum transfers, as otherwise only the K-shell electrons contribute significantly. On the other hand, K-shell electrons in higher-Z systems are bound more closely to the nucleus, which also leads to an increase of the form factor.

In the language of quantum electrodynamics, Rayleigh scattering can be considered as the special case of a bound-bound transition from an initial state $|i\rangle$ via a virtual intermediate state $|\nu\rangle$ to a final state $|f\rangle$, where the energies of the initial and final state E_i and E_f are equal. This is illustrated in figure 2.4. For comparison, also another example of a bound-bound transition – the two photon decay – is shown. The latter process has been treated within the same theoretical framework [99, 100] which will be outlined in the following for Rayleigh scattering.

In current state-of-the-art calculations, Rayleigh scattering is treated perturbatively to second order within the relativistic QED framework. This technique was first applied by G. E. Brown and his group [101–105]. For later improvements, see for example [10] and references therein. The predictions that appear in the present thesis were provided by A. Surzhykov, V. A. Yerokhin and S. Fritzsche [106]. For

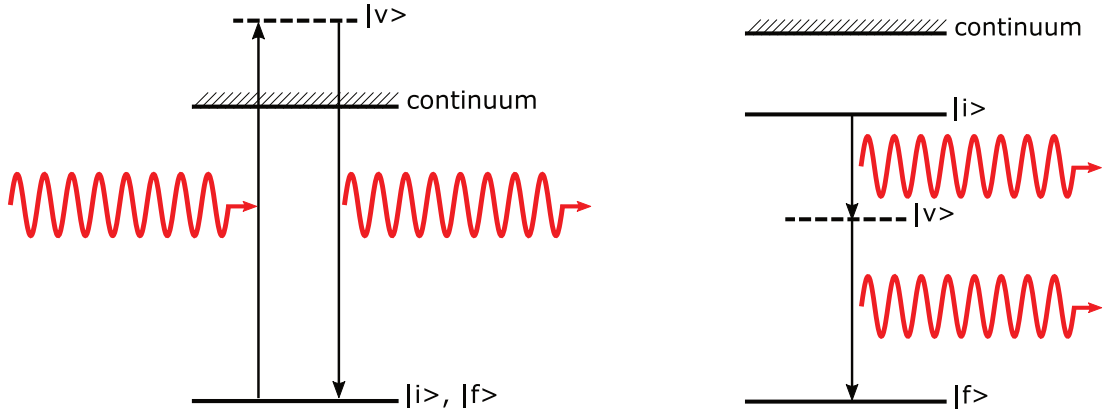

Figure 2.4: Illustration of bound-bound transitions Rayleigh scattering (a) and two-photon decay (b). In both cases, the transition is between (real) bound states $|i\rangle$ and $|f\rangle$ via a (virtual) intermediate state $|\nu\rangle$.

details on the calculation methods, see their publications [77, 79] and references therein. The second order transition amplitude (S-matrix element) $A^{(R)} = \mathcal{M}_{if}$ between the (many-electron) states $|i\rangle$ and $|f\rangle$ depends on the wave vectors $\boldsymbol{k}$, $\boldsymbol{k}'$ and polarizations $\boldsymbol{\epsilon}$, $\boldsymbol{\epsilon}'$ of the incident and outgoing photon. It can be written as a sum of two contributions which correspond to the Feynman diagrams shown in figure 2.5:

$$\mathcal{M}_{if}(\boldsymbol{k},\boldsymbol{\epsilon},\boldsymbol{k}',\boldsymbol{\epsilon}') = \mathcal{M}^{+}_{if}(\boldsymbol{k},\boldsymbol{\epsilon},\boldsymbol{k}',\boldsymbol{\epsilon}') + \mathcal{M}^{-}_{if}(\boldsymbol{k},\boldsymbol{\epsilon},\boldsymbol{k}',\boldsymbol{\epsilon}'), \tag{2.15}$$

$$\mathcal{M}^{+}_{if}(\boldsymbol{k},\boldsymbol{\epsilon},\boldsymbol{k}',\boldsymbol{\epsilon}') = \sum_{\nu} \frac{\langle f|\,\hat{\mathcal{R}}^{\dagger}(\boldsymbol{k}',\boldsymbol{\epsilon}')\,|\nu\rangle\,\langle\nu|\,\hat{\mathcal{R}}(\boldsymbol{k},\boldsymbol{\epsilon})\,|i\rangle}{E_i - E_\nu + \hbar\omega}, \tag{2.16}$$

$$\mathcal{M}^{-}_{if}(\boldsymbol{k},\boldsymbol{\epsilon},\boldsymbol{k}',\boldsymbol{\epsilon}') = \sum_{\nu} \frac{\langle f|\,\hat{\mathcal{R}}(\boldsymbol{k},\boldsymbol{\epsilon})\,|\nu\rangle\,\langle\nu|\,\hat{\mathcal{R}}^{\dagger}(\boldsymbol{k}',\boldsymbol{\epsilon}')\,|i\rangle}{E_i - E_\nu - \hbar\omega}, \tag{2.17}$$

$$\hat{\mathcal{R}}(\boldsymbol{k},\boldsymbol{\epsilon}) = \boldsymbol{\alpha}\boldsymbol{\epsilon}\cdot\exp(i\boldsymbol{k}\boldsymbol{r}). \tag{2.18}$$

The transition operators $\hat{\mathcal{R}}$, $\hat{\mathcal{R}}^{\dagger}$ describe the absorption and emission of a photon, respectively. The quantity $\boldsymbol{\alpha}$ denotes the vector of Dirac matrices [107]. In this form of $\mathcal{M}_{if}$, all quantum numbers of the initial and final state need to be specified. A simplification commonly made is the independent particle approximation (IPA) which allows to rewrite equations 2.16 and 2.17 as sums over single-electron states [93]. This approximation works well for high photon energies (well above the K-shell ionization threshold) and heavy targets [108]. In a recent theoreti-

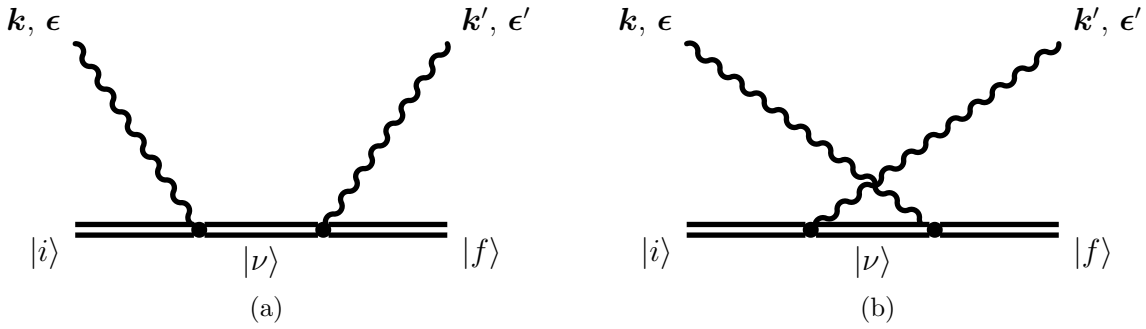

Figure 2.5: Lowest order Feynman diagrams for Rayleigh scattering. (a) Absorption first ($\mathcal{M}_{if}^{+}$). (b) Emission first ($\mathcal{M}_{if}^{-}$). Time axis is from left to right.

cal study, beyond-IPA effects were investigated with a rigorous treatment of the electron-electron interaction in helium-like ions [80].
From the S-matrix element, the cross section is obtained as

$$\left(\frac{\mathrm{d}\sigma}{\mathrm{d}\Omega}\right)_{if}(\boldsymbol{k},\boldsymbol{\epsilon},\boldsymbol{k}',\boldsymbol{\epsilon}') = \left|\mathcal{M}_{if}(\boldsymbol{k},\boldsymbol{\epsilon},\boldsymbol{k}',\boldsymbol{\epsilon}')\right|^2 . \tag{2.19}$$

In the present thesis, only unpolarized targets are considered, which means that one has to average equation 2.19 over the initial total angular momentum projection M_i. Also, the same quantity in the final state, M_f, is not observed, which leads to a summation over M_f of equation 2.19. With these steps, the total Rayleigh cross section reads

$$\frac{\mathrm{d}\sigma}{\mathrm{d}\Omega}(\boldsymbol{k},\boldsymbol{\epsilon},\boldsymbol{k}',\boldsymbol{\epsilon}') = \frac{1}{2J_i+1}\sum_{M_i,M_f}\left(\frac{\mathrm{d}\sigma}{\mathrm{d}\Omega}\right)_{if}(\boldsymbol{k},\boldsymbol{\epsilon},\boldsymbol{k}',\boldsymbol{\epsilon}'), \tag{2.20}$$

where J_i is the total angular momentum of the initial state $|i\rangle$.

Delbrück scattering

The elastic scattering of photons from electron-positron pairs, that are created in the Coulomb field of a nucleus, is referred to as Delbrück scattering (see figure 2.6 for illustration). This nonlinear QED effect as a consequence of the vacuum polarization was predicted by M. Delbrück as a comment in [15]. An overview of experimental and theoretical results is given in [109]. Delbrück scattering is closely related to other nonlinear QED effects, namely light-light scattering [17–19], photon splitting in an external field [20, 21] and photon coalescence in an external field [22]. The similarity of these processes can be seen by comparing their Feynman diagrams

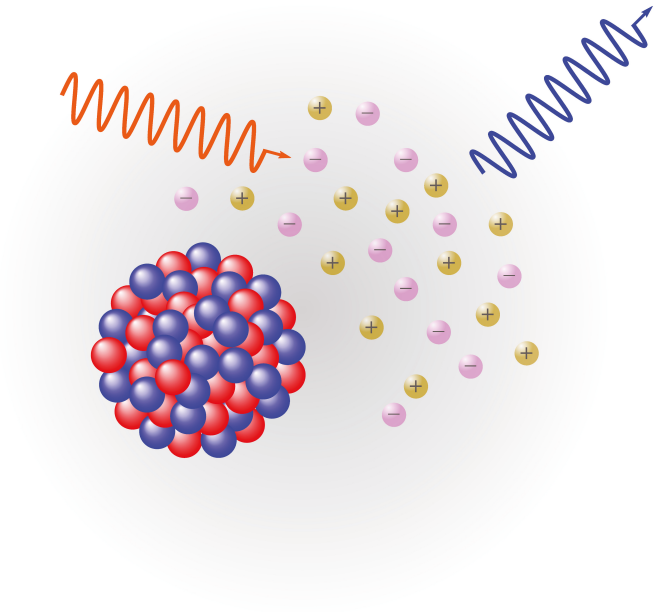

Figure 2.6: Illustration of Delbrück scattering. A photon scatters from virtual electron-positron pairs which are created in a nuclear field.

which are shown in figure 2.7 [110]. The relative importance of Delbrück scattering

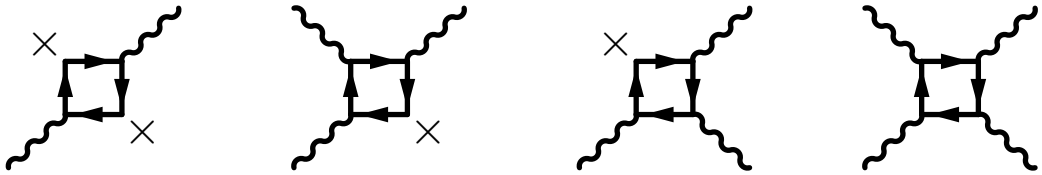

Figure 2.7: Feynman diagrams for nonlinear QED processes. (a) Delbrück scattering. (b) Photon coalescence. (c) Photon splitting. (d) Photon-photon scattering. Time axis is from left to right.

for the present thesis is estimated from the analytical amplitudes given in [24]:

$$A_{\parallel}^{(D)} = (Z\alpha)^2 \cdot r_e \cdot \left(\frac{\hbar\omega}{m_e c^2}\right)^2 \cdot \frac{14 + 59 \cdot \cos(\theta)}{72 \cdot 32}, \tag{2.21}$$

$$A_{\perp}^{(D)} = (Z\alpha)^2 \cdot r_e \cdot \left(\frac{\hbar\omega}{m_e c^2}\right)^2 \cdot \frac{59 + 14 \cdot \cos(\theta)}{72 \cdot 32}.$$

A good accuracy cannot necessarily be expected for $\hbar\omega = 175$ keV, as the amplitudes 2.21 were derived for the low-energy limit $\hbar\omega \ll m_e c^2$. They shall only serve as a rough estimate to demonstrate that Delbrück scattering can be neglected in this

thesis (see figure 2.3).

Nuclear Thomson scattering

For low energies, scattering from the nucleus can be treated as scattering from a point charge Ze with mass M_{nucl}. The differential cross section can be obtained from the Thomson scattering cross section 2.10 by applying the following substitutions in r_e:

$$m_e \to M_{nucl}, \qquad e \to Ze. \tag{2.22}$$

The process is therefore called nuclear Thomson scattering. Effects from a finite nuclear size can be taken into account using a (nuclear) form factor similar to 2.11. In [25], nuclear Thomson scattering was measured in a scenario where it was the dominant contribution to the elastic scattering cross section ($E = 5.5$ to 7.2 MeV, low-Z, $\theta = 140°$). For heavy elements and energies below 500 keV, nuclear Thomson scattering is not important [98], therefore also not in the present thesis, as can be seen in figure 2.3.

Nuclear resonance scattering

For photon energies above several MeV, internal degrees of the nucleus can be excited. The scattering process associated with such excitations is referred to as nuclear resonance scattering [26, 27]. The amplitudes for this process can be parametrized with the GDR[1] parameters σ_j, E_j and Γ_j [111]:

$$\begin{aligned} A_{\perp}^{(NR)} &= \frac{(\hbar\omega)^2}{4\pi\hbar c} \cdot \sum_{j=1}^{n} \sigma_j \Gamma_j \cdot \frac{E_j^2 - (\hbar\omega)^2}{(E_j^2 - (\hbar\omega)^2)^2 + (\hbar\omega)^2 \Gamma_j^2}, \\ A_{\parallel}^{(NR)} &= A_{\perp}^{(NR)} \cdot \cos(\theta). \end{aligned} \tag{2.23}$$

The sum in 2.23 runs to $n = 1$ for spherical and to $n = 2$ for deformed nuclei. Estimations for this thesis are obtained with the GDR parameters from [112, 113]. They are shown in figure 2.3 and indicate that nuclear resonance scattering can be neglected here.

[1] Giant dipole resonance

2.1.4 Pair production

For photon energies above $2m_ec^2$, electron-positron pairs can be created. Momentum conservation requires that a third partner is present in the reaction. This can be a nucleus, but an electron is also possible. In the latter case the energy threshold is $4m_ec^2$ and the process is referred to as triplet production [114]. For this thesis, pair and triplet production are not relevant and only mentioned for completeness.

2.2 Atomic de-excitation processes

When an electron is removed from an inner atomic shell (for example by photoionization, see section 2.1.1), the system is in an excited state. Subsequent de-excitation can occur either radiatively (fluorescence) or non-radiatively (Auger decay). These two processes are illustrated in figure 2.8. In a characteristic transition (fluorescence

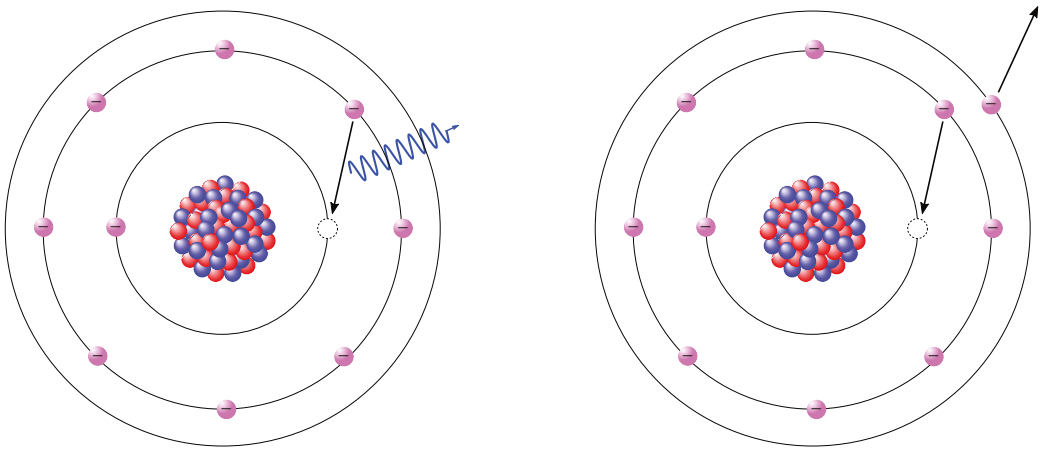

(a) (b)

Figure 2.8: Atomic de-excitation processes. (a) Fluorescence. (b) Auger decay.

radiation), an inner-shell vacancy is filled by an electron from a higher shell in combination with the emission of a photon, therefore it is a radiative process. If the transition is from an initial state $|i\rangle$ to a final state $|f\rangle$, the energy of the emitted photon is given by

$$\hbar\omega = E_i - E_f. \tag{2.24}$$

The differential probability for the emission of a photon into the solid angle $\mathrm{d}\Omega$ is [115]:

$$\mathrm{d}A = \frac{e^2\omega}{2\pi\hbar c}\left|\langle f|\,\hat{\mathcal{R}}^\dagger(\boldsymbol{k},\boldsymbol{\epsilon})\,|i\rangle\right|^2 \mathrm{d}\Omega. \tag{2.25}$$

Here, $\hat{\mathcal{R}}^\dagger$ is again the photon emission operator defined in equation 2.18. The relevant scenario for the present thesis is a single K-shell vacancy. Its filling results in an isotropic emission of the fluorescence radiation [116].
A non-radiative de-excitation process, that can only occur in many-electron systems, is the Auger decay. An inner-shell vacancy is filled by an electron from a higher shell and the released energy is used to eject another (outer-shell) electron from the same system. The effect was discovered independently by L. Meitner [117] and P. Auger [118] and named after the latter.
For the present thesis, the fluorescence yield ω_i (i is the shell of the vacancy) is relevant, which is defined as

$$\omega_i = \frac{\Gamma_{rad}}{\Gamma_{rad} + \Gamma_{nonrad}}, \tag{2.26}$$

where Γ_{rad}, Γ_{nonrad} denote the rates for radiative and non-radiative decay, respectively. In [119], derivations for simple estimations of the Z-dependences of Γ_{rad} and Γ_{nonrad} are given:

$$\Gamma_{rad} \propto Z^4, \qquad \Gamma_{nonrad} \propto Z^0. \tag{2.27}$$

This leads to the parametrization of ω_i, which was also already published in [120]:

$$\omega_i = \frac{Z^4}{C_i + Z^4}. \tag{2.28}$$

The (positive) constant C_i depends on the shell of the vacancy of the shell and is smallest for the K-shell, as shown in [121], together with other parametrizations of ω_i. Fluorescence is therefore most prominent in high-Z materials and in the case of K-shell vacancies.

2.3 Basic semiconductor detector concepts

In the present experiment, x-rays were measured with semiconductor detectors. The basic working principle of such detectors will be explained in this section. More

details can be found in [82], from which the content of this section was obtained. A semiconductor detector consists of a high-purity semiconductor crystal, which is electrically contacted on two sides. The crystal material has four valence electrons and common choices are silicon or germanium. The crystal is doped with atoms that have three valence electrons (p-dopants, acceptors) on one side and with five-valence-electrons atoms (n-dopants, donators) on the other side. A donator has one valence electron more than required for the crystal structure, therefore this exceeding electron can freely move within the crystal. An acceptor has one electron less, which leads to a defect (hole) in the crystal structure. Valence electrons of nearby atoms can fill the hole, which consequently shifts. Such a hole can be considered as a positive charge carrier. In the border region between the n- and the p-doped part of the detector crystal, donator electrons diffuse into the p-region and recombine with the holes there. This region then does not contain any more free charge carriers and is therefore called depletion zone. The diffusion leads to a surplus of negative charges (electrons) in the p-region and a surplus of positive charges (holes) in the n-region, which results in an electric field that counteracts the diffusion. The size of the depletion zone, the charge surpluses and the electric field increase until an equilibrium is reached. The voltage V_C, to which the electric field corresponds at that point, is called contact potential and typically 0.6 to 0.7 V. The application of an external reverse bias voltage V_{bias} (positive pole to n-region, negative pole to p-region) causes the free charge carriers to drift to their corresponding contacts. The width z_d of the depletion zone then increases according to

$$z_d = \sqrt{\frac{2\varepsilon_0\varepsilon_r \cdot (V_C + V_{bias})}{e} \cdot \left(\frac{N_A + N_D}{N_A \cdot N_D}\right)}, \tag{2.29}$$

where ε_r is the relative permittivity of the crystal material and N_A, N_D are the concentrations of acceptor- and donator atoms, respectively. The depletion zone is the active volume of the detector. In order to maximize it, a large bias voltage on the order of kV is applied. When an energy E is deposited in the depletion zone, a local cloud of electron-hole pairs with total charge $\Delta q \propto E$ is created. These charge carriers drift to opposite sides of the detector, which induces a change of voltage

$$\Delta U = \frac{\Delta q}{C}. \tag{2.30}$$

The detector capacity C depends on the geometry of the detector. In this thesis, only planar detectors are used, where the active volume is between two parallel

contacts. Another commonly used type is a coaxial detector, where one contact is located in the center of, the other one around a cylinder. For a planar detector with surface area A, the capacity can be calculated as for a plate capacitor:

$$C = \varepsilon_0 \varepsilon_r \cdot \frac{A}{z_d}. \tag{2.31}$$

For a good signal-to-noise ratio, ΔU should be maximized and therefore C minimized. This is already achieved through the maximization of z_d and can be optimized further by choosing a small surface area A. Reduction of A means a reduction of the active area which is usually not desired. This problem can be solved by using segmented detectors which combine a large total active area with small areas of the individual contacts (see section 4.2.2). Without energy deposition, electron-hole pairs can also be created via thermal excitation. This effect degrades the energy resolution and can be reduced by cooling the detector crystal using, for example, liquid nitrogen. Additional noise contributions can arise from the readout electronics connected to the detector. The most crucial one is the preamplifier, which is the first component behind the detector. Cooling also this part of the system greatly improves the resolution.
In the following, the charge carrier movement in the detector crystal is discussed in more detail. In the presence of an electric field $\mathcal{E}$, a charge carrier (electron or hole) drifts with the velocity

$$\boldsymbol{v}_d = \mu(\mathcal{E}) \cdot \mathcal{E}. \tag{2.32}$$

In general, the material-specific mobility μ is a function of the electric field, which again is a function of the position. During the drift, charge carriers can be lost, for example by recombination or trapping. This results in a reduced collection efficiency and due to its statistical nature, this process softens the proportionality $\Delta U \propto E$. Another effect is a widening of the charge cloud during the drift. In a simple approximation, the widening can be described as a diffusion process. The spatial distribution of the charge cloud is given by a gaussian with increasing variance

$$\sigma^2(t) = \sqrt{2Dt}, \tag{2.33}$$

where t is the drift time and D the diffusion constant. The latter is given by the

Nernst-Einstein relation [122]:

$$D = \frac{k_B T}{e} \mu. \tag{2.34}$$

It depends on the mobility and the temperature T, $k_B \approx 8.62 \cdot 10^{-5}$ eV/K is the Boltzmann constant. In a more complex description of the charge cloud widening, also the repulsion of the charge carriers among each other has to be taken into account. This was done, for example in [123, 124], but neglected in the present thesis.

2.4 Synchrotron radiation source

The term "synchrotron" refers to an accelerator for charged particles that is built as a closed loop of linear acceleration sections and bending magnets. In contrast to a linear accelerator, a synchrotron has the advantage, that only a few accelerating sections are needed, as the particles to be accelerated traverse them many times. The disadvantage is, that the particles loose energy in the bending sections in form of so-called synchrotron radiation. This initially unwanted effect is nowadays exploited as the main feature in high-brilliance light sources, which therefore are referred to as synchrotron radiation sources. These are operated as storage rings, where the charged particles orbit with a constant velocity and the accelerating sections are mainly used to compensate for the energy losses. In modern facilities, a more elaborated concept than bending magnets is used to generate synchrotron radiation: a periodically alternating magnetic field structure is inserted into a straight section of the storage ring. In that section, the charged particles perform sinosoidal oscillations, which generates the desired radiation. Depending on the structure's dimensions, it is either called a wiggler or an undulator. A schematic view of such a device is shown in figure 2.9. The period of the magnetic field is denoted λ_u. It is related to the wavelength λ of the generated synchrotron radiation via the undulator equation [127]:

$$\lambda(\theta) = \frac{\lambda_u}{2\gamma^2} \left(1 + \frac{K^2}{2} + \gamma^2 \theta^2\right). \tag{2.35}$$

The generated wavelength depends on the emission angle θ (with respect to the particle beam direction), the particles' Lorentz factor γ and the dimensionless undulator

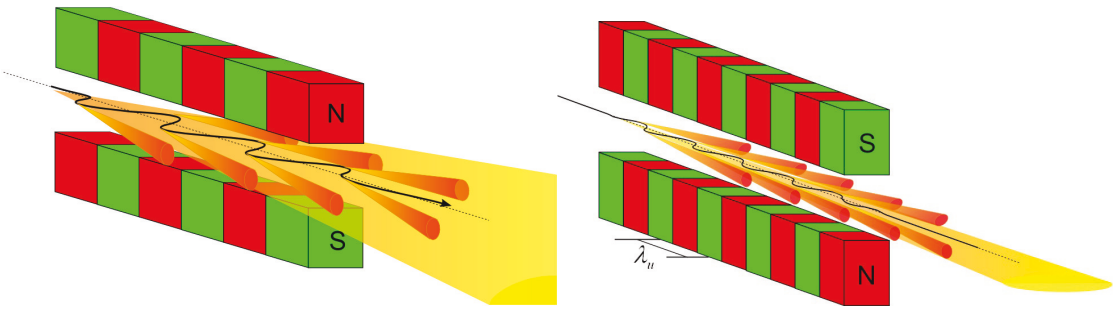

(a) (b)

Figure 2.9: Magnetic field structure in (a) a wiggler and (b) an undulator. The black line indicates the trajectory of the charged particles, the red lobes the emitted synchrotron radiation at different positions. Graphics from [125, 126].

parameter K, which is defined (for electrons and positrons) as [127]

$$K = \frac{eB\lambda_u}{2\pi m_e c}. \tag{2.36}$$

The undulator parameter describes the strength of the deflection of the particles. It can be varied to tune the wavelength of the emitted radiation. Usually λ_u is fixed, therefore the magnetic field B is varied. If permanent magnets are used, the field acting on the particle beam is adjusted via the distance between the magnet sequences on opposite sides of the beam, the so-called undulator gap. Large values $K > 1$ indicate a wiggler. The charged particles are strongly deflected in the magnetic field and the lobes of emitted radiation form relatively large angles with the beam direction. The lobes from different positions can therefore not interfere, which results in a broad spectral emission. An undulator is represented by $K < 1$. In this case only a small deflection occurs. The radiation is emitted near the beam axis, which not only leads to a small opening angle of the emitted photon beam, but also to an interference of the lobes from the different positions. The result of this interference is a narrow energy spectrum.

3 Polarized photon scattering

The photon scattering processes relevant for this thesis – Compton- and Rayleigh scattering – were already introduced in chapter 2. In the present chapter, the discussion will be extended to polarization effects that are relevant for scattering. The description of the photon polarization using Stokes parameters is explained in section 3.1. With this concept established, the scattering processes can be described with the transfer matrix formalism which is covered in section 3.2. The application of that formalism to Compton- and Rayleigh scattering is shown in sections 3.3 and 3.4, respectively.

3.1 Polarization of photons

In this section, the main concepts and terminology of photon polarization are introduced. Section 3.1.1 describes of types of polarization that a single photon can have. The characterization of photon beams is outlined in section 3.1.2.

3.1.1 Polarization of a single photon

Photons can be described as electromagnetic waves. Both the electric field $\boldsymbol{\mathcal{E}}$ and the magnetic field $\boldsymbol{\mathcal{B}}$ oscillate transversely to the wave's propagation direction. For a complete description it suffices to give one of the fields, usually one chooses $\boldsymbol{\mathcal{E}}$. It is convenient to write $\boldsymbol{\mathcal{E}}$ as the real part of a complex electric field $\boldsymbol{E}$. In the simplest case one has a plane wave where the time- and space dependence of $\boldsymbol{E}$ is contained in a phase factor $\exp(i(\omega t - \boldsymbol{k}^T\boldsymbol{r}))$. Its parameters are the (angular) frequency ω and the wave vector $\boldsymbol{k}$. The energy of the photon is given by $E = \hbar\omega$. The phase factor is multiplied by a constant amplitude with real magnitude $\mathcal{E}_0$ and complex (unit) direction $\boldsymbol{\epsilon}$ which defines the polarization of the photon. The overall expression for the electric field then is

$$\boldsymbol{\mathcal{E}}(\boldsymbol{r}, t) = \Re\left\{\boldsymbol{E}(\boldsymbol{r}, t)\right\} = \mathcal{E}_0 \cdot \Re\left\{\boldsymbol{\epsilon} \cdot \exp(i(\omega t - \boldsymbol{k}^T\boldsymbol{r}))\right\}. \tag{3.1}$$

The transversality $\boldsymbol{k}^T \cdot \boldsymbol{\mathcal{E}} = 0$ implies, that $\boldsymbol{\epsilon}$ can be represented by any pair of (complex) orthonormal base vectors $\boldsymbol{b}_1$ and $\boldsymbol{b}_2$ that are orthogonal to $\boldsymbol{k}$. The or-

thonormality between the base vectors reads

$$\boldsymbol{b}_i^\dagger \cdot \boldsymbol{b}_j = \delta_{ij}, \tag{3.2}$$

where the † symbol indicates the combination of complex conjugation and transposition (here: of a column vector, in general: of a matrix). The electric field orientation is given by

$$\boldsymbol{\epsilon} = (\boldsymbol{b}_1^\dagger \cdot \boldsymbol{\epsilon})\boldsymbol{b}_1 + (\boldsymbol{b}_2^\dagger \cdot \boldsymbol{\epsilon})\boldsymbol{b}_2. \tag{3.3}$$

In order to facilitate the following discussion, it is helpful to define a coordinate system. In this case, a right-handed (real) orthonormal system $\{\boldsymbol{e}_1,\boldsymbol{e}_2,\boldsymbol{e}_3\}$ with $\boldsymbol{e}_3 \parallel \boldsymbol{k}$ is convenient. A common choice is $\boldsymbol{e}_1 = \boldsymbol{e}_x$, $\boldsymbol{e}_2 = \boldsymbol{e}_y$ and $\boldsymbol{e}_3 = \boldsymbol{e}_z$. In scattering scenarios, this choice is not always possible as there are several photon propagation directions (incident and scattered photon). Therefore the general case shall be considered here. With the coordinate system given, one can now specify bases $\{\boldsymbol{b}_1, \boldsymbol{b}_2\}$ that represent different polarizations. The base vectors

$$\boldsymbol{e}_\parallel := \boldsymbol{e}_1, \qquad \boldsymbol{e}_\perp := \boldsymbol{e}_2 \tag{3.4}$$

represent linear polarization along the coordinate system axis $\boldsymbol{e}_1$ and $\boldsymbol{e}_2$, respectively. The orientation of the electric field vector then does not vary in time and space, only its magnitude does. Linear polarizations rotated around the $\boldsymbol{e}_3$ axis by an angle ϕ_0 (with respect to the $\boldsymbol{e}_1$ axis) can be constructed via

$$\boldsymbol{b}_{\phi_0} = \cos(\phi_0)\boldsymbol{e}_\parallel + \sin(\phi_0)\boldsymbol{e}_\perp. \tag{3.5}$$

The special cases $\phi_0 = \pm 45°$ form the base

$$\boldsymbol{e}_\nearrow := \frac{1}{\sqrt{2}}\left(\boldsymbol{e}_1 + \boldsymbol{e}_2\right), \qquad \boldsymbol{e}_\searrow := \frac{1}{\sqrt{2}}\left(\boldsymbol{e}_1 - \boldsymbol{e}_2\right) \tag{3.6}$$

which will be used later. The base vectors

$$\boldsymbol{e}_R := \frac{1}{\sqrt{2}}\left(\boldsymbol{e}_1 - i\boldsymbol{e}_2\right), \qquad \boldsymbol{e}_L := \frac{1}{\sqrt{2}}\left(\boldsymbol{e}_1 + i\boldsymbol{e}_2\right) \tag{3.7}$$

represent right-handed (R) and left-handed (L) circular polarization. The electric field vector of a circularly polarized photon has a constant magnitude and it rotates around the photon propagation direction. The convention used here is that the handedness is defined from the point of view of the source. The general case of photon

polarization is called elliptical polarization. It is constructed from a superposition of linear and circular polarization. The electric field vector then rotates around the propagation direction and changes its magnitude, forming an ellipse. The different types of polarization are illustrated in figure 3.1. Any photon polarization is fully

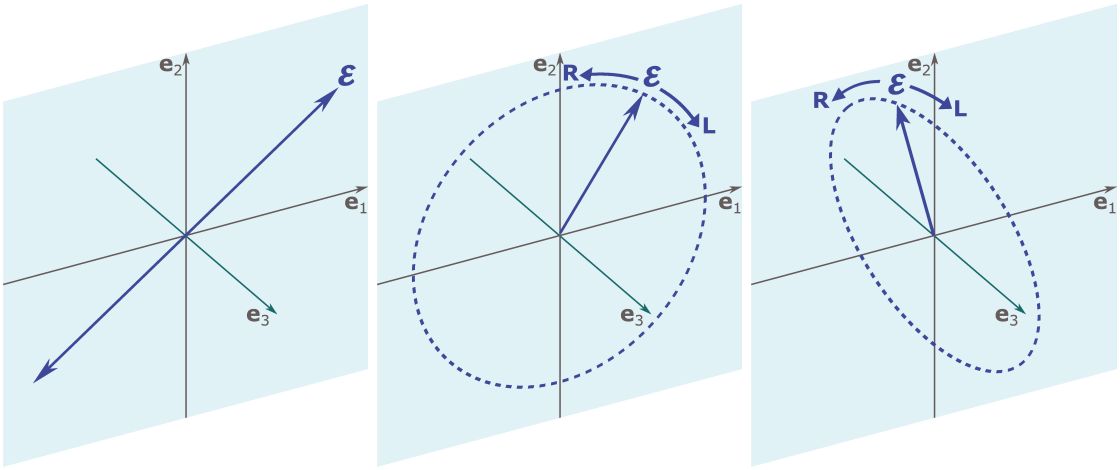

(a) (b) (c)

Figure 3.1: Polarization states of a single photon. (a) Linear polarization. (b) Circular polarization. (c) Elliptical polarization. The orientation of the electric field vector is shown. For circular and elliptical polarization, its temporal evolution is indicated for right-handed (R) and left-handed (L) polarization.

characterized by $\boldsymbol{\epsilon}$. Alternatively, one can use Stokes parameters [128, 129] for the polarization description:

$$\xi_1 = |\boldsymbol{e}_{\parallel}^{\dagger}\boldsymbol{\epsilon}|^2 - |\boldsymbol{e}_{\perp}^{\dagger}\boldsymbol{\epsilon}|^2 \tag{3.8}$$

$$\xi_2 = |\boldsymbol{e}_{\nearrow}^{\dagger}\boldsymbol{\epsilon}|^2 - |\boldsymbol{e}_{\searrow}^{\dagger}\boldsymbol{\epsilon}|^2 \tag{3.9}$$

$$\xi_3 = |\boldsymbol{e}_{R}^{\dagger}\boldsymbol{\epsilon}|^2 - |\boldsymbol{e}_{L}^{\dagger}\boldsymbol{\epsilon}|^2. \tag{3.10}$$

Note, that these Stokes parameters correspond to a single photon, so they satisfy

$$\xi_1^2 + \xi_2^2 + \xi_3^2 = 1. \tag{3.11}$$

In the following section it is shown, how Stokes parameters for the description of a photon beam are defined.

3.1.2 Polarization of a photon beam

The difficulty in describing a photon beam is that its (complex) electric field $\boldsymbol{E}_{beam}$ can in general not be written as in 3.1. This is due to the fact, that a partially polarized beam is an incoherent superposition of photons with different orientations $\boldsymbol{\epsilon}$. The *absolute* Stokes parameters characterizing a beam are defined as

$$\begin{aligned} S_0 &:= I_{\parallel} + I_{\perp} \;\propto \left\langle |\boldsymbol{e}_{\parallel}^{\dagger}\boldsymbol{E}_{beam}|^2 + |\boldsymbol{e}_{\perp}^{\dagger}\boldsymbol{E}_{beam}|^2 \right\rangle_T , \\ S_1 &:= I_{\parallel} - I_{\perp} \;\propto \left\langle |\boldsymbol{e}_{\parallel}^{\dagger}\boldsymbol{E}_{beam}|^2 - |\boldsymbol{e}_{\perp}^{\dagger}\boldsymbol{E}_{beam}|^2 \right\rangle_T , \\ S_2 &:= I_{\nearrow} - I_{\searrow} \propto \left\langle |\boldsymbol{e}_{\nearrow}^{\dagger}\boldsymbol{E}_{beam}|^2 - |\boldsymbol{e}_{\searrow}^{\dagger}\boldsymbol{E}_{beam}|^2 \right\rangle_T , \\ S_3 &:= I_R - I_L \;\propto \left\langle |\boldsymbol{e}_{R}^{\dagger}\boldsymbol{E}_{beam}|^2 - |\boldsymbol{e}_{L}^{\dagger}\boldsymbol{E}_{beam}|^2 \right\rangle_T . \end{aligned} \tag{3.12}$$

The $\langle \dots \rangle_T$ operator indicates a time average over the fast oscillations of the electric field. The Stokes parameters can be accessed experimentally by measuring intensities I. Different "types" of intensities can be used, for example in a scattering experiment: for the incident beam one uses the number of photons per area and time, whereas the scattered beam is conveniently characterized by the number of photons per solid angle and time. The total intensity of the beam is given by S_0, whereas the other Stokes parameters represent intensity differences between orthogonal polarization states. The intensity I_x corresponding to a polarization state x can be measured by passing the beam through a filter that blocks photons with the orthogonal polarization $\overline{x}$. For soft x-rays ($\hbar\omega < 20$ keV), such (almost) perfect filters can be realized, for example, with channel-cut crystals [130]. For higher photon energies, as discussed in this thesis, indirect methods such as Compton polarimetry (see section 5.1.2) are required. Instead of the absolute Stokes parameters $\{S_i\}$ one usually considers *normalized* Stokes parameters $\{P_i\}$ defined as

$$P_i = \frac{S_i}{S_0}, \qquad i = 0, \dots, 3. \tag{3.13}$$

All three sets $\{\xi_i\}$, $\{S_i\}$ and $\{P_i\}$ are commonly simply referred to as "Stokes parameters". A compact notation of latter two is given by the (absolute and normalized)

Stokes vector

$$\boldsymbol{S} = \begin{pmatrix} S_0 \\ S_1 \\ S_2 \\ S_3 \end{pmatrix}, \qquad \boldsymbol{P} = \begin{pmatrix} 1 \\ P_1 \\ P_2 \\ P_3 \end{pmatrix}. \tag{3.14}$$

In order to illustrate the meaning of the Stokes parameters, some special cases are discussed:

- $P_1 = P_2 = P_3 = 0$: unpolarized beam.
- $P_1 = \cos(2\phi_0)$, $P_2 = \sin(2\phi_0)$, $P_3 = 0$: all photons in the beam are linearly polarized in the direction given by the angle ϕ_0 (as in equation 3.5).
- $P_1 = P_2 = 0$, $P_3 = \pm 1$: all photons in the beam are circularly polarized ($+$: right-handed, $-$: left-handed).

A quantity that "summarizes" the polarization of a photon beam is the degree of polarization defined as

$$P = \sqrt{P_1^2 + P_2^2 + P_3^2} \leq 1. \tag{3.15}$$

In beams without circular polarization components ($P_3 = 0$) this reduces to the degree of linear polarization

$$P_L = \sqrt{P_1^2 + P_2^2}. \tag{3.16}$$

This quantity is commonly used to describe partially linearly polarized beams. The Stokes parameters are parametrized as

$$P_1 = P_L \cdot \cos(2\phi_0), \; P_2 = P_L \cdot \sin(2\phi_0), \; P_3 = 0. \tag{3.17}$$

In such a beam, the fraction $(1 + P_L)/2$ of the photons is linearly polarized in the direction of ϕ_0, $(1 - P_L)/2$ orthogonal to it.

3.2 Transfer matrix formalism

The Stokes parameters offer a convenient way to describe scattering of photon beams. For this, let $\boldsymbol{S}$ be the (absolute) Stokes vector of the incident photon beam.

The goal is to have an expression for the Stokes vector of the scattered photon beam $\boldsymbol{S}'$. From the definition 3.12 of the Stokes parameters it is clear, that they depend on the chosen coordinate system. In a scattering scenario, where two photons are involved, also two coordinate systems need to be defined. Depending on those choices, $\boldsymbol{S}$ and $\boldsymbol{S}'$ as well as their functional dependence change. Let $\{\boldsymbol{e}_1, \boldsymbol{e}_2, \boldsymbol{e}_3\}$ and $\{\boldsymbol{e}_1', \boldsymbol{e}_2', \boldsymbol{e}_3'\}$ be the coordinate systems before and after the scattering process, respectively. In this thesis, they are chosen as illustrated in figure 3.2. The axis $\boldsymbol{e}_3$

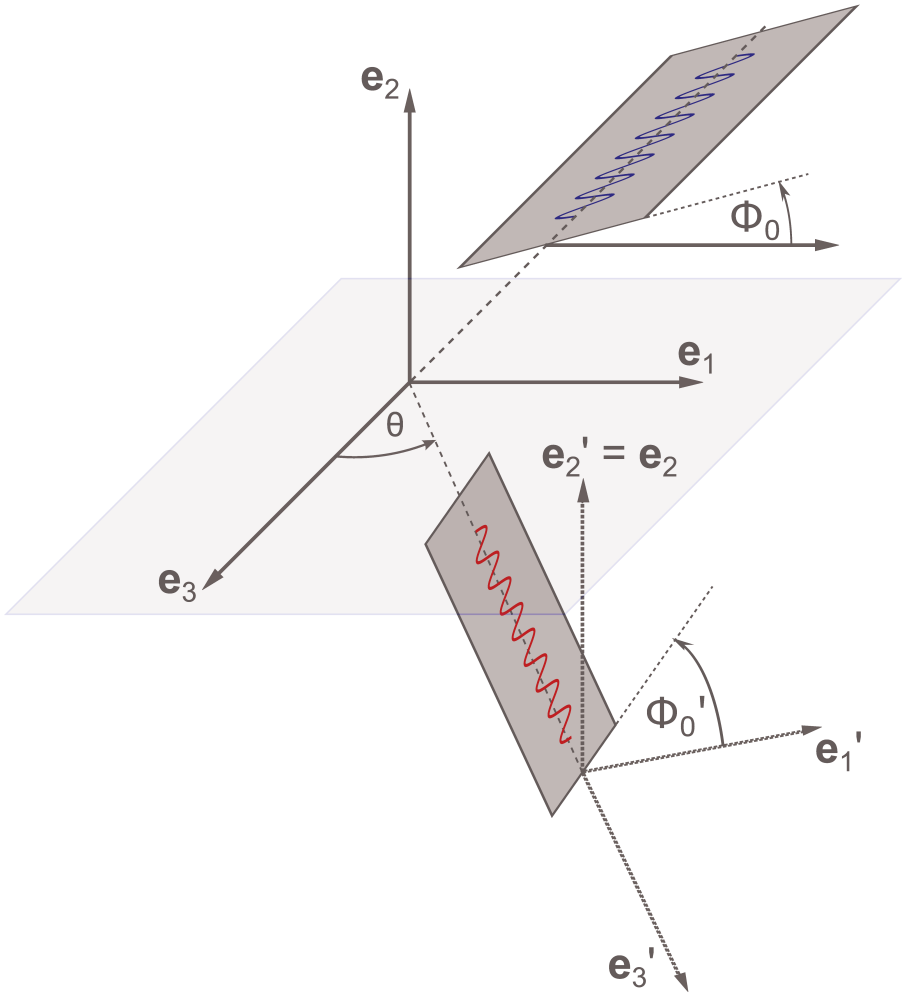

Figure 3.2: Geometry for photon scattering: Photons are indicated by a blue (incident) and red (scattered) wavy line. θ is the angle between their propagation directions. Their polarization orientations form angles ϕ_0 and ϕ_0', respectively, with the scattering plane (in case of linear polarization).

and $\boldsymbol{e}_3'$ corresponding to the directions of the wave vectors $\boldsymbol{k}$ and $\boldsymbol{k}'$ of the incident and scattered photon, respectively, define the scattering plane. The angle between

$\boldsymbol{e}_3$ and $\boldsymbol{e}'_3$ is the polar scattering angle θ. The axis $\boldsymbol{e}_1$ and $\boldsymbol{e}'_1$ are chosen in the scattering plane, the axis $\boldsymbol{e}_2$ and $\boldsymbol{e}'_2 = \boldsymbol{e}_2$ perpendicular to it. The indicated angles ϕ_0 and ϕ'_0 are relevant for the case of linear polarization when the Stokes parameters can be written as in equation 3.17.
With the coordinate systems established, one can now turn to the relation between $\boldsymbol{S}$ and $\boldsymbol{S}'$. They are connected via a linear transformation – the 4×4 transfer matrix T [129]:

$$\boldsymbol{S}' = T \cdot \boldsymbol{S}. \tag{3.18}$$

The entries of T describe the physics of the scattering process, so they depend on the scatterer, the incident photon energy and the polar scattering angle θ. For scattering, their dimension is a differential cross section [area per solid angle], as the dimensions of $\boldsymbol{S}$ and $\boldsymbol{S}'$ are [number of photons per area and time] and [number of photons per solid angle and time], respectively. An explicit dependence on the azimuthal scattering angle φ, which was introduced in section 2.1.2, is not contained in T. This is due to the fact, that the coordinate systems are defined with respect to the (possibly variable) scattering plane and not with respect to a certain fixed laboratory system. But often – also in this thesis – it is convenient to write the Stokes vector of the incident beam in such a fixed system $\{\boldsymbol{e}_{1,Lab},\ \boldsymbol{e}_{2,Lab},\ \boldsymbol{e}_{3,Lab}\}$, so that it does not depend on the orientation of the scattering plane. The $\boldsymbol{e}_{3,Lab}$ axis corresponds to the incident photon propagation direction. The $\boldsymbol{e}_{1,Lab}$ axis is the reference direction in the laboratory frame which corresponds to an azimuthal scattering angle $\varphi = 0$. Usually one chooses the direction of the (linear) polarization of the incident beam as the $\boldsymbol{e}_{1,Lab}$ axis. If the scattering plane is tilted by an arbitrary angle φ against the $\boldsymbol{e}_{1,Lab}$ axis (see figure 3.3), one needs to transform the laboratory Stokes vector $\boldsymbol{S}_{Lab}$ into the Stokes vector $\boldsymbol{S}$ in the $\{\boldsymbol{e}_1, \boldsymbol{e}_2, \boldsymbol{e}_3\}$ system so that equation 3.18 can still be applied. They are related by a linear transformation

$$\boldsymbol{S} = M(\varphi) \cdot \boldsymbol{S}_{Lab} \tag{3.19}$$

with the rotation matrix

$$M(\varphi) = \begin{pmatrix} 1 & 0 & 0 & 0 \\ 0 & \cos(2\varphi) & \sin(2\varphi) & 0 \\ 0 & -\sin(2\varphi) & \cos(2\varphi) & 0 \\ 0 & 0 & 0 & 1 \end{pmatrix}. \tag{3.20}$$

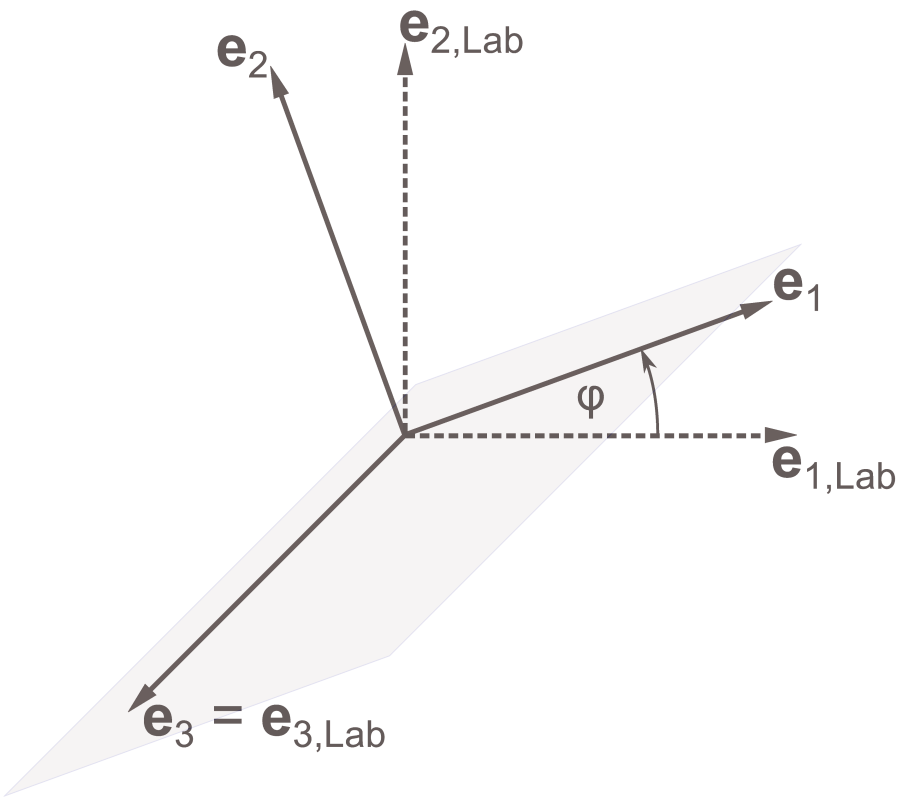

Figure 3.3: Scattering plane rotated around the incident photon direction by the azimuthal scattering angle φ with respect to the laboratory axis $\boldsymbol{e}_{1,Lab}$.

Combining equations 3.18 and 3.19 leads to

$$\boldsymbol{S}' = T(\theta) \cdot M(\varphi) \cdot \boldsymbol{S}_{Lab}. \tag{3.21}$$

The θ-dependence of T is written explicitly in equation 3.21 in order to demonstrate the convenient factorization into terms that depend on only one of the scattering angles. The differential cross section of the scattering process can be written as

$$\frac{\mathrm{d}\sigma}{\mathrm{d}\Omega}(\theta, \varphi) = \frac{S_0'}{S_{0,Lab}} = (1, 0, 0, 0) \cdot T(\theta) \cdot M(\varphi) \cdot \boldsymbol{P}_{Lab}. \tag{3.22}$$

3.3 Polarized photon Compton scattering

An extensive discussion of the transfer matrix formalism applied to Compton scattering is found in [129]. In that paper, the coordinate systems are chosen slightly different, so the entries in the Compton transfer matrix T_C are not exactly the same as in the present thesis. The same coordinate systems as here are chosen in [131]

and the corresponding transfer matrix reads:

$$T_C = \frac{r_e^2}{2} \cdot \left(\frac{k'}{k}\right)^2 \times \begin{pmatrix} 1+\cos^2(\theta)+(k-k')(1-\cos(\theta)) & -\sin^2(\theta) & 0 & T_{03} \\ -\sin^2(\theta) & 1+\cos^2(\theta) & 0 & T_{13} \\ 0 & 0 & 2\cos(\theta) & T_{23} \\ T_{30} & T_{31} & T_{32} & T_{33} \end{pmatrix} \tag{3.23}$$

One should note, that equation 3.23 describes the Compton process for the simplified case where the final electron spin is not observed. Furthermore, the entries in the last row and column are not relevant in this thesis and therefore they are not explicitly given to improve readability. These terms are connected to the circular polarization components of the incident (last column) and the scattered (last row) photon. All except T_{33} are proportional to the spin of the incident electron, so they vanish (on average) for non-spin-polarized targets, which is the only scenario considered in this thesis. Since the employed polarimeter is not sensitive to circular polarization, the entire last row and therefore in particular T_{33} is neglected. For calculations with T_C in this thesis, only the upper left 3×3 submatrix is used and the Stokes vectors $\boldsymbol{P}$ and $\boldsymbol{S}$ are treated as three-component vectors. As will be shown in section 3.4, this can also be done in the case of Rayleigh scattering.

3.4 Polarized photon Rayleigh scattering

The general structure of the cross section for elastic scattering from an unpolarized atomic target has been derived in [75]. It leads to a transfer matrix of the following form:

$$T_R = \begin{pmatrix} T_{00} & T_{01} & 0 & 0 \\ T_{01} & T_{11} & 0 & 0 \\ 0 & 0 & T_{22} & -T_{32} \\ 0 & 0 & T_{32} & T_{33} \end{pmatrix}. \tag{3.24}$$

The structure of T_R is similar to the one of T_C (for an unpolarized target), but T_R has non-zero entries at the positions (2,3) and (3,2). These give rise to the so-called type-L circular dichroism, where circular polarization components of the incident beam can affect linear polarization components of the scattered beam (and vice

versa). This effect is discussed in [74] and the results in that paper indicate that T_{32} can be up to 20 % of T_{00} for high-Z scatterers and photon energies between 100 keV and 1 MeV. In this thesis, effects of a non-zero T_{32} are neglected, as it is assumed that P_3 of the incident beam is close to zero and that P_3 of the scattered beam cannot be measured. Therefore – as for T_C – only the upper left 3×3 matrix is used here. As pointed out in [74], results can be approximated assuming $J_i = J_f = 0$ in equation 2.20 (which is exact for closed-shell atoms), for further discussion see [132]. This approximation is also applied in the theory shown in the present thesis [106]. It simplifies the general expression for the cross section in [75] to the result that has already been shown in [28] (here the definitions of the Stokes parameters ξ_i of [28] are used, primed ones correspond to the scattered photon):

$$\begin{aligned}\frac{\mathrm{d}\sigma}{\mathrm{d}\Omega} = &\frac{1}{4} \cdot \left(\left|A_\parallel\right|^2 + \left|A_\perp\right|^2\right) \cdot (1 + \xi_1\xi_1') + \frac{1}{4} \cdot \left(\left|A_\parallel\right|^2 - \left|A_\perp\right|^2\right) \cdot (\xi_1 + \xi_1') \\ &+ \frac{1}{2} \cdot \Re\left\{A_\parallel \cdot A_\perp^*\right\} \cdot (\xi_2\xi_2' + \xi_3\xi_3') + \frac{1}{2} \cdot \Im\left\{A_\parallel \cdot A_\perp^*\right\} \cdot (\xi_2\xi_3' - \xi_3\xi_2')\,. \quad (3.25)\end{aligned}$$

The approximation $J_i = J_f = 0$ leads to the following relations in the transfer matrix for Rayleigh scattering 3.24:

$$T_{11} = T_{00}, \qquad T_{33} = T_{22}. \quad (3.26)$$

The remaining entries of T_R are given by (see appendix A for the derivation)

$$\begin{aligned}&T_{00} = \frac{1}{2} \cdot \left(\left|A_\parallel\right|^2 + \left|A_\perp\right|^2\right), \qquad T_{01} = \frac{1}{2} \cdot \left(\left|A_\parallel\right|^2 - \left|A_\perp\right|^2\right), \\ &T_{22} = \Re\left\{A_\parallel \cdot A_\perp^*\right\}, \qquad T_{32} = \Im\left\{A_\parallel \cdot A_\perp^*\right\}. \quad (3.27)\end{aligned}$$

These expressions are plotted for $\hbar\omega = 175$ keV and $Z = 79$ as a function of the scattering angle θ in figure 3.4. The fully relativistic S-matrix calculations from [106], which are employed in the present thesis are shown together with a form factor approximation. Data for the latter are obtained from [133, 134], where different form factors are tabulated. Here, the modified relativistic form factors with angle-independent anomalous scattering factors (MFASF) are used. They were identified in [31] as the preferable choice against other form factor options. Following the recommendation of the EPDL[1] documentation [135], a two-point linear interpolation between the data for $\hbar\omega = 145.4$ keV and $\hbar\omega = 244.5$ keV is applied to obtain anomalous scattering factors at $\hbar\omega = 175$ keV and a double-logarithmic interpola-

[1] Evaluated Photon Data Library

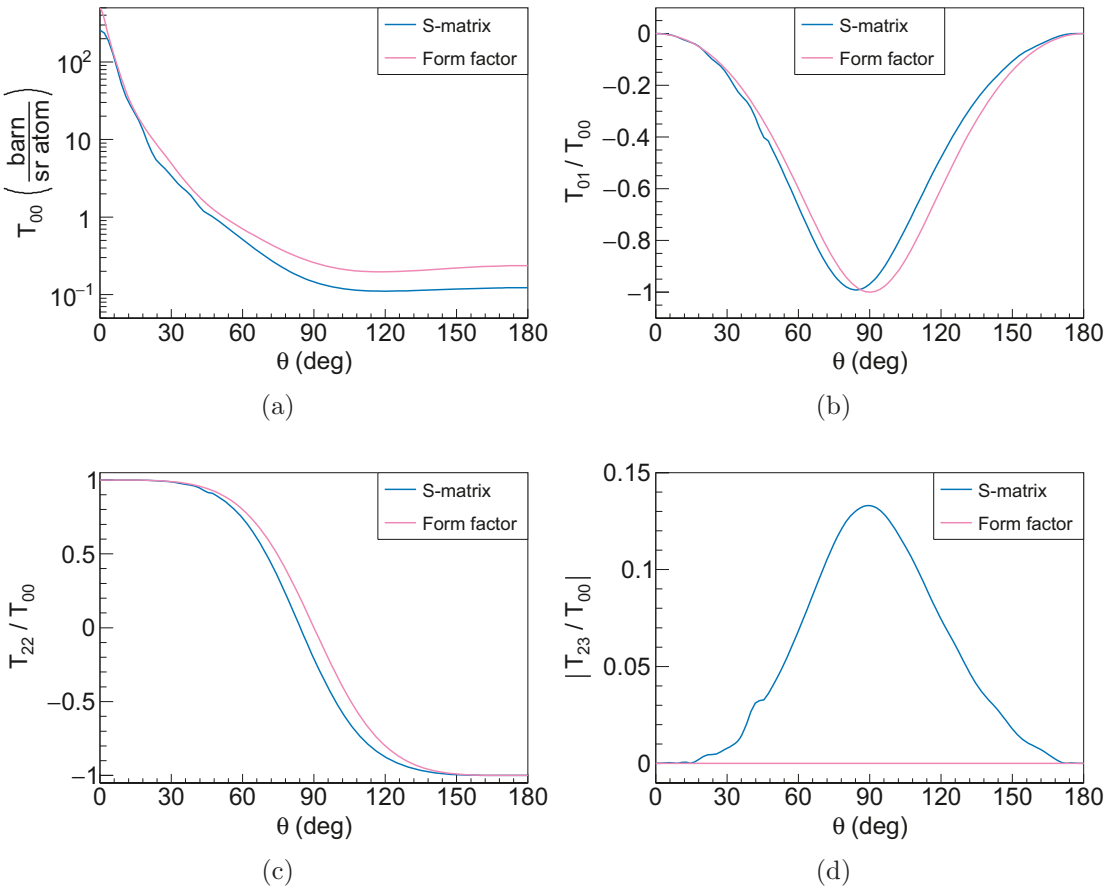

Figure 3.4: Entries of the transfer matrix for Rayleigh scattering at $\hbar\omega = 175$ keV and $Z = 79$. (a) T_{00}. (b) T_{01} normalized to T_{00}. (c) T_{22} normalized to T_{00}. (d) $|T_{23}|$ normalized to T_{00}.

tion is chosen for the form factor values. In figure 3.4a one sees that at $\theta = 0°$, the prediction of T_{00} (which corresponds to the differential cross section for an unpolarized incident beam) for the S-matrix calculations is by almost a factor two lower than for the form factor approximation. This can be explained with the fact, that in the S-matrix calculations, only the shells up to N are included. Higher shells are excluded because they require a lot of computation time and their contribution can be neglected at the angles relevant for the present experiment ($\theta \geq 30°$). As discussed in section 2.1.3, higher shells dominate the scattering at very forward angles, and therefore a large error is introduced in that angular region when these shells are omitted.

4 Experiment

In this chapter, the experimental environment and procedure are described. The most important components are the x-ray source (section 4.1) and detectors (section 4.2). The experimental setup is presented in section 4.3 and the individual measurements are summarized in section 4.4.

4.1 The synchrotron radiation source PETRA III

DESY is a large-scale research facility in Germany and part of the Helmholtz Association [136]. The research at DESY mainly focuses on the areas particle and astroparticle physics, accelerators and photon science.
The particular facility employed for the experiment presented in this thesis is related to the latter two: PETRA III is a particle storage ring operated as an x-ray light source. The parameters given in this paragraph are taken from the DESY website [137]. The storage ring PETRA III has a length of 2304 m and is operated with 6-GeV positrons. The experimental hall "Max von Laue" is almost 300 m long and houses 14 beamlines and 30 experimental stations. Note, that more beamlines and end stations were added during the PETRA III extension project between the experiment presented in this thesis and the writing. The beam current is kept constant (within 1 %) by frequently injecting new positrons ("top-up mode").
The experiment was performed at the High Energy Material Science Beamline P07 [138] at PETRA III, which is operated by the HZG[1]. The radiation at this beamline is produced in an undulator with $\lambda_u = 29$ mm and 66 periods. Photons have linear polarization in the horizontal plane and their energy can be tuned between 50 and 200 keV. The energy resolution at 80 keV is 5 to 250 eV. These specifications are from the unified data sheet of P07 available on the DESY website [139]. The energy is tuned via a double crystal monochromator described also on the DESY website [140] together with a schematic view of the beamline [141] which is shown in figure 4.1. The experiment of this thesis was performed in the experimental hutch EH3. Several beam collimators in OH2 and EH3 were used during the experiment to set the beam size to 1.1 mm. This value was found by trial-and-error with the purpose

[1]Helmholtz-Zentrum Geesthacht, Centre for Materials and Coastal Research

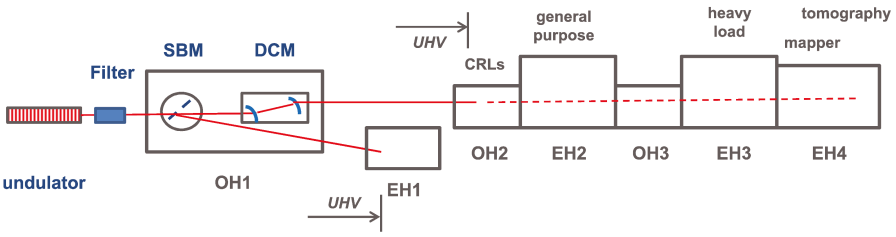

Figure 4.1: Schematic view of the beamline P07. Abbreviations are SBM (single bounce monochromator), DCM (double crystal monochromator), OH (optics hutch), EH (experimental hutch), UHV (ultra high vacuum), CRL (compound refractive lens). Graphic from [141].

to achieve a photon rate on the detector high enough for good statistics, but also not too high to avoid dead time and pile-up.

4.2 Employed detector systems

This section briefly introduces the two detectors that were employed in the present experiment to detect x-rays. Both are planar semiconductor detectors based on the principles described in section 2.3. Their crystal materials are germanium and silicon, respectively. Both detectors were cooled with liquid nitrogen during the experiment.

4.2.1 Standard Ge(i) detector

This high-purity germanium (HPGe) detector is commercially available from ORTEC. The model number is GLP-25300/13P4 and the parameters cited here can be found in the online product configuration guide [142]. The detector crystal is a cylinder with an active diameter of 25 mm and a depth of 13 mm. It is shielded from the environment by a beryllium window with a thickness of 0.25 mm. Design values for the energy resolution (FWHM[2]) are 300 eV at 5.9 keV and 545 eV at 122 keV. The input stage of the preamplifier of this detector is cooled, so that the energy resolution is only minimally degraded by electronic noise. In the experiment, this detector was used for elastic scattering differential cross section measurements. Details on this task follow in section 5.2.

[2]Full Width at Half Maximum

4.2.2 Segmented Si(Li) polarimeter

The lithium-drifted silicon (Si(Li)) detector was developed at IKP[3], FZJ[4] within the SPARC[5] collaboration [143] as a dedicated Compton polarimeter for hard x-rays between $\sim$ 70 keV and a few 100 keV [144]. Detailed descriptions and the parameters given here can be found in previous thesis where it was already employed [36, 39, 65]. The detector crystal has an area of 80×80 mm^2 and a depth of 7 mm. The total area is divided into an active area of 64×64 mm^2 and a guard ring surrounding it to minimize field effects near the boundary. The contacts on the front- and on the backside of the crystal are each divided into 32 strips with a length of 64 mm and a pitch of 2 mm. Neighboring strips are electrically isolated by a 50 μm gap. The strip patterns on the front- and the backside are oriented perpendicular to each other, which results in a structure of 1024 pseudo-pixels (see figure 4.2). Such a structure

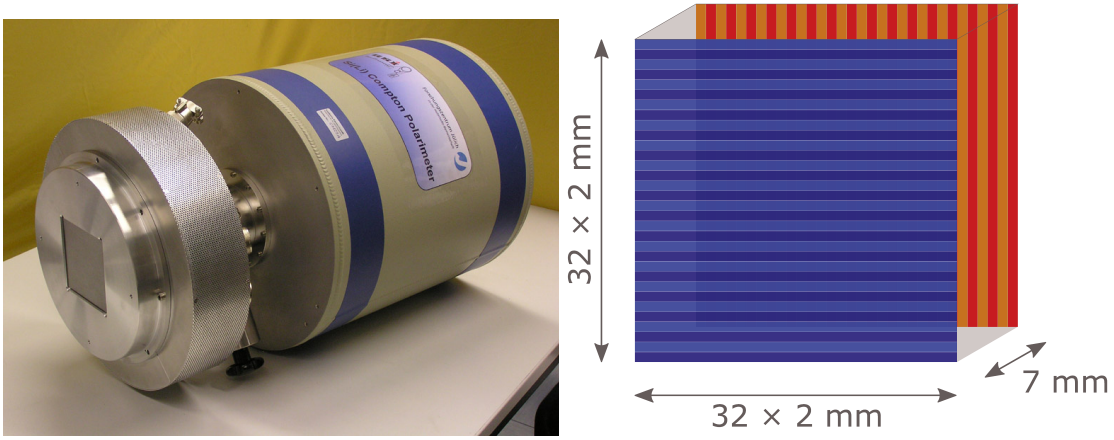

(a) (b)

Figure 4.2: The Si(Li) polarimeter. (a) Photograph (taken from [65]). (b) Schematic view of the strip structure.

enables a two-dimensional determination of the position of energy depositions in the detector. This is achieved by the individual readout of each strip. It is important to note that several simultaneous, spatially separated energy depositions can be registered because this multi-hit capability is one crucial feature for the application as a Compton polarimeter (more details in section 5.1.2). Another one is the energy resolution, which is around 2 keV FWHM at 59.54 keV for an individual strip. In

[3]Institut für Kernphysik
[4]Forschungszentrum Jülich GmbH
[5]Stored Particle Atomic Research Collaboration

addition, each strip has a time resolution of about 50 ns, which allows for background suppression via coincidence conditions. For each strip, readout electronics are required, in particular a preamplifier, which should be mounted as close to the detector as possible. For large numbers of strips, this leads to a space problem, which made it for this detector impossible to be operated with cooled preamplifiers. This explains the – compared to the germanium detector – significantly worse energy resolution. Currently, a similar polarimeter with cooled preamplifiers is being developed.

4.3 Experimental setup

The description of the experimental setup is divided into two parts: section 4.3.1 shows how the individual components are arranged in the laboratory and section 4.3.2 covers the relevant aspects of the data acquisition.

4.3.1 Geometric arrangement

The setup shown in this section is restricted to the end station in the experimental hutch EH3. A schematic top view is given in figure 4.3. The PETRA III photon

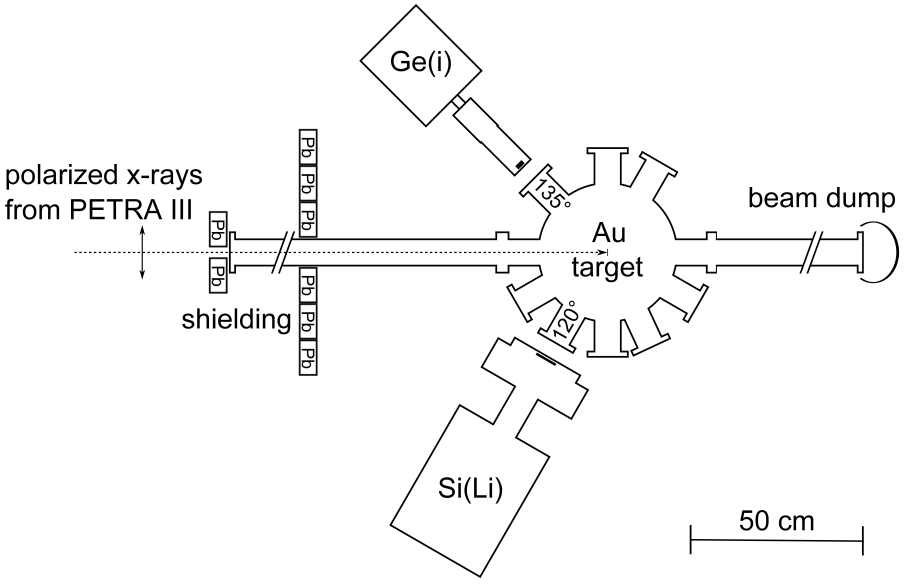

Figure 4.3: Top view of the experimental setup.

beam enters from the left. Its energy was set to 175 keV and its linear polarization

was oriented in the horizontal plane. The target chamber is a vertical cylinder (diameter: 40 cm, height: 31 cm) with several horizontal viewports. It was evacuated to $1.2 \cdot 10^{-7}$ mbar via a pump port located on the bottom end cap. A target holder is inserted via a port on the top end cap. It can hold up to five targets, which can be switched and rotated (around the vertical axis) without breaking the vacuum. The main target for the experiment was a gold foil with a thickness of 1.036 μm. Such a dimensioning combined sufficient luminosity with a minimum of multiple scattering in the target (mean free path length $\approx$ 400 μm). A dump for the incident beam that did not interact with the target is located in the adjacent experimental hutch EH4. The detectors were placed outside the chamber (and therefore outside the vacuum) as close as possible to the viewports. Figure 4.3 shows their placement for the first run corresponding to the indicated scattering angles. At other runs, the detectors were placed at other scattering angles, which, for certain configurations, required a rotation of the entire chamber (around the vertical axis). For all runs, the detectors were placed in the horizontal plane and their viewports were equipped with stainless steel windows. It was found during the experiment, that the incident beam was scattered into the detectors somewhere else than in the target, possibly in the collimators. As a solution, lead blocks were placed as shielding between the final collimator in EH3 and the detectors. It was clearly observed that this measure suppressed the unwanted stray radiation (see section 4.4.3).

4.3.2 Data acquisition

Both detectors were read out using standard analog NIM[6] and VME[7] modules. Detailed descriptions of these components can be found in [82]. Figure 4.4 shows schematically how the polarimeter was connected to the data acquisition system. For a single strip, the following readout chain was adopted: the output signal from the preamplifier ("preamp") of the strip is split into two branches – the time- and the energy branch. The time branch signal is shaped by a fast amplifier (TFA[8]) to generate a short pulse. This pulse is converted into a logic pulse by a CFD[9], if its amplitude is sufficiently large. The logic pulse is fed into three modules: first, it stops a TDC[10], which was initially started by a reference signal. This gives a time

[6]Nuclear Instrumentation Module
[7]Versa Modular Eurocard bus
[8]Timing Filter Amplifier
[9]Constant Fraction Discriminator
[10]Time to Digital Converter

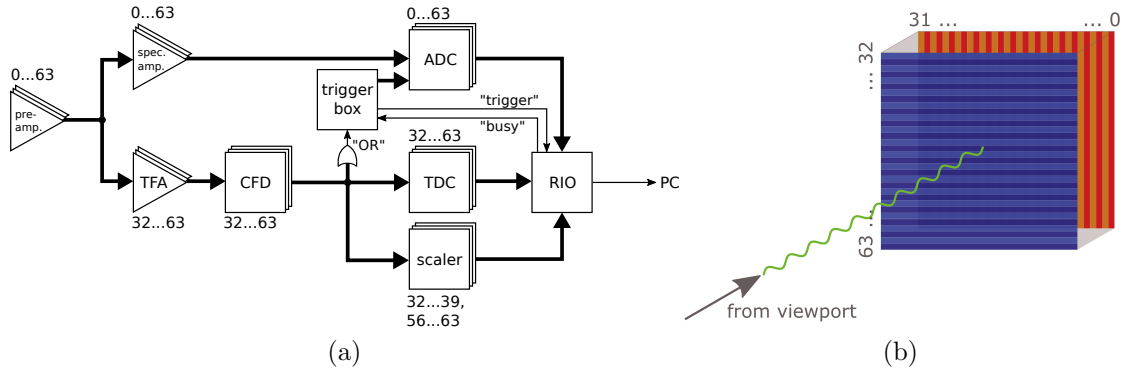

Figure 4.4: Data acquisition for the polarimeter. (a) Simplified schematic of the readout electronics. Numbers at the modules indicate which strips were connected. See text for abbreviations. (b) Choice of strip numbering.

information on the pulse. Second, it increments a scaler. This allows to count how many pulses arrive during one event. Third, a logical "OR" of all the CFD-signals is fed into the trigger box where then a trigger signal is generated. In the energy branch, a spectroscopy amplifier ("spec. amp.") forms a long, smooth (low-noise) pulse which has an amplitude proportional to the energy recorded in the strip. The amplitude is determined and converted into a digital number (here: between 0 and 4095) in an ADC[11]. A signal from the trigger box gates the ADCs (all of them at the same time), so that they are read out only in case of a trigger signal, i.e. when at least one CFD has a valid signal. The outputs of the ADCs, TDCs and scalers are combined in the frontend processor RIO[12] which then writes the data to a listmode file. The readout scheme for the germanium detector is similar, it also stores an ADC, TDC and scaler value. As can be seen from figure 4.4, only part of the strips were connected to TFA, CFD, TDC and scaler modules. This was due to the fact, that only a limited number of CFDs and scalers was available at that time. Only the horizontal frontside strips 32 to 63 were connected to CFDs and therefore generated trigger signals.

4.4 Overview of the measurements

This section summarizes the measurements that were performed during the experiment. The auxiliary measurements beam alignment (section 4.4.1), energy calibra-

[11] Analog to Digital Converter
[12] Remote Input Output

tion (section 4.4.2) and background determination (section 4.4.3) are presented and for the main runs (beam on target), a summary of the parameters is given in section 4.4.4.

4.4.1 Beam alignment

This measurement was performed at the beginning of the experiment. Its purpose was to ensure that the incident beam correctly hits the target. One of the slots in the target holder was equipped with a split fluorescence foil. To see whether the beam hit the foil, a video camera was installed monitoring the target through a 90°-viewport. Additionally, a scintillator was placed at the 30°-viewport. Initially, the target holder was not rotated around the vertical axis (normal beam incidence). For rotations up to 50°, no fluorescence was observed and the event rate recorded by the scintillator was between 40 and 80 s^{-1}. For rotations 70° to 80° the event rate increased to 27000 s^{-1} indicating that the target chamber was well aligned with the incident beam, both horizontally and vertically.

4.4.2 Energy calibration

For all the detectors (Ge(i) and each individual strip of the polarimeter) a calibration had to be performed to find the relation between deposited energy E and recorded ADC value X. Here, a linear dependence with a possible offset is assumed:

$$E = aX + b. \tag{4.1}$$

The calibration parameters a and b were determined by recording the spectrum of a source with known lines E_i, in this case ^{133}Ba. In such a calibration spectrum, the ADC values X_i corresponding to the reference lines were extracted by fitting analytical functions to the peaks. For the spectra of the polarimeter strips, a simple gaussian with linear background was sufficient. The spectra of the Ge(i) detector featured narrower lines and more statistics which required more complicated fit functions for some lines. These functions were among those discussed in section 5.2.3. The parameters a and b were obtained by fitting a straight line to the pairs (X_i, E_i). Calibration spectra were recorded several times during the experiment: for each run either directly before or after it. Example calibration spectra are shown in figure 4.5.

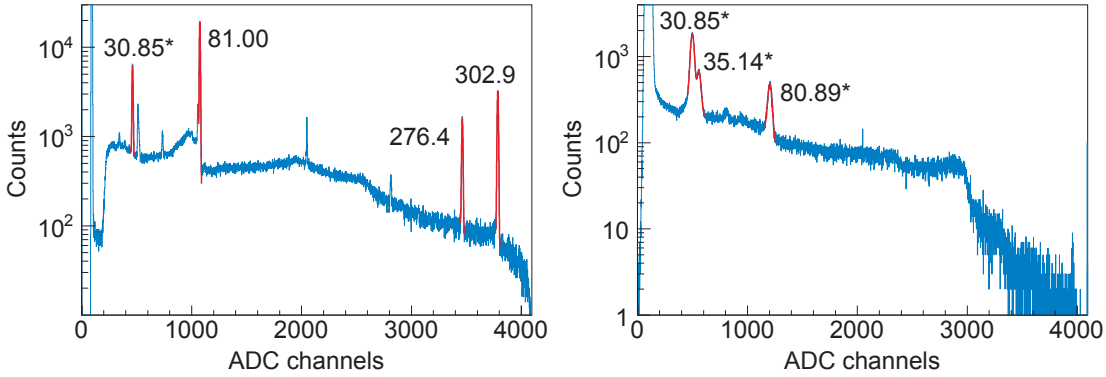

(a) (b)

Figure 4.5: ^{133}Ba calibration spectra. (a) Ge(i). (b) Polarimeter strip 15. Red fits indicate the lines (with energies in keV) that were used for calibration. Reference lines are from [145]. Values with a * are weighted means of overlapping lines.

4.4.3 Background measurement

In this context, the term "background" refers to energy depositions in the detectors that do not originate from the scattering target, but they may or may not originate from the incident beam. They include in particular scattering of the incident beam from objects other than the target, as mentioned in section 4.3.1. This effect was found during the first run (Ge(i) at 135°, polarimeter at 120°) when the lead shielding shown in figure 4.3 was not placed yet. It was identified by comparing the position spectra of Au $K\alpha$ fluorescence photons and elastically scattered photons. To be more specific, these spectra represent the position distributions of single hits (one energy deposition per event) over the surface of the polarimeter. The position spectra are shown in figure 4.6. A round structure is seen for the fluorescence photons from the target. This reflects the fact, that the detector was slightly larger than the round viewport. One would expect the same structure for any kind of radiation that originates exclusively from the target. The elastically scattered photons show a different structure in the position spectrum, which indicates that only a small fraction came from the target. To verify this and to also check the germanium detector, the target was removed, i.e. the beam was shot through an empty slot of the target holder. For this setup, the energy spectra of the detectors were investigated. These are shown in figure 4.7. Ideally, the background spectra would not contain any photons from the incident beam that were scattered elastically some-

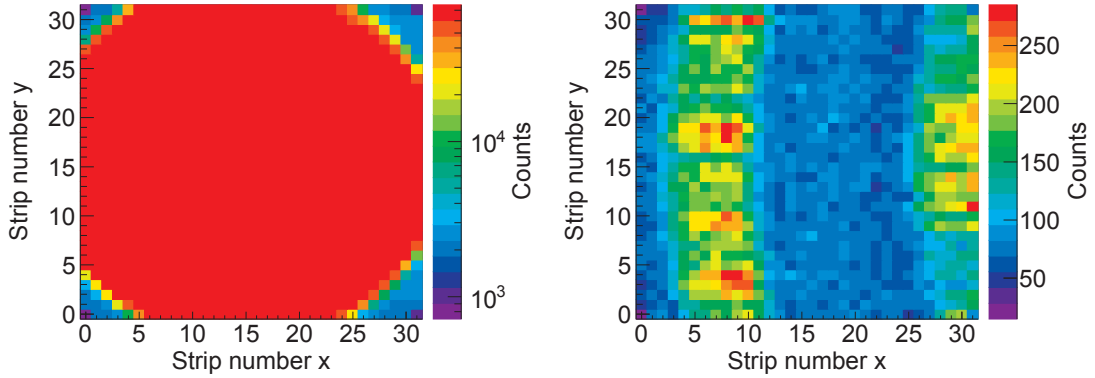

(a) (b)

Figure 4.6: Polarimeter single hit position distributions without the lead shielding shown in figure 4.3. (a) Au Kα fluorescence. (b) Elastically scattered photons.

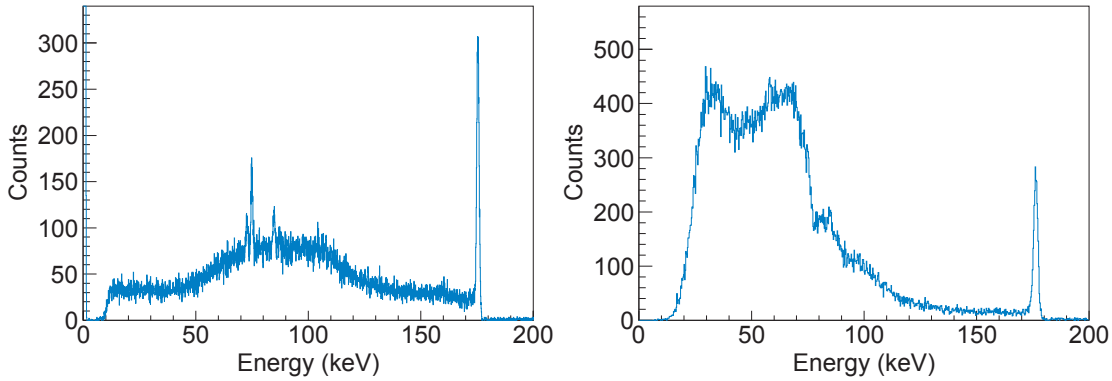

(a) (b)

Figure 4.7: Background energy spectra without the lead shielding shown in figure 4.3. (a) Ge(i). (b) Polarimeter single hits.

where. This is obviously not the case, as both spectra feature a prominent peak at 175 keV. To solve this problem, the lead shielding shown in figure 4.3 was added. Then another background run was performed to test whether the shielding could block the unwanted hits. The resulting energy spectra are shown in figure 4.8. For both detectors, the elastic peak at 175 keV is now missing, which indicates that the addition of the shielding had the desired effect. For each position of the detectors, a background run (beam on empty target holder) was performed. The recorded energy spectra were used to correct the counts in the runs with beam on target (see section 5.2.2).

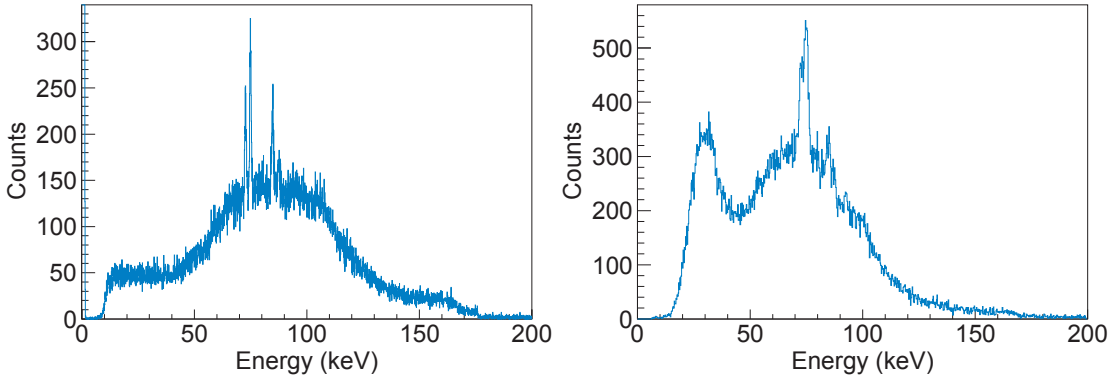

(a) (b)

Figure 4.8: Background energy spectra with the lead shielding shown in figure 4.3. (a) Ge(i). (b) Polarimeter single hits.

4.4.4 Summary of main runs

Table 4.1 summarizes the parameters of the individual runs with beam on target. Given are the target rotation (around the vertical axis, 0° corresponds to normal incidence) and for both detectors their scattering angles θ and distances between target and detector window.

Table 4.1: Parameters for beam-on-target runs.

Run	Target rotation (°)	Detector	Scattering angle (°)	Distance (mm)
1	0	Ge(i)	135	340
		Si(Li)	120	25
2a	30	Ge(i)	30	525
		Si(Li)	90	25
2b	30	Ge(i)	150	335
		Si(Li)	90	25
3	30	Ge(i)	90	415
		Si(Li)	65	15

5 Analysis

This chapter describes in detail how the data were analyzed in order to obtain the final results, namely the (angle-) differential Rayleigh scattering cross section and the linear polarization of the Rayleigh-scattered photons, of the Compton-scattered photons and of the incident PETRA-III photon beam. In section 5.1, the analysis of individual events is presented. Such an analysis results in several spectra which are then processed in a second step. This further processing can be performed independently for the determination of the differential cross section (section 5.2) and the polarization of the scattered beam (section 5.3). The relation between the polarization of the incident and the scattered photons is discussed in section 5.4.

5.1 Spectra generation

The first step of the data analysis is to calculate various quantities for individual events and sort them into spectra. This section describes the quantities that are calculated and the conditions under which the spectra are filled. For the polarimeter, different types of events are mainly distinguished by the number of strips that have recorded a valid signal. The signal of a strip is defined as valid, when the measured energy is in a certain interval. The lower limit (threshold) serves to leave out strips where the signal possibly originated from random noise. The threshold was set for each strip individually to values between 5.5 and 7 keV. For some noisy strips at the detector boundary, values of up to 16 keV were chosen. The upper energy limit was introduced when unexpected structures at high energies close to the maximum ADC value were found. This effect (possibly from the ADC) was not investigated further, instead an upper energy limit of 200 keV was set to filter out all those unwanted high-energy events. In this thesis, only events with one or two valid strips (per side of the polarimeter: front and back) are considered. These scenarios are covered in sections 5.1.1 and 5.1.2, respectively.

5.1.1 Single hit spectra

The germanium detector does not have a segmentation, therefore it can only record single hits (one measured energy per event). The energy spectrum of these events is

the starting point for the determination of the differential cross section (see section 5.2). In order to obtain a cleaner spectrum, only events with a scaler count of one are considered. Events with higher scaler counts represent scenarios, where several energy depositions occurred which may lead to a distortion in the energy measurement. For the polarimeter, single hits are defined as events where exactly one strip on each side (front and back) has a valid signal. The energy of such an event is calculated as the average of the energies recorded by front- and backside strip. The resulting spectrum allows to determine the differential cross section at the scattering angles where the polarimeter is placed. The procedure is the same as for the spectra from the germanium detector. Note, that the choice of single hits for the determination of the differential cross section from the polarimeter data is not unique. Alternatively, events with more than one valid strip per detector side could be included by summing the energies of all the valid strips (separately for both detector sides). Such a procedure would increase the statistics, but also broaden the spectrum, because the calculated sum energies contain noise contributions from several strips. The resulting degradation of resolution would be particularly critical due to the relatively high noise level from the individual strips (see section 4.2.2).

5.1.2 Double hit spectra for Compton polarimetry

In equation 3.21, the Stokes vector $\boldsymbol{S'}$ of a beam of Compton-scattered photons is given as a function of the polar and azimuthal scattering angles θ and φ, respectively, and the Stokes vector $\boldsymbol{S}_{Lab}$ of the incident photon beam. The angle-dependent intensity $I'(\theta, \varphi) = S'_0(\theta, \varphi)$ is given by

$$\begin{aligned} I'(\theta, \varphi) &= (1, 0, 0, 0) \cdot T_C(\theta) \cdot M(\varphi) \cdot \boldsymbol{S}_{Lab} \\ &\propto (1, 0, 0, 0) \cdot T_C(\theta) \cdot M(\varphi) \cdot \boldsymbol{P}_{Lab}. \end{aligned} \tag{5.1}$$

The technique of Compton polarimetry – first applied in [146] – involves a measurement of I', from which $\boldsymbol{P}_{Lab}$ is then deduced. In principle, a complete determination of $\boldsymbol{P}_{Lab}$ is possible, but the circular polarization component $P_{3,Lab}$ can only be accessed when the Compton scattering occurs in an oriented target ($T_{03} \neq 0$ in equation 3.23) [147]. Most of the used polarimeters, for example in [41, 148, 149] and also this thesis, are based on randomly oriented scatterers and therefore only sensitive to the linear polarization of the incident photon beam, i.e. $P_{1,Lab}$ and $P_{2,Lab}$. It shall be noted though, that it was proposed to detect circular polarization even in

an unpolarized scatterer by means of γ-ray tracking [150]. In that reference, an applicable energy range of 100 keV to several 10 MeV is expected, but experimental verification is still missing. As an alternative hard x-ray (linear) polarimetry technique, Rayleigh polarimetry is discussed in [151]. Like Compton polarimetry, it is based on equation 5.1, but using T_R instead of T_C.
In this section, the analysis of individual events that fill the θ-φ-spectrum is described. In order to avoid confusion with the different angles and Stokes vectors involved in the overall geometry of the experiment, their nomenclature is defined in figure 5.1.

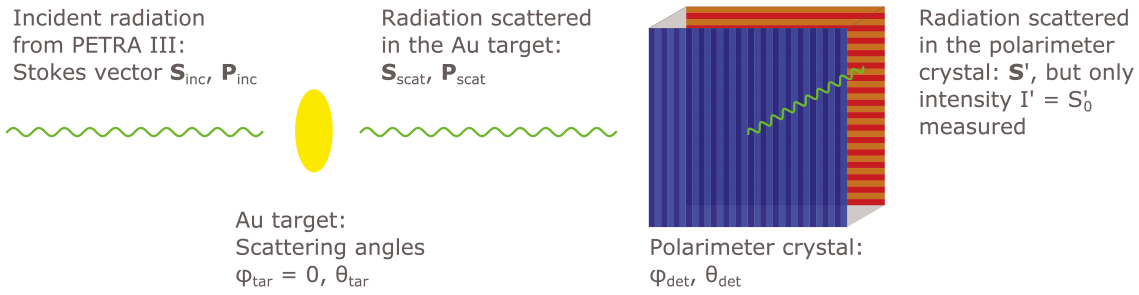

Figure 5.1: Different scattering angles and Stokes vectors involved in the experiment. Both Rayleigh- and Compton scattering in the Au target are considered, the corresponding Stokes vectors are denoted $\boldsymbol{S}_{scat}^{(R)}$ and $\boldsymbol{S}_{scat}^{(C)}$ ($\boldsymbol{P}_{scat}^{(R)}$ and $\boldsymbol{P}_{scat}^{(C)}$), respectively.

Using these definitions, equation 5.1 is applied with $\theta = \theta_{det}$, $\varphi = \varphi_{det}$ and $\boldsymbol{P}_{Lab} = \boldsymbol{P}_{scat}$. Figure 5.2 illustrates the choice the the laboratory coordinate system for Compton scattering in the strip detector, in particular the definition of φ_{det}. In order to apply Compton polarimetry, one needs to fully reconstruct Compton scattering events that occur inside the detector. For this, both the recoil electron and the Compton-scattered photon need to be absorbed. Furthermore, these two absorptions must occur at different positions. The simplest signature of such an event is a valid signal in exactly two strips on each detector side (two strips on one side and one strip on the other is also possible, this case is treated below). Let $E_{x1} > E_{x2}$ and $E_{y1} > E_{y2}$ the energies of the x- and y-strips, respectively. As only incident photons with energies below $\frac{1}{2}m_e c^2$ are considered here, the strips with E_{x1} and E_{y1} (E_{x2} and E_{y2}) can be attributed to the scattered photon (recoil electron). Averaging gives the energies of the photon and the electron:

$$E_{phot} = \frac{E_{x1} + E_{y1}}{2}, \qquad E_{elec} = \frac{E_{x2} + E_{y2}}{2} \qquad (2\ x\text{-strips},\ 2\ y\text{-strips}). \tag{5.2}$$

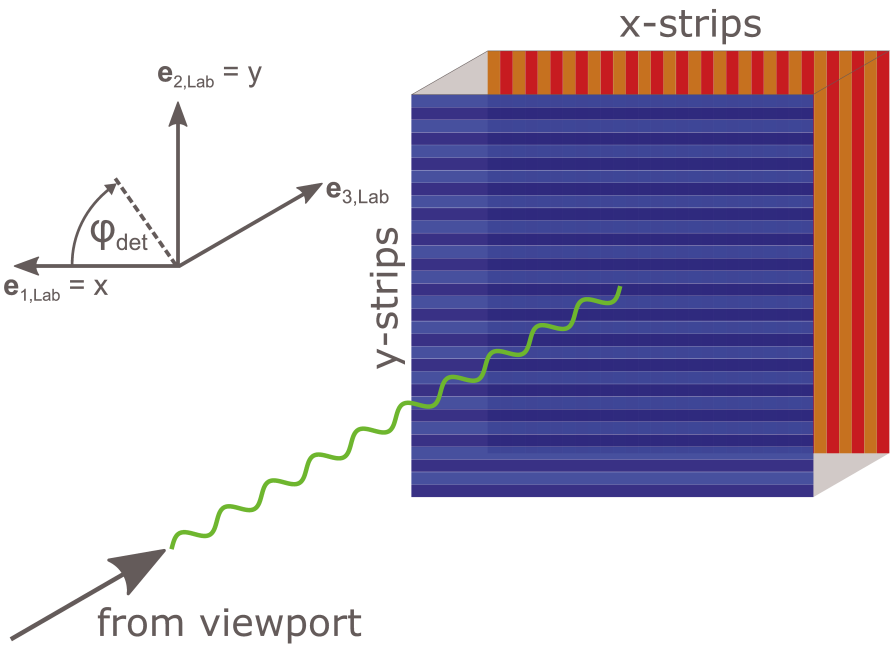

Figure 5.2: Coordinate system for scattering in the polarimeter. The y-axis corresponds to the vertical direction for all polarimeter positions during the experiment.

Using equations 2.4 and 2.5, the incident photon energy $\hbar\omega$ and the polar scattering angle θ_{det} can be calculated. Let Δn_x and Δn_y be the strip number separations between the photon and the electron in x- and y-direction, respectively. With the strip widths w_x and w_y, the spatial separations $\Delta x = \Delta n_x \cdot w_x$ and $\Delta y = \Delta n_y \cdot w_y$ are calculated. The azimuthal scattering angle φ_{det} is obtained from

$$\tan(\varphi_{det}) = \frac{\Delta y}{\Delta x}. \tag{5.3}$$

Note that equation 5.3 is only correct when the absorptions occur in the centers of the strips. In order to take into account the finite strip width, a randomization procedure for φ_{det} is applied (see section 5.3.1). The randomization is not performed during the single-event analysis, instead it is applied at a later stage using the Δn_x-Δn_y-spectrum as input. The advantage of this scheme is, that it saves computation time (compared to the randomization of φ_{det} for each event individually). On the other hand, information on θ_{det} is lost, but that can be compensated by filling the Δn_x-Δn_y-spectrum only when θ_{det} is in a certain interval $[\theta_1, \theta_2]$. A high sensitivity is achieved with an interval around $\theta_{det} = 90°$. Here, the same compromise between sensitivity and statistics as in previous works [40, 66, 152, 153] is chosen: $\theta_1 = 75°$,

$\theta_2 = 105°$. More conditions for filling the Δn_x-Δn_y-spectrum are the following:

1. The energy sums $E_{x1} + E_{x2}$ and $E_{y1} + E_{y2}$ should not differ by more than a chosen tolerance ΔE_{max} (here: $\Delta E_{max} = 6$ keV).

2. The positions of the electron and photon absorptions should be sufficiently far away from each other. Chosen criterion: $|\Delta n_x| > 1$ or $|\Delta n_y| > 1$ or both. There are two reasons for applying this condition: first, the uncertainty of φ_{det} for small distances between the interaction points is high, therefore such events do not provide significant information. Second, close-lying energy depositions may not be Compton-scattering events, instead they could arise from so-called charge sharing: there the charge cloud from a single energy deposition is spread over neighboring strips, so they both record a valid signal.

3. Energy condition: the reconstructed incident photon energy should be within a chosen interval $[E_1, E_2]$. This condition selects only the portion of the energy spectrum of the photons incident on the detector that is currently of interest. For example, the elastically scattered 175-keV photons are selected in the present analysis with $E_1 = 173$ keV, $E_2 = 178$ keV.

4. Coincidence condition: the measured time difference between the electron and the photon signal should not be more than a chosen value ΔT_{max} (here: $\Delta T_{max} = 300$ ns). Applying this condition allows to filter out (unwanted) independent energy depositions that occur during one event, but not simultaneously. As in the present experiment only the y-strips were connected to TDCs, the coincidence condition could only be checked on that detector side. A requirement for this method to work is that all involved strips have a valid TDC signal. That means that all measured energies must be above the CFD threshold of about 20 keV. For smaller incident photon energies, many recoil electrons have energies below that threshold, so that the corresponding "good" events are ignored. The lowest incident photon energy investigated in the present experiment was 116 keV, which corresponds to the peak position of the photons that were Compton-scattered in the gold target at an angle of 120°. Only in this case the coincidence condition could not be applied.

Double hits can also lead to events where two strips on one detector side and one strip on the other have a valid signal, for example one x-strip with energy E_x and

two y-strips, again with energies $E_{y1} > E_{y2}$. For such a scenario, the energies of the scattered photon and the recoil electron are calculated as

$$E_{phot} = \frac{E_{y1} \cdot E_{av}}{E_{y1} + E_{y2}}, \qquad E_{elec} = \frac{E_{y2} \cdot E_{av}}{E_{y1} + E_{y2}} \qquad (1\ x\text{-strip},\ 2\ y\text{-strips}), \tag{5.4}$$

where $E_{av} = \frac{1}{2} \cdot (E_x + E_{y1} + E_{y2})$ is the energy average of the detector front- and backside. The energy difference between detector front- and backside involves only three strips (as opposed to four, when two x- and two y-strips have a valid signal) and therefore its variance is reduced by $\frac{3}{4}$. This leads to an alteration of the filling condition (1):

$$|\Delta E| = |E_x - E_{y1} - E_{y2}| \leq \Delta E_{max} \cdot \frac{\sqrt{3}}{2}. \tag{5.5}$$

In events with one y-strip and two x-strips, the coincidence condition (4) is always assumed to be fulfilled.
For background correction, also the absolute distance between the electron and photon absorption positions

$$d = \sqrt{(\Delta x)^2 + (\Delta y)^2} \tag{5.6}$$

is calculated for each event. The d-spectrum is filled with the same conditions as the Δn_x-Δn_y-spectrum. Here a simple uniform randomization within the pixels is applied. Using the randomized values for Δx and Δy in equation 5.3, one could in principle take into account the finite pixel size for the distribution of φ_{det}. But there the more elaborated method described in section 5.3.1 is applied. It is assumed that for the background correction, the simple uniform randomization suffices, as the d-spectrum is only used to estimate the background counts (see section 5.3.2).

5.2 Differential cross section for Rayleigh scattering

According to equation 3.22, the angle-differential cross section for Rayleigh scattering $\left(\frac{\mathrm{d}\sigma}{\mathrm{d}\Omega}\right)_R$ (for a fixed photon energy) depends on the two scattering angles θ_{tar} and φ_{tar} as well as the Stokes vector of the incident beam:

$$\left(\frac{\mathrm{d}\sigma}{\mathrm{d}\Omega}\right)_R (\theta_{tar}, \varphi_{tar}) = (1, 0, 0, 0) \cdot T_R(\theta_{tar}) \cdot M(\varphi_{tar}) \cdot \boldsymbol{P}_{inc}. \tag{5.7}$$

In this section it is described how $\left(\frac{\mathrm{d}\sigma}{\mathrm{d}\Omega}\right)_R$ is extracted from the experimental data.

5.2.1 General principle

In the present experiment, a relative cross section measurement has been performed. As a normalization, the isotropic $K\alpha_1$ fluorescence line of the gold target is chosen. Such a procedure was previously applied for example in [154, 155]. The cross section for $K\alpha_1$ emission, $\left(\frac{\mathrm{d}\sigma}{\mathrm{d}\Omega}\right)_K$, is related to the Rayleigh scattering cross section via

$$\left(\frac{\mathrm{d}\sigma}{\mathrm{d}\Omega}\right)_R(\theta_{tar},\varphi_{tar}) = \frac{C_R(\theta_{tar},\varphi_{tar})}{C_K(\theta_{tar},\varphi_{tar})}\cdot\frac{\eta_K}{\eta_R}\cdot\left(\frac{\mathrm{d}\sigma}{\mathrm{d}\Omega}\right)_K. \tag{5.8}$$

The quantities C_R, C_K are the measured line strengths (integrated counts) of the Rayleigh and $K\alpha_1$ peak, respectively, at the given detector position $(\theta_{tar},\varphi_{tar})$. Their ratio is corrected with the detector efficiencies $\eta_R = \eta(175\text{ keV})$ and $\eta_K = \eta(68.803\text{ keV})$. The main analysis task is the determination of C_R and C_K which is described in sections 5.2.2 and 5.2.3. Brief comments on η and $\left(\frac{\mathrm{d}\sigma}{\mathrm{d}\Omega}\right)_K$ are given in sections 5.2.4 and 5.2.5, respectively. Error estimations are discussed in section 5.2.6.

5.2.2 Background correction

The line strengths of the Rayleigh and $K\alpha_1$ peak are obtained from the energy spectrum. This may either be the spectrum of the germanium detector or the single hit spectrum of the polarimeter. Let $c_{tot}[i]$ be the measured counts in bin i of the energy spectrum. The index *tot* (total) indicates, that both signal (from target) and background (from somewhere else than the target) are included. In order to improve the line strength determination, the background counts $c_{bg}[i]$ are subtracted from the total counts to obtain the corrected counts

$$c_{cor}[i] = c_{tot}[i] - c_{bg}[i]. \tag{5.9}$$

The energy distribution of the background was measured in a run without target (see section 4.4.3). Let $\tilde{c}_{bg}[i]$ be the content in bin i of such a spectrum. The background contribution in the spectrum with target is obtained via a scaling factor λ:

$$c_{bg}[i] = \lambda\cdot\tilde{c}_{bg}[i]. \tag{5.10}$$

A first estimation for λ is made from the measurement times t (with target) and $\tilde{t}$ (without target):

$$\lambda = \frac{t}{\tilde{t}}. \tag{5.11}$$

The underlying assumption for equation 5.11 is that the mean background rate is the same for the measurements with and without target. But since the background includes events that originate from the incident beam (but not from the target), the background rate varies with the intensity of the incident beam. The latter has not been monitored, therefore the validity of the scaling factor given by equation 5.11 cannot be checked. The value is only used as a starting point for a determination of λ "by hand". There, λ is varied with the goal to achieve the following properties in the background-corrected spectrum $c_{cor}[i]$:

- Features clearly related to the background such as lead fluorescence lines are reduced as much as possible.
- Negative bin contents are kept to a minimum.
- Unphysical dips in the spectrum are avoided.

Examples of raw and background-corrected spectra for both detectors are shown in figure 5.3. The main features of the energy spectra are the following:

- Fluorescence lines from the gold target: $K\alpha_2$ (66.989 keV), $K\alpha_1$ (68.803 keV), $K\beta_3$ (77.580 keV), $K\beta_1$ (77.984 keV), $K\beta_2$ (80.150 keV) [156]. "Au" is omitted in figure 5.3. Due to the finite energy resolution, not all lines can be resolved.
- Compton profile (C): this broad feature arises from photons that are Compton-scattered in the gold target. The peak position varies with the scattering angle θ_{tar} according to equation 2.4.
- Rayleigh peak (R): photons that are elastically scattered in the gold target form a narrow peak at the incident beam energy of 175 keV.
- Pile-up: when the time interval between two energy depositions in the detector is short enough, the ADC registers them as only one event with the recorded energy being roughly the sum of the two energies. Pile-up consisting of two gold fluorescence photons is observed in the spectrum of the germanium detector (figure 5.3a). In the spectrum of the polarimeter (figure 5.3b), the

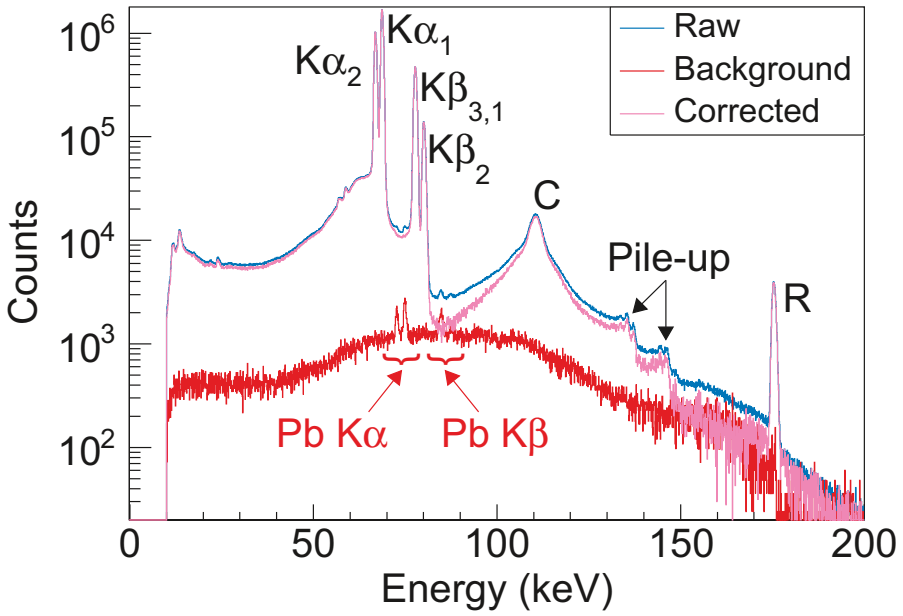

(a)

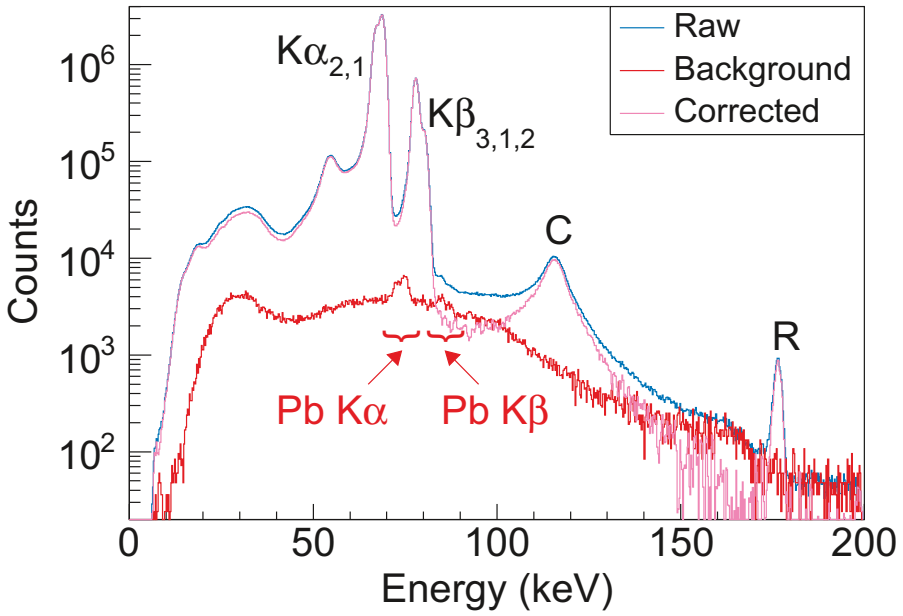

(b)

Figure 5.3: Raw (total) and background-corrected energy spectra. (a) Germanium detector at $\theta_{tar} = 135°$. (b) Si(Li) polarimeter at $\theta_{tar} = 120°$. See text for details on the indicated features.

effect is missing. This can be explained with the segmentation: a pile-up event requires that two energy depositions occur in the same strip (on both detector

sides). The probability for this scenario is negligible at the photon flux in this experiment.

- Fluorescence lines from the lead environment: this feature is not related to the target and therefore occurs in the total and in the background spectrum. Applying the background correction 5.9 removes the lead fluorescence lines.

5.2.3 Peak area determination

The counts of the $K\alpha_1$ and the Rayleigh peak are determined from the background-corrected energy spectrum. A straightforward approach would be to add the bin contents in a suitable region around each peak. But this method cannot be applied here due to the reasons, that can be observed in figure 5.3. First, background contributions (originating from the target) are present. These include – among others – the wings of the Compton profile and recoil electrons from 175-keV photons that are Compton-scattered in the detector and where the scattered photon escapes. Second, there is a strong overlap between the $K\alpha_1$ and $K\alpha_2$ line. The method chosen here to take into account these problems is a χ^2 fit of the peaks. In a region around a peak, a function $g(E)$ is fitted to the spectrum. The fit function is the sum of a peak shape $f(E)$ and a background term. For simplicity, the latter is assumed to be linear. Due to the $K\alpha_1/K\alpha_2$ overlap, a simultaneous fit of these two lines is performed. The area of a peak is obtained by integrating $f(E)$ and the counts C as

$$C = \frac{1}{w_{bin}} \int f(E)\mathrm{d}E, \tag{5.12}$$

where w_{bin} is the bin width. In the following, the shape of the peak function $f(E)$ will be discussed. Since it is not known entirely, different shapes are tried and compared. Not all the shapes are accepted, in cases where it is already clear "by eye" that the function does not describe the data, it is rejected. The resulting variations of C are used for a measure of the error introduced by the fitting procedure. Different forms of $f(E)$ are constructed here from additive building blocks $f_i(E)$. These functions were proposed earlier and can be found in [157]. Each function is written as the product of an amplitude A_i and a functional form that depends on further fit parameters B_j. Starting point is a gaussian with centroid μ and standard deviation σ. For better readability, these parameters are not written as B_j. In order to account for asymmetric peaks, the gaussian term is modified with an asymmetry parameter B_1:

$$f_1(E) = \frac{A_1 \cdot \sqrt{2}}{\sqrt{\pi}\sigma\,(1+B_1)} \cdot \begin{cases} \exp\left(-\frac{(E-\mu)^2}{2\sigma^2}\right) & E \leq \mu \\ \exp\left(-\frac{(E-\mu)^2}{2(\sigma B_1)^2}\right) & E > \mu \end{cases} . \tag{5.13}$$

This is the dominant term in $f(E)$, the following contributions are regarded as corrections. The first one is a function with step-like behavior:

$$f_2(E) = \frac{A_2}{\sqrt{2\pi}\sigma\,(1+B_1)} \cdot \mathrm{erfc}\left(\frac{E-\mu}{\sigma B_2}\right). \tag{5.14}$$

The parameter B_2 is not present in the formula in [157] (table 1, number B6b). It is introduced here to allow a width of the step that is different from the value of the gaussian. In addition to a step, also tails on both sides of the gaussian are considered here. Two functional forms for the tails are used. The first form results from a convolution of a gaussian with an exponential decay. As indicated in [158], it is usually assumed that the gaussian in this convolution has the same standard deviation σ as the one in f_1. With this, the tail has the form:

$$f_3(E) = \frac{A_3}{2\sigma|B_3|} \cdot \exp\left(\frac{E-\mu}{\sigma B_3} + \frac{1}{2B_3^2}\right) \cdot \mathrm{erfc}\left[\mathrm{sign}(B_3) \cdot \left(\frac{E-\mu}{\sqrt{2}\sigma} + \frac{1}{\sqrt{2}B_3}\right)\right]. \tag{5.15}$$

The parameter B_3 governs the tail width. Positive (negative) values correspond to a tail on the low-energy (high-energy) side of the main peak. The second tail function is given by

$$f_4(E) = \frac{A_4 \cdot \Gamma(n)}{\Gamma\left(n - \frac{1}{|B_4|}\right) \cdot \Gamma\left(\frac{1}{|B_4|}\right) \cdot \sigma} \cdot \frac{\exp\left(\frac{E-\mu}{\sigma B_4}\right)}{\left[1 + \exp\left(\frac{E-\mu}{\sigma} \cdot \mathrm{sign}\,(B_4)\right)\right]^n} \tag{5.16}$$

with $\Gamma()$ being Euler's gamma function. As B_3 in f_3, B_4 determines the tail width and its sign the side of the main peak. The exponent $n > 0$ parametrizes the function (it does not act as a fit parameter). In [159], $n = 4$ was chosen. At the beginning, this was used here, too. Later, $n = 10$ was selected, since it allows a lower limit for the width $|B_4|_{min} = \frac{1}{n}$. Values of B_4 closer to zero would cause f_4 to diverge. The tails are used pairwise, which means that the fit function always includes a low-energy- and a high-energy tail of the same type (f_3 or f_4 or none), but with independent fit parameters. Combinations of the following variations were performed to construct different peak shape functions $f(E)$:

- Fix B_1 to 1 or not.
- Enable a step or not.
- Set different upper limits for the step height (relative to the gaussian height).
- Use f_3, f_4 or no tails.
- Use f_4 with $n = 4$ or $n = 10$.
- Set different upper limits for the tail area (relative to the gaussian area).

For the simultaneous fit of $K\alpha_1$ and $K\alpha_2$, one fit function $f(E)$ for each peak enters the total fit function $g(E)$. The following restrictions are imposed:

- The used steps and tails are the same for both peaks and they scale with the line strength, i.e. the following parameters are common for both peaks: A_2/A_1, B_2, A_3/A_1 (A_4/A_1), B_3 (B_4).
- The line strength ratio of $K\alpha_1$ and $K\alpha_2$ is fixed to the theoretical value (taking into account the detector efficiency). This measure is indispensable in particular for the polarimeter spectra because the more pronounced $K\alpha_1/K\alpha_2$ overlap (compared to the germanium detector) would otherwise result in a highly unstable fit. The theoretical line strength ratio is obtained from the relative intensities found in [156].

Figure 5.4 shows example fits of the $K\alpha$ and Rayleigh peaks. The fits of the Rayleigh peak in figure 5.4b and 5.4d are presented together with the individual components f_i of the fit function. The background components are omitted as they coincide with zero on the given scales. Note that the centroids of the Rayleigh peaks clearly deviate from the incident beam energy of 175 keV. This can be explained with a poor calibration: the reference lines in the calibration (see section 4.4.2) are all relatively far away 175 keV, therefore the calibration is inaccurate in this energy region. The effect is more pronounced for the polarimeter than for the Germanium detector, as for the polarimeter calibration only reference lines below 175 keV are used. For the differential cross section determination such a shift of the peak is not a problem as only the peak counts are relevant. In order to obtain the final line strength C_i for a certain line $i = K, R$, let J be the number of accepted fit functions and C_{ij},

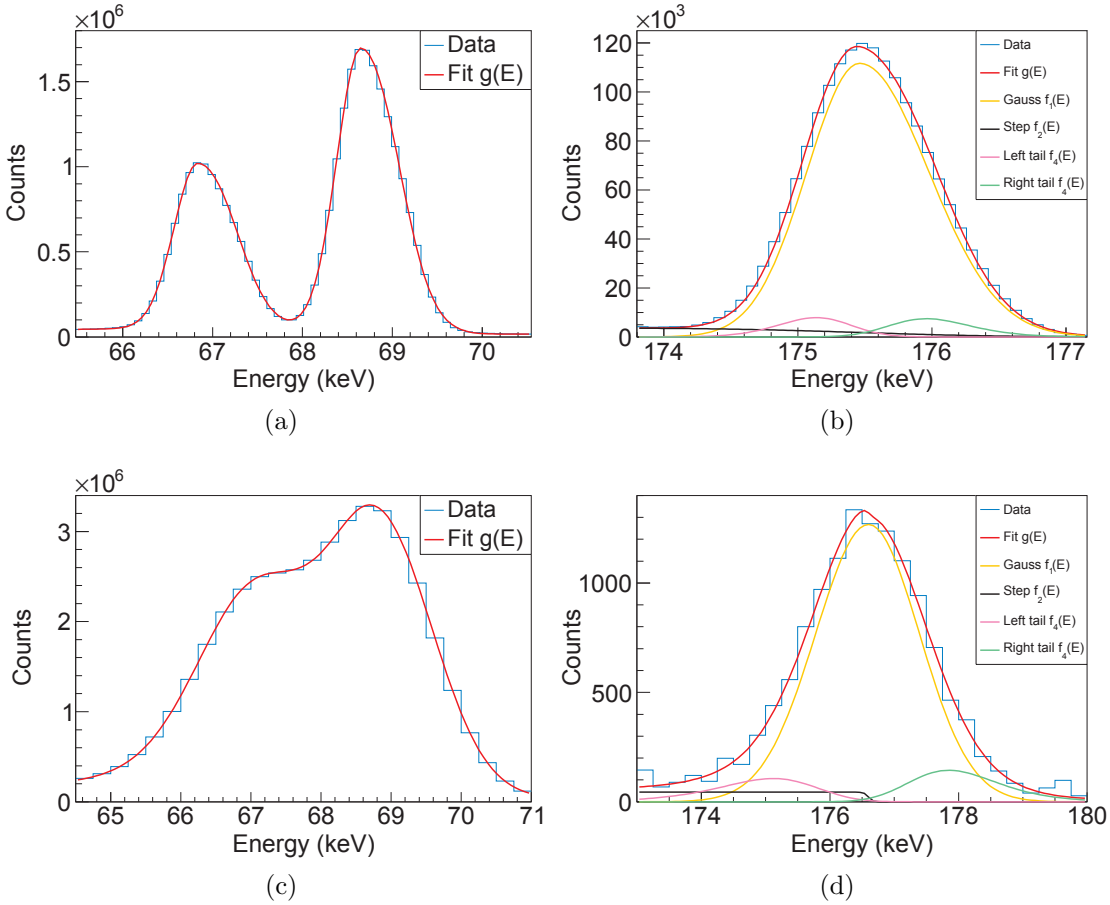

Figure 5.4: Fits of the $K\alpha$ and Rayleigh peaks. (a) Germanium detector at $\theta_{tar} = 135°$, $K\alpha$. (b) Germanium detector at $\theta_{tar} = 30°$, Rayleigh. (c) Si(Li) polarimeter at $\theta_{tar} = 120°$, $K\alpha$. (d) Si(Li) polarimeter at $\theta_{tar} = 120°$, Rayleigh.

$j = 1, \ldots, J$ the corresponding values from each fit. C_i is calculated as the mean:

$$C_i = \frac{1}{J} \sum_{j=1}^{J} C_{ij}. \tag{5.17}$$

5.2.4 Detector efficiency

The energy-dependent (relative) efficiencies $\eta(E)$ in equation 5.8 are obtained differently for the two detectors. For the germanium detector, data from a previous efficiency measurement [160] are available in form of the following parametrization:

$$\eta(E) = \exp\left[\sum_{i=0}^{5} \zeta_i \cdot [\log(E/\mathrm{keV})]^i\right]. \tag{5.18}$$

The polarimeter efficiency is estimated from a Monte Carlo simulation. The EGS5 [161] code is provided by G. Weber [162] and has been applied previously [163]. In the code, values for the electronic noise of the strips σ_{noise} can be specified. The current implementation only allows one global value for all x- and one value for all y-strips. As a refinement, both noise levels are set to zero and the stored energies are randomized (gaussian) in a second step. The noise levels then used are set for each strip individually – with values directly obtained from experimental data. For the determination of the latter, the ^{133}Ba calibration spectra (available for each strip) are used. In such a spectrum the isolated and sufficiently intense 81-keV line is fitted with a simulated spectrum. The underlying simulation shall mimic the calibration source: it simulates an irradiation of the entire detector with unpolarized 81-keV photons and again the electronic noise is set to zero. This gives simulated histograms of the 81-keV line for each strip individually. The fit function $g(E)$ is constructed as a convolution of the simulated histogram and a gaussian, together with a quadratic background. Since the gaussian width (standard deviation) σ_{noise} enters as a fit parameter, the fitting becomes non-trivial. In this thesis, the RooFit package [164] is used, which provides methods for such a task. A fit example and the results for all strips are shown in figure 5.5.

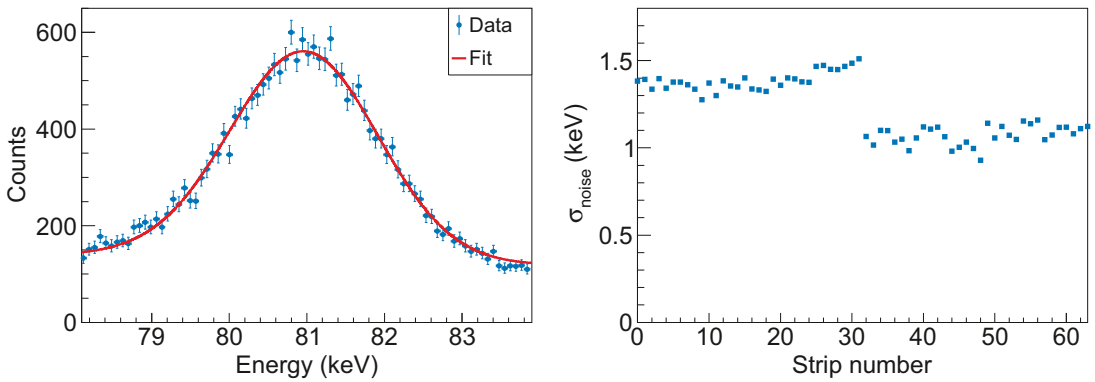

(a) (b)

Figure 5.5: Fit of the 81-keV ^{133}Ba line using a simulated spectrum convoluted with a gaussian. (a) Example fit of strip 48. (b) Resulting values of σ_{noise} for all strips. The strip numbering is defined in figure 4.4b.

5.2.5 Normalization

In order to calculate an absolute Rayleigh scattering cross section, a value for the $K\alpha_1$ cross section $\left(\frac{\mathrm{d}\sigma}{\mathrm{d}\Omega}\right)_K$ needs to be provided to apply equation 5.8. In this thesis, $\left(\frac{\mathrm{d}\sigma}{\mathrm{d}\Omega}\right)_K$ is calculated according to

$$\left(\frac{\mathrm{d}\sigma}{\mathrm{d}\Omega}\right)_K = \sigma_{ion,K} \cdot \omega_K \cdot p(K\alpha_1) \cdot \frac{1}{4\pi} \tag{5.19}$$

The cross section for the ionization of the gold K-shell at 175 keV is labeled $\sigma_{ion,K}$ and its theoretical value is provided by A. Surzhykov [165]. A reference value for the gold K-shell fluorescence yield ω_K is taken from [166]. The quantity $p(K\alpha_1)$ denotes the probability for gold that in the event of fluorescence, it is $K\alpha_1$ emission. It is calculated from the relative intensities of the strongest lines, namely $K\alpha_1$, $K\alpha_2$, $K\beta_1$, $K\beta_2$ and $K\beta_3$. Reference values for the relative intensities are taken from [156]. The factor $\frac{1}{4\pi}$ relates the total to the differential cross section assuming isotropic emission.

5.2.6 Error estimation for the differential cross section

Several error sources are taken into account for the final result $\left(\frac{\mathrm{d}\sigma}{\mathrm{d}\Omega}\right)_R$. For the experimentally determined quantities C_i $(i = K, R)$ statistical errors are calculated conservatively using the smallest value C_{ij} from the accepted fit functions $j = 1, \ldots, J$:

$$\frac{\Delta C_{i,stat}}{C_i} = \max_j \left\{ \frac{1}{\sqrt{C_{ij}}} \right\}. \tag{5.20}$$

Additionally, an uncertainty of the fitting procedure is estimated as

$$\frac{\Delta C_{i,fit}}{C_i} = \max_j \left| \frac{C_{ij} - C_i}{C_{ij}} \right|. \tag{5.21}$$

The overall relative error of C_i is estimated as a sum in squares of the two mentioned contributions:

$$\frac{\Delta C_i}{C_i} = \sqrt{\left(\frac{\Delta C_{i,stat}}{C_i}\right)^2 + \left(\frac{\Delta C_{i,fit}}{C_i}\right)^2}. \tag{5.22}$$

The relative error of the line strength ratio is given by

$$\Delta\left(\frac{C_R}{C_K}\right)\Big/\left(\frac{C_R}{C_K}\right) = \sqrt{\left(\frac{\Delta C_R}{C_R}\right)^2 + \left(\frac{\Delta C_K}{C_K}\right)^2}. \tag{5.23}$$

It is calculated individually for each detector position $(\theta_{tar}, \varphi_{tar})$. A systematic error, that is common for all detector positions, comes from the uncertainties of the efficiency ratio and the cross section normalization. The main contributions are expected to be the K-shell ionization cross section (relative error: 5 %) and the efficiency ratio (relative error: 5 %, as also estimated previously [167]). The overall systematic Rayleigh differential cross section error is estimated to be 8 %.

5.3 Polarization analysis

This section describes, how a Δn_x-Δn_y-spectrum (filled with suitable conditions, see section 5.1.2) is analyzed to extract the Stokes vector $\boldsymbol{P}_{Lab}$ of the radiation incident on the polarimeter. As mentioned before, the radiations investigated in this thesis are the photons that are Rayleigh- and Compton-scattered in the gold target and the corresponding Stokes vectors are $\boldsymbol{P}_{Lab} = \boldsymbol{P}_{scat}^{(R)}$ and $\boldsymbol{P}_{Lab} = \boldsymbol{P}_{scat}^{(C)}$, respectively. The fundamental concept is the relation between the θ_{det}-φ_{det}-distribution and $\boldsymbol{P}_{Lab}$ given by equation 5.1. In order to take into account detector effects, an angle-dependent detection efficiency $\eta(\theta_{det}, \varphi_{det})$ is introduced:

$$I'(\theta_{det}, \varphi_{det}) = \eta(\theta_{det}, \varphi_{det}) \cdot (1, 0, 0, 0) \cdot T_C(\theta_{det}) \cdot M(\varphi_{det}) \cdot \boldsymbol{S}_{Lab}. \tag{5.24}$$

Since the information on θ_{det} is lost in the Δn_x-Δn_y-spectrum (all events with $\theta_1 \leq \theta_{det} \leq \theta_2$ are included), only the the one-dimensional φ_{det}-distribution is of interest:

$$I'(\varphi_{det}) = \int_{\theta_1}^{\theta_2} \mathrm{d}\theta'\ I'(\theta', \varphi_{det}) =: \boldsymbol{V}^T(\varphi_{det}) \cdot \boldsymbol{S}_{Lab}. \tag{5.25}$$

To apply equation 5.25 (as a fit function), the experimental φ_{det}-spectrum must be available. Section 5.3.1 describes how it is obtained from the measured Δn_x-Δn_y-spectrum. A refinement of the analysis is achieved when background-corrected data are used. This background correction is described in section 5.3.2. In section 5.3.3 it is shown how the unknown function $\boldsymbol{V}$ in equation 5.25 is estimated by means of Monte Carlo simulations. The bootstrap method is applied to the analysis steps from

the sections 5.3.1 to 5.3.3. This serves to obtain estimates for the statistical errors of the Stokes parameters. Detailed descriptions of the involved randomizations are given in section 5.3.4.

5.3.1 Randomization of φ_{det} in finite-size pixels

The simplest way to transform the Δn_x-Δn_y- into the φ_{det}-distribution is the application of equation 5.3. But it does not take into account, that the energy depositions are in general occurring at different positions within the pixels and therefore smearing out the φ_{det}-distribution. In the following it is described how this effect is modeled. Starting point are pixels 1 and 2 where the Compton recoil electron and scattered photon, respectively, are absorbed. The relative position of these pixels defines Δn_x and Δn_y. The absorption positions inside the pixels are given by the coordinates (x_1, y_1) and (x_2, y_2). The relative coordinates are $\Delta x = x_2 - x_1$ and $\Delta y = y_2 - y_1$. From these the absolute distance between the absorption points d and the angle φ_{det} are calculated according to equations 5.6 and 5.3, respectively. Figure 5.6 illustrates this scenario. The finite pixel size defines certain limits for the

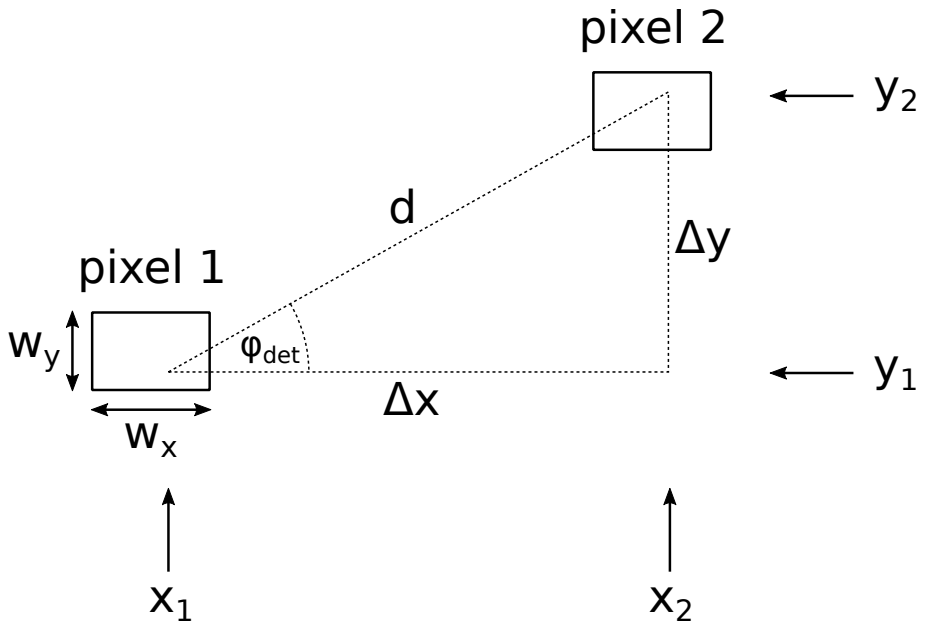

Figure 5.6: Geometry of a Compton scattering event inside the polarimeter. Pixels (pseudo-pixels) are formed through the combination of the front- and backside strip structure. The pixels in the present scenario are square, but the proposed method for the φ_{det}-randomization does not require that.

coordinates of the absorption positions:

$$\begin{aligned} x_1 &\in [x_{1,min}, x_{1,max}], \qquad y_1 \in [y_{1,min}, y_{1,max}], \\ x_2 &\in [x_{2,min}, x_{2,max}], \qquad y_2 \in [y_{2,min}, y_{2,max}]. \end{aligned} \tag{5.26}$$

They imply limits for φ_{det} and d:

$$\varphi_{det} \in [\varphi_{min}, \varphi_{max}], \qquad d \in [d_{min}, d_{max}]. \tag{5.27}$$

With the intervals given by 5.26 and 5.27, the set

$$\Omega := [x_{1,min}, x_{1,max}] \times [y_{1,min}, y_{1,max}] \times [\varphi_{min}, \varphi_{max}] \times [d_{min}, d_{max}] \tag{5.28}$$

is constructed. This set contains – but is not limited to – all possible combinations of absorption positions (x_1, y_1) and (x_2, y_2) in the two pixels. The next step is to derive a probability density $f_{\boldsymbol{R}}(\boldsymbol{r})$ for the vector $\boldsymbol{r} := (x_1, x_2, \varphi_{det}, d)^T$ on Ω. This density is constructed under the following assumptions:

- The components of $\boldsymbol{r}$ are independent.
- The position in pixel 1 (x_1, y_1) is distributed uniformly.
- The interval $[\varphi_{min}, \varphi_{max}]$ is small enough so that the distribution of φ_{det} is approximately uniform.
- The distribution of d follows an exponential decay.

The probability density $f_{\boldsymbol{R}}(\boldsymbol{r})$ then becomes

$$f_{\boldsymbol{R}}(\boldsymbol{r}) \propto \exp\left(-\frac{d}{\tau}\right). \tag{5.29}$$

The exponential decay is governed by the mean free path length $\tau = (\frac{\mu}{\rho} \cdot \rho)^{-1}$ where the mass attenuation coefficient $\frac{\mu}{\rho}$ and the mass density ρ are properties of the detector material. Reference values for ρ and $\frac{\mu}{\rho}$ are taken from [123] and [81], respectively. In order to determine the distribution of φ_{det} with the condition, that pixel 2 is hit, the following variable transformation is introduced:

$$\boldsymbol{x} = \begin{pmatrix} x_1 \\ y_1 \\ x_2 \\ y_2 \end{pmatrix} = \begin{pmatrix} x_1 \\ y_1 \\ x_1 + d \cdot \cos(\varphi_{det}) \\ y_1 + d \cdot \sin(\varphi_{det}) \end{pmatrix}. \tag{5.30}$$

The Jacobi determinant is given by

$$\left|\frac{\partial \boldsymbol{x}}{\partial \boldsymbol{r}}\right| = d. \tag{5.31}$$

This leads to the probability density of the transformed variables

$$f_{\boldsymbol{X}}(\boldsymbol{x}) \propto \frac{1}{d(\boldsymbol{x})} \cdot \exp\left(-\frac{d(\boldsymbol{x})}{\tau}\right) =: w(\boldsymbol{x}), \tag{5.32}$$

where $d(\boldsymbol{x})$ is given by equation 5.6. The following recipe is used to obtain a numeric estimate of the φ_{det}-distribution:

1. Choose a (four-dimensional) grid for $\boldsymbol{x}$ on the intervals in equation 5.26.
2. Create a histrogram for φ_{det} with limits φ_{min} and φ_{max} and a binning of choice.
3. Loop over the grid and evaluate φ_{det} and $w(\boldsymbol{x})$ for each point $\boldsymbol{x}$. Fill the φ_{det}-histogram with weight $w(\boldsymbol{x})$.

If instead of the φ_{det}-histogram the two-dimensional φ_{det}-d-histogram is required, the same procedure can be applied. It was found that a smoother resulting φ_{det}-histogram is obtained when the components of $\boldsymbol{x}$ are randomized uniformly within the step size of the grid. Note that $\frac{\mu}{\rho}$ depends on the energy of the scattered photon. As an approximation, a constant value is used which corresponds to the energy of a photon scattered at $\theta_{det} = 90°$. If the energy of the incident photons is varied though, $\frac{\mu}{\rho}$ changes and therefore also τ, which requires a new calculation of the φ_{det}-histogram for the combination of the pixels 1 and 2. Both φ_{det} and w do not explicitly depend on the individual coordinates, but only on the differences Δx and Δy. A φ_{det}-histogram can therefore be created using – aside of τ – only Δn_x, Δn_y and the pixel dimensions (strip widths) as input. Examples of φ_{det}-histograms are shown in figure 5.7.
In order to transform the entire Δn_x-Δn_y- into a φ_{det}-spectrum, the following steps are performed for each bin $(\Delta n_x, \Delta n_y)$:

1. Create a φ_{det}-histogram as described above.
2. If N is the number of counts in the bin $(\Delta n_x, \Delta n_y)$, get N samples from the φ_{det}-histogram and fill them into the final φ_{det}-spectrum. The sampling routine for arbitrary one-, two- and three-dimensional histograms is readily available within the ROOT framework [168]. It is based on the inversion method [169], also known as inversion transform sampling.

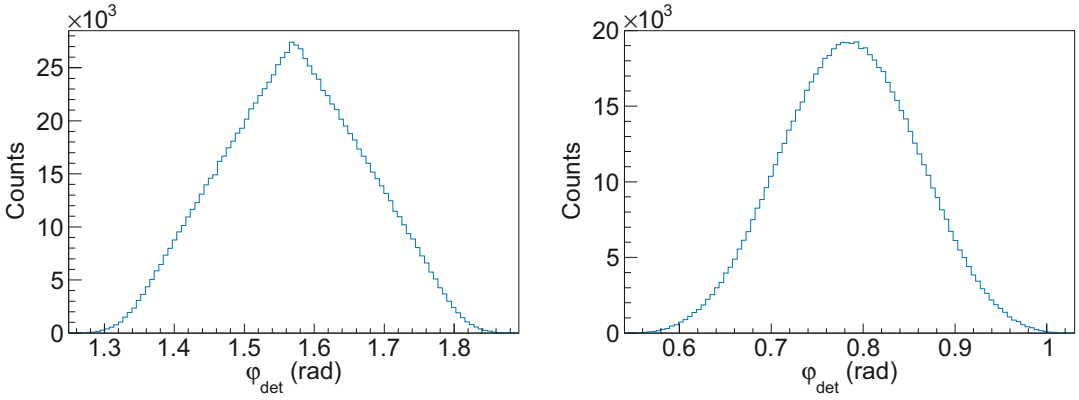

(a) (b)

Figure 5.7: Histograms for the randomization of φ_{det} to account for the finite pixel size. (a) $\Delta n_x = 0$, $\Delta n_y = 4$. (b) $\Delta n_x = 4$, $\Delta n_y = 4$.

5.3.2 Background correction

The scenario here is similar to the one in section 5.2.2: signal (Lab) and background (bg) counts contribute to the total measured intensity $I'_{tot}(\varphi_{det})$. It is assumed that signal and background are superposed incoherently which allows the following partition of the total Stokes vector [131]:

$$\boldsymbol{S}_{tot} = \boldsymbol{S}_{Lab} + \boldsymbol{S}_{bg}. \tag{5.33}$$

Applying equation 5.25 yields

$$I'_{Lab}(\varphi_{det}) = \boldsymbol{V}^T(\varphi_{det}) \cdot (\boldsymbol{S}_{tot} - \boldsymbol{S}_{bg}) = I'_{tot}(\varphi_{det}) - I'_{bg}(\varphi_{det}). \tag{5.34}$$

The background φ_{det}-spectrum $I'_{bg}(\varphi_{det})$ is obtained from the background Δn_x-Δn_y-spectrum using the randomization procedure described in section 5.3.1. In the following it is explained how the required Δn_x-Δn_y-distribution of the background is estimated. The determination is split into two parts. First, the number of background events N_{bg} is estimated. This estimation is shown for the background of the Rayleigh peak in figure 5.8. A linear background is fitted left and right of the Rayleigh peak and these two parts are merged under the peak at their crossing point. The integral of the resulting function (divided by the bin width) in the same interval as chosen for the energy condition (here: 173 to 178 keV, see section 5.1.2) gives N_{bg}. The second ingredient for the background Δn_x-Δn_y-distribution is its shape. It is estimated from the Δn_x-Δn_y-distribution in an (incident photon) energy interval near

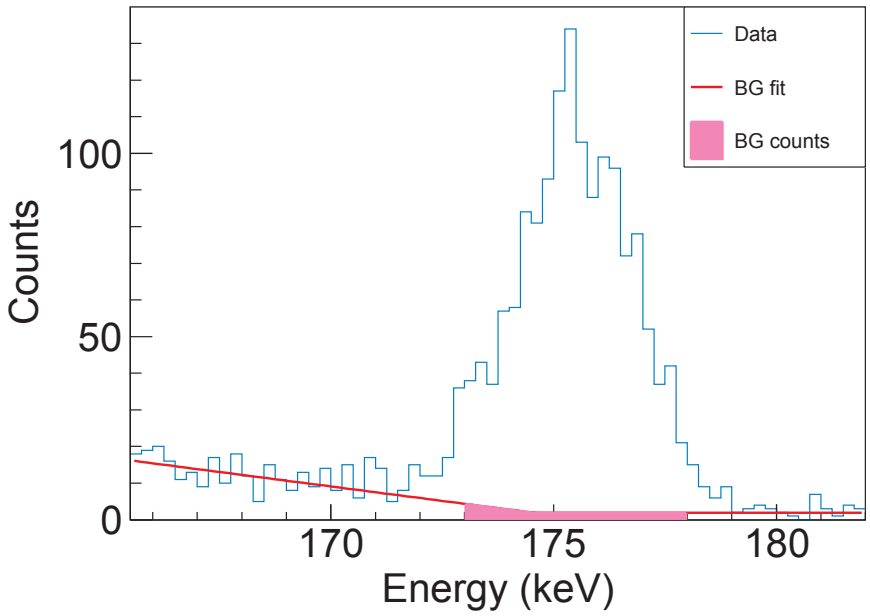

Figure 5.8: Incident photon energy spectrum of reconstructed Compton scattering events inside the polarimeter. A linear fit left and right of the Rayleigh peak is shown together with the area of the fit function under the peak.

the peak (chosen here: 166 to 171 keV), let this be called $I'_{bg,0}(\Delta n_x, \Delta n_y)$. This procedure can be justified when the background Δn_x-Δn_y-distribution changes slowly with energy, which is assumed here. The final background Δn_x-Δn_y-distribution $I'_{bg}(\Delta n_x, \Delta n_y)$ is obtained by sampling $I'_{bg,0}$ N_{bg} times. This background correction procedure can only be applied to narrow peaks. Therefore a different scheme is used to estimate the background of the broad Compton peak. Since the shape of the background distribution cannot be accessed, it is assumed to be uniform. The background counts N_{bg} are estimated from the spectrum of d. For this the d-spectrum is fitted with a Monte-Carlo-generated d-histogram:

$$g(d_i) = A \cdot c_{sim}[i]. \tag{5.35}$$

Equation 5.35 represents the evaluation of the fit function g at d_i, the center of the i^{th} bin. The counts in the same bin of the simulated histogram are denoted $c_{sim}[i]$, A is the fit parameter. The signal counts are the total counts of the simulated histogram multiplied with A. This number is subtracted from the total counts of the experimental d-spectrum to obtain N_{bg}. Such a procedure relies on the fact, that the fit function g given by equation 5.35 only describes the d-spectrum in a certain

range where the background is negligible. If, for simplicity, a constant background is assumed, that range lies in the region of small distances where the counts are high. The fit interval is restricted to that range, here it is chosen to extend from 0 to 4 cm. Figure 5.9 shows an example of a d-spectrum together with its fit. In order to take into account effects of the detector's strip structure, the assumed

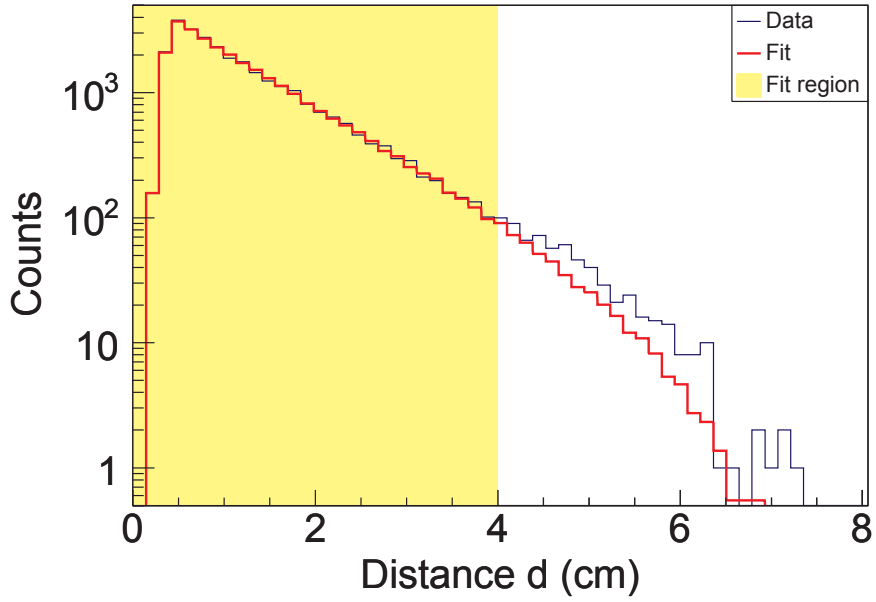

Figure 5.9: Distribution of the absolute distance between the recoil electron and the Compton-scattered photon inside the polarimeter. Data are fitted with a simulated distribution in the indicated region.

unpolarized background is converted into a Δn_x-Δn_y-distribution $I'_{bg,0}$ (even though it is then converted back to φ_{det}-distribution). A Monte Carlo simulation is in principle possible, but here a simpler scheme is applied: samples are generated for x_1, y_1 and φ_{det} from uniform distributions and for d from an exponential distribution (again with decay length τ). With x_1 and y_1 being centered around 0, the strip number differences can be calculated as

$$\Delta n_x = \frac{x_1 + d \cdot \cos(\varphi_{det})}{w_x}, \qquad \Delta n_y = \frac{y_1 + d \cdot \sin(\varphi_{det})}{w_y}. \tag{5.36}$$

These then fill the histogram $I'_{bg,0}(\Delta n_x, \Delta n_y)$, here 100000 samples are generated. As before, the background spectrum to be subtracted I'_{bg} is obtained by sampling $I_{bg,0}$ N_{bg} times.

5.3.3 Fit with Monte Carlo spectra

To generate Monte Carlo simulated Δn_x-Δn_y-histograms, the same code as for the polarimeter efficiency (see section 5.2.4) is used. With σ_{noise} available for each strip, simulations of the detector response are performed setting the following Stokes parameters for the incident photons:

$$\boldsymbol{S}_1 = \begin{pmatrix} S_{0,1} \\ S_{0,1} \\ 0 \\ 0 \end{pmatrix}, \quad \boldsymbol{S}_2 = \begin{pmatrix} S_{0,2} \\ -S_{0,2} \\ 0 \\ 0 \end{pmatrix}, \quad \boldsymbol{S}_3 = \begin{pmatrix} S_{0,3} \\ 0 \\ S_{0,3} \\ 0 \end{pmatrix}, \quad \boldsymbol{S}_4 = \begin{pmatrix} S_{0,4} \\ 0 \\ -S_{0,4} \\ 0 \end{pmatrix}. \tag{5.37}$$

These correspond to 100 % polarized beams with polarization tilts being 0°, 90°, 45° and 135° with respect to the horizontal plane. The intensities $S_{0,j}$ $(j = 1, \ldots, 4)$ are the numbers of simulated events, which are chosen to be 10^8 in all cases. A linear combination of these Stokes vectors is used to parametrize the unknown Stokes vector

$$\boldsymbol{S}_{Lab} = \sum_{j=1}^{4} W_j \boldsymbol{S}_j \tag{5.38}$$

with non-negative coefficients W_j. Any possible $\boldsymbol{S}_{Lab}$ with vanishing circular polarization component can be written in the form of equation 5.38. Let $\varphi_{det,i}$ be the center of the bin i in the φ_{det}-spectrum. Then equation 5.25 for the counts in the simulated spectra reads

$$I'_j(\varphi_{det,i}) = \boldsymbol{V}^T(\varphi_{det,i}) \cdot \boldsymbol{S}_j. \tag{5.39}$$

Combining equations 5.38 and 5.39 gives

$$I'(\varphi_{det,i}) = \sum_{j=1}^{4} W_j I'_j(\varphi_{det,i}), \tag{5.40}$$

which defines the fit function for the experimental φ_{det}-spectrum. When the normalization of the fit function to the total experimental counts in the φ_{det}-spectrum is enforced, the number of fit parameters is reduced to 3. With the values W_j obtained from the fit, the Stokes vector of interest $\boldsymbol{S}_{Lab}$ is calculated according to equation 5.38. This method gives in principle not only the relative Stokes parameters $P_{1,Lab}$ and $P_{2,Lab}$, but also the absolute intensity of the photon beam incident

on the polarimeter $S_{0,Lab}$. The latter relies on a correct modeling of the absolute detector efficiency $\eta(\theta_{det}, \varphi_{det})$ by the simulation. Such a correct modeling is not assumed here, but it is expected, that the relative detector efficiency is sufficiently well described. The constant factor that relates it to the absolute efficiency does not influence $P_{1,Lab}$ and $P_{2,Lab}$. The spectra $I'_j(\varphi_{det})$ are obtained from the simulated Δn_x-Δn_y-spectra applying the same randomization procedure as for the experimental spectrum (see section 5.3.1). For a photon energy of 175 keV, the simulated Δn_x-Δn_y-spectra are shown in figure 5.10. In figure 5.11 an example of an exper-

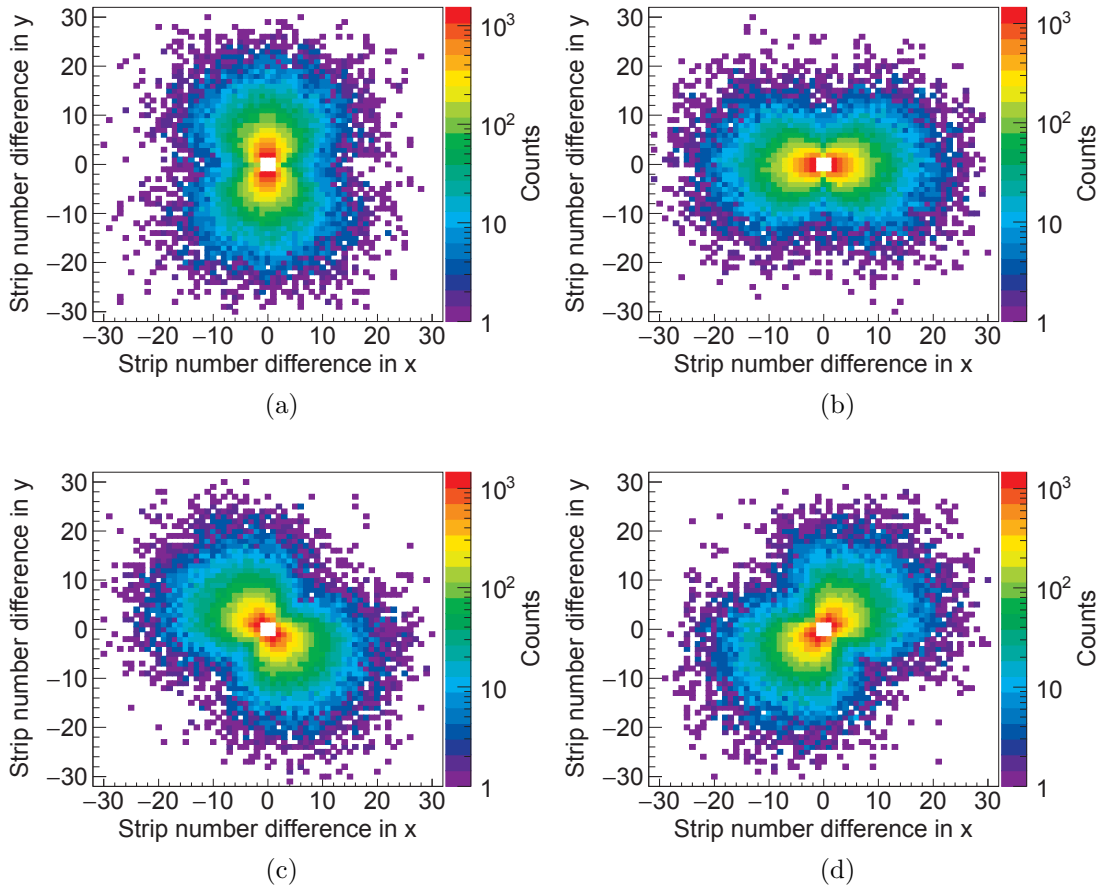

Figure 5.10: Simulated Δn_x-Δn_y-spectra for 100 % polarized 175-keV photons. The polarization orientation is (a) 0°, (b) 90°, (c) 45° and (d) 135° with respect to the horizontal plane.

imental Δn_x-Δn_y-spectrum (at $\theta_{tar} = 65°$) and the corresponding fit of the φ_{det}-spectrum are given. Alternative approaches for the polarization determination, that were discussed during this thesis, but not yet implemented, are found in appendix B.

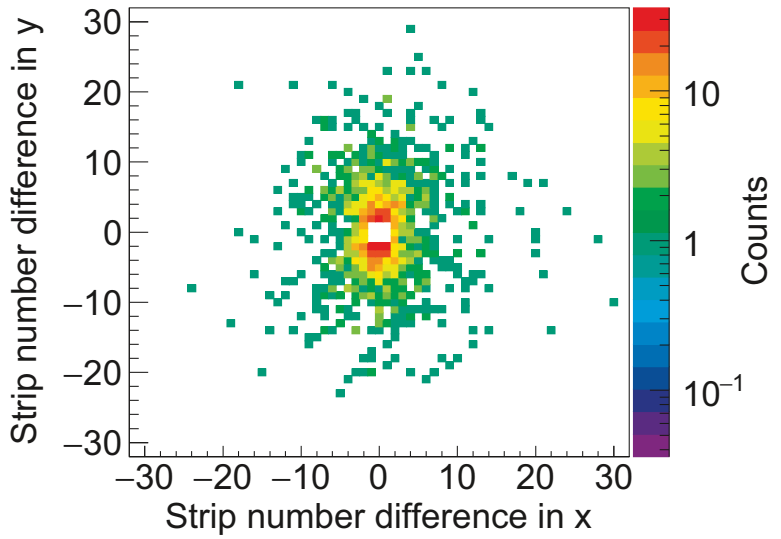

(a)

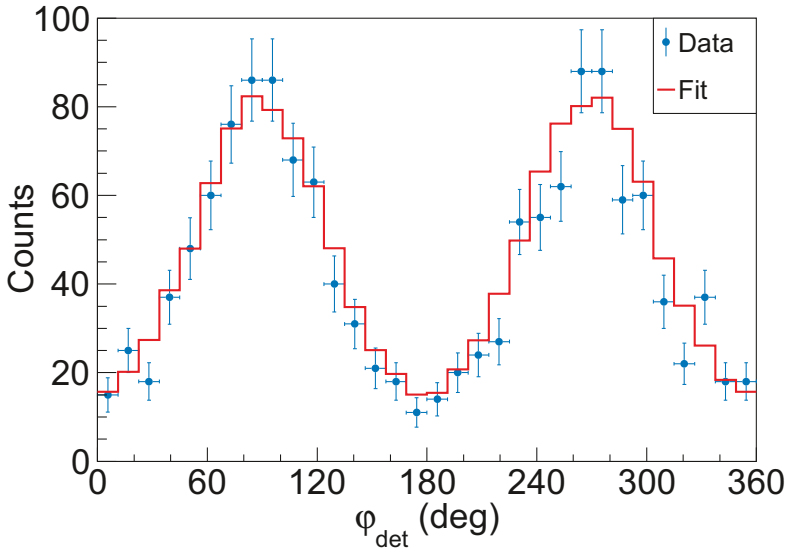

(b)

Figure 5.11: Experimental data of Rayleigh photons scattered at $\theta_{tar} = 65°$. (a) Δn_x-Δn_y-spectrum. (b) φ_{det}-spectrum with Monte Carlo fit function.

5.3.4 Bootstrap procedure

The bootstap method [170] is used to resample Δn_x-Δn_y-spectra. These resampled spectra are then used as input for the described procedures to determine $\boldsymbol{P}_{Lab}$. Repeating this resampling process many times leads to a $\boldsymbol{P}_{Lab}$-distribution whose width (component-wise) is used as an estimate for the statistical error. This section gives an overview of the implementation. Starting point are six distributions

$I'_0(\Delta n_x, \Delta n_y)$ which are labeled as follows:

- $I'_{exp,0}(\Delta n_x, \Delta n_y)$: experimentally measured distribution at the energy of interest.
- $I'_{bg,0}(\Delta n_x, \Delta n_y)$: background distribution, either measured or assumed to be uniform in φ_{det}, see section 5.3.2.
- $I'_{sim1,0}(\Delta n_x, \Delta n_y), \ldots, I'_{sim4,0}(\Delta n_x, \Delta n_y)$: Monte Carlo simulated distributions.

In addition, one needs the mean numbers of events $N_{exp,0}$ (for the experimental spectrum) and $N_{bg,0}$ (for the background spectrum). While $N_{exp,0}$ is simply given by the number of events in $I'_{exp,0}(\Delta n_x, \Delta n_y)$, the background strength $N_{bg,0}$ is estimated from the data according to the methods described in section 5.3.2. With these quantities available, a single resampling iteration consists of the following steps:

1. Randomize the number of events for the experimental and the background spectrum: $N_{exp} \sim \text{Poisson}(N_{exp,0})$ and $N_{bg} \sim \text{Poisson}(N_{bg,0})$.
2. Create $I'_{exp}(\Delta n_x, \Delta n_y)$, a resampled experimental (total) spectrum. The number of sampled events is N_{exp}.
3. Create $I'_{bg}(\Delta n_x, \Delta n_y)$, a resampled background spectrum. The number of sampled events is N_{bg}.
4. Create $I'_{sim1}(\Delta n_x, \Delta n_y), \ldots, I'_{sim4}(\Delta n_x, \Delta n_y)$, resampled simulated spectra. Here, the number of sampled events is not random, instead the number of events in the corresponding original spectrum $I_{sim,j,0}$ is used.
5. Convert the six resampled spectra into φ_{det}-spectra using the randomization procedure described in section 5.3.1.
6. Subtract the background φ_{det}-spectrum from the experimental one.
7. Fit the background-corrected φ_{det}-spectrum with a linear combination of the simulated φ_{det}-spectra, as described in section 5.3.3.
8. Store the values of $P_{1,Lab}$ and $P_{2,Lab}$.

In this thesis, the number of resampling iterations is set to 100000. An example for resulting distributions of $P_{1,Lab}$ and $P_{2,Lab}$ is shown in figure 5.12. From the stored

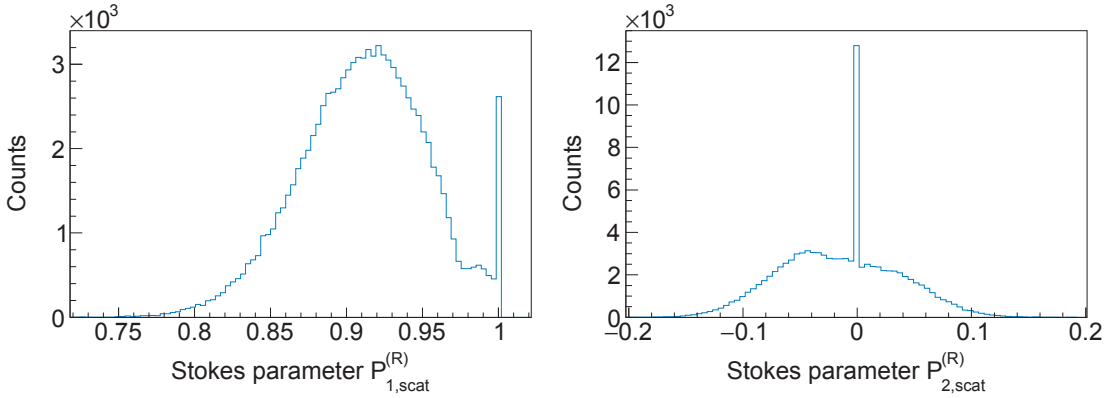

(a) (b)

Figure 5.12: Distributions resulting from the bootstrap resampling procedure for Rayleigh-scattered photons at $\theta_{tar} = 120°$. (a) $P^{(R)}_{1,scat}$. (b) $P^{(R)}_{2,scat}$.

values of $P_{1,Lab}$ and $P_{2,Lab}$ means and RMS[1] values are computed to get the final results and their (statistical) error estimates, respectively. As one can see in figure 5.12, there is a single bin with strangely large content at 1 (for $P_{1,Lab}$) and 0 (for $P_{2,Lab}$). It is believed, that this is an artifact that results from the range restriction of the fit parameters, that does not allow values of $P_{1,Lab}$ larger than 1. If the fit routine finds the optimum value for one or more fit parameters outside the respective ranges, the parameter is set to the limit value, which results in a value for $P_{1,Lab}$ that falls in the bin around 1. The restriction $P^2_{1,Lab} + P^2_{2,Lab} \leq 1$ then forces the value for $P_{2,Lab}$ to fall in the bin around 0. It is found, that here this artifact has a negligible effect on the determination of mean and RMS.

5.4 Scattering analysis

This section explains how calculations regarding scattering in the gold target are performed. The relation between the Stokes vectors of the incident and the scattered photon beams is given by equation 3.21 applied to the proper angles:

$$\boldsymbol{S}_{scat}(\theta_{tar}, \varphi_{tar}) = T(\theta_{tar}) \cdot M(\varphi_{tar}) \cdot \boldsymbol{S}_{inc}. \tag{5.41}$$

Both Compton- and Rayleigh scattering are considered, therefore both $T = T_C,\ T_R$ are used. In this thesis, only the relative Stokes vectors $\boldsymbol{P}_{scat}$ and $\boldsymbol{P}_{inc}$ are of interest,

[1]Root Mean Square

they can be related to each other by modifying equation 5.41 to

$$\boldsymbol{P}_{scat}(\theta_{tar}, \varphi_{tar}) = \frac{T(\theta_{tar}) \cdot M(\varphi_{tar}) \cdot \boldsymbol{P}_{inc}}{(1,0,0,0) \cdot T(\theta_{tar}) \cdot M(\varphi_{tar}) \cdot \boldsymbol{P}_{inc}}. \tag{5.42}$$

Equations 5.41 and 5.42 are used to calculate the Stokes vector of the scattered photon beam from the one of the incident photon beam, assuming a point-like detector. Section 5.4.1 derives the modifications that are required to describe a measurement with an extended detector. A non-uniform detection probability (over the detector surface) is taken into account in section 5.4.2. In section 5.4.3, the inversion of equations 5.41 and 5.42 is discussed, which allows the reconstruction of polarization of the incident beam from the measured one. Error estimations are presented in section 5.4.4.

5.4.1 Detector size effects

The size of the detector is taken into account by integrating equation 5.41 over the detector surface. The following calculations correspond to the square polarimeter, modifications of the procedure for the round germanium detector are shown afterwards. The center of the detector is assumed to be at the angles $(\theta_{tar}, \varphi_{tar})$. Around this, angles (θ', φ') corresponding to points on the detector surface can be ordered for the integration as follows:

$$\theta' \in [\theta_{min}, \theta_{max}]\,, \qquad \varphi' \in [\varphi_{tar} - \delta\varphi(\theta'),\ \varphi_{tar} + \delta\varphi(\theta')]\,. \tag{5.43}$$

With this, the integration of equation 5.41 reads

$$\begin{aligned}\boldsymbol{S}^{(ext)}_{scat}(\theta_{tar}, \varphi_{tar}) &= \int_{\theta_{min}}^{\theta_{max}} \mathrm{d}\theta'\ \sin(\theta') \cdot T(\theta') \int_{\varphi_{tar}-\delta\varphi(\theta')}^{\varphi_{tar}+\delta\varphi(\theta')} \mathrm{d}\varphi'\ M(\varphi') \cdot \boldsymbol{S}_{inc} \\ &= \int_{\theta_{min}}^{\theta_{max}} \mathrm{d}\theta'\ \sin(\theta') \cdot T(\theta') \int_{-\delta\varphi(\theta')}^{\delta\varphi(\theta')} \mathrm{d}\tilde{\varphi}\ M(\tilde{\varphi}) \cdot M(\varphi_{tar}) \cdot \boldsymbol{S}_{inc}.\end{aligned} \tag{5.44}$$

The superscript (ext) denotes an extended detector and the dependence of the Stokes vector on θ_{tar} for this case is contained in θ_{min} and θ_{max}. In the second line of equation 5.44 the variable substitution $\tilde{\varphi} = \varphi' - \varphi_{tar}$ (corresponds to a shift of the detector to $\varphi_{tar} = 0$) is applied and the property of the rotation matrix $M(\tilde{\varphi}+\varphi_{tar}) = M(\tilde{\varphi}) \cdot M(\varphi_{tar})$ is exploited. With this, an expression analogous to equation 5.41

can be obtained:

$$\boldsymbol{S}_{scat}^{(ext)}(\theta_{tar}, \varphi_{tar}) = T^{(ext)}(\theta_{tar}) \cdot M(\varphi_{tar}) \cdot \boldsymbol{S}_{inc}. \tag{5.45}$$

The transfer matrix for the extended detector $T^{(ext)}$ is given by

$$T^{(ext)}(\theta_{tar}) = \int_{\theta_{min}}^{\theta_{max}} \mathrm{d}\theta' \ \sin(\theta') \cdot T(\theta') \int_{-\delta\varphi(\theta')}^{\delta\varphi(\theta')} \mathrm{d}\tilde{\varphi} \ M(\tilde{\varphi}). \tag{5.46}$$

Figure 5.13 illustrates the approach for the evaluation of $T^{(ext)}$. The incident pho-

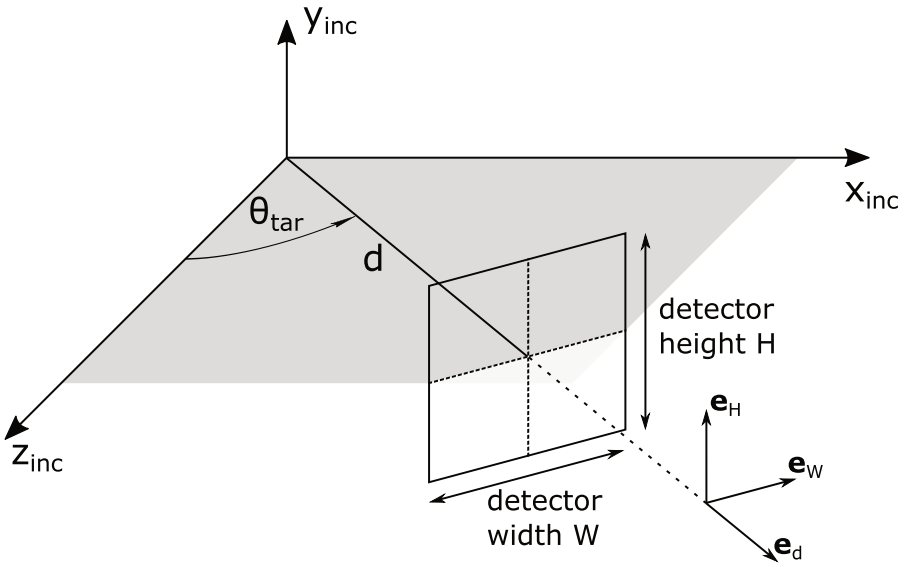

Figure 5.13: Detector geometry used for the integration in equation 5.46.

ton beam propagates along the z_{inc}-direction and the detector with height H and width W is positioned in the horizontal plane at a distance d from the scattering target. Unit vectors $\boldsymbol{e}_d$, $\boldsymbol{e}_W$ and $\boldsymbol{e}_H$ correspond to the direction of the connection target-detector center, and the horizontal and vertical axis of the detector surface, respectively. They are given by

$$\boldsymbol{e}_d = \begin{pmatrix} \sin(\theta_{tar}) \\ 0 \\ \cos(\theta_{tar}) \end{pmatrix}, \qquad \boldsymbol{e}_W = \begin{pmatrix} \cos(\theta_{tar}) \\ 0 \\ -\sin(\theta_{tar}) \end{pmatrix}, \qquad \boldsymbol{e}_H = \begin{pmatrix} 0 \\ 1 \\ 0 \end{pmatrix}. \tag{5.47}$$

With these vectors, a point $\boldsymbol{r}$ on the detector surface is parametrized as follows:

$$\boldsymbol{r} = d \cdot \boldsymbol{e}_d + w \cdot \boldsymbol{e}_W + h \cdot \boldsymbol{e}_H \tag{5.48}$$

with $w \in \left[-\frac{W}{2}, \frac{W}{2}\right]$ and $h \in \left[-\frac{H}{2}, \frac{H}{2}\right]$. Using the integration variables θ' and $\tilde{\varphi}$, $\boldsymbol{r}$ is expressed as

$$\boldsymbol{r} = L \cdot \begin{pmatrix} \sin(\theta')\cos(\tilde{\varphi}) \\ \sin(\theta')\sin(\tilde{\varphi}) \\ \cos(\theta') \end{pmatrix}. \tag{5.49}$$

With the reduced parameters $\hat{w} = \frac{w}{d}$, $\hat{h} = \frac{h}{d}$ and $\hat{L} = \frac{L}{d}$, the combination of equations 5.48 and 5.49 yields

$$\hat{L} \cdot \begin{pmatrix} \sin(\theta')\cos(\tilde{\varphi}) \\ \sin(\theta')\sin(\tilde{\varphi}) \\ \cos(\theta') \end{pmatrix} = \boldsymbol{e}_d + \hat{w} \cdot \boldsymbol{e}_W + \hat{h} \cdot \boldsymbol{e}_H. \tag{5.50}$$

Equation 5.50 immediately gives $\hat{L} = \sqrt{1 + \hat{w}^2 + \hat{h}^2}$ and with this the relation between the variable sets $(\theta', \tilde{\varphi})$ and $(\hat{w}, \hat{h})$. Calculation the Jacobi determinant leads to the following result:

$$\sin(\theta')\ \mathrm{d}\theta'\ \mathrm{d}\tilde{\varphi} = \hat{L}^{-3}\ \mathrm{d}\hat{w}\ \mathrm{d}\hat{h}. \tag{5.51}$$

With this change of variables, equation 5.46 becomes

$$T^{(ext)}(\theta_{tar}) = \int_{-\frac{W}{2d}}^{\frac{W}{2d}} \mathrm{d}\hat{w} \int_{-\frac{H}{2d}}^{\frac{H}{2d}} \mathrm{d}\hat{h}\ \hat{L}^{-3} \cdot T(\theta'(\hat{w}, \hat{h})) \cdot M(\tilde{\varphi}(\hat{w}, \hat{h})). \tag{5.52}$$

In order to evaluate the (in general not analytically available) components of T, θ' must be expressed in terms of $\hat{w}$ and $\hat{h}$. The last component of equation 5.50 yields

$$\theta' = \arccos\left[\frac{\cos(\theta_{tar}) - \hat{w} \cdot \sin(\theta_{tar})}{\hat{L}}\right], \tag{5.53}$$

implying that θ' (and with this also T) is an even function of $\hat{h}$. For the evaluation of $\tilde{\varphi}(\hat{w}, \hat{h})$, one notes that M only contains the $\tilde{\varphi}$-dependent terms $\cos(2\tilde{\varphi})$ and $\sin(2\tilde{\varphi})$. It can be shown, that they are even and odd functions of $\hat{h}$, respectively. Therefore all components of $T \cdot M$ proportional to $\sin(2\tilde{\varphi})$ vanish when integrated and all the others are even functions of $\hat{h}$. This results in the following transfer matrix for an

extended detector (only upper left 3×3 part of T considered):

$$T^{(ext)}(\theta_{tar}) = \int_{-\frac{W}{2d}}^{\frac{W}{2d}} \mathrm{d}\hat{w} \int_{-\frac{H}{2d}}^{\frac{H}{2d}} \mathrm{d}\hat{h}\ \hat{L}^{-3} \cdot \begin{pmatrix} T_{00} & T_{01}\cos(2\tilde{\varphi}) & 0 \\ T_{10} & T_{11}\cos(2\tilde{\varphi}) & 0 \\ 0 & 0 & T_{22}\cos(2\tilde{\varphi}) \end{pmatrix}. \quad (5.54)$$

This matrix has almost the same structure as the corresponding matrices for a point-like detector (equation 3.23 for Compton- and equation 3.24 for Rayleigh scattering). Only the symmetry $T_{10} = T_{01}$ is not retained. The integral in equation 5.54 is evaluated numerically using a 1000×1000-points grid in $(\hat{w}, \hat{h})$. In order to compare results from calculations with a point-like and an extended detector, $T^{(ext)}$ is divided by the solid angle

$$\Delta\Omega = \int_{-\frac{W}{2d}}^{\frac{W}{2d}} \mathrm{d}\hat{w} \int_{-\frac{H}{2d}}^{\frac{H}{2d}} \mathrm{d}\hat{h}\ \hat{L}^{-3} \quad (5.55)$$

that is covered by the detector. This normalization is only necessary when the absolute differential cross section is considered, as $\Delta\Omega$ cancels in any calculation of the Stokes parameters P_1 and P_2.

In order to adapt the described integration procedure to a round detector, the following modification is applied: as before, one integrates a rectangular detector, now with $W = H = D$, where D is the diameter of the round detector. For each grid point $(\hat{w}, \hat{h})$, one checks if it corresponds to a position on the (round) surface and if not, the point is skipped.

5.4.2 Position-dependent detection probability

In the integration described in section 5.4.1, one implicitly assumes that the probability to record an event is equal for all the positions on the detector surface. This is in general not true and it would therefore be desirable to include a more accurate estimation of the weights, with which the different regions of the detector surface contribute. For the polarimeter, this can readily be done by counting the events that are registered in the individual strips. This option is not available for the non-segemented germanium detector, but since it is significantly smaller than the polarimeter, it is found that there is only a negligible difference in the results, when $T^{(ext)}$ is used instead of T. Using the correct weights is therefore not crucial for the germanium detector. For the polarimeter, the weighting function is represented by a two-dimensional position distribution over the detector surface, one example

is figure 4.6a. Depending on the application, the position distribution of different types of energy depositions is used:

- Polarization of Compton-scattered photons: the weighting function is given by the position distribution of recoil electrons of those events that are used to analyze the polarization of the Compton-scattered photons.
- Polarization of Rayleigh scattered photons: again recoil electrons, but from events that are used to analyze the polarization of the Rayleigh-scattered photons.
- Differential Rayleigh scattering cross section: use the position distribution of single hits.

Choosing different position distributions takes into account the fact, that different types of events may have different detection probability distributions. The weighting function is incorporated by writing it as a function of the integration variables in equation 5.54. This term is then added as a factor $u(\hat{w}, \hat{h})$ to the integrand:

$$T^{(ext,w)}(\theta_{tar}) = \int_{-\frac{W}{2d}}^{\frac{W}{2d}} \mathrm{d}\hat{w} \int_{-\frac{H}{2d}}^{\frac{H}{2d}} \mathrm{d}\hat{h}\ \hat{L}^{-3} \cdot u(\hat{w}, \hat{h}) \cdot \begin{pmatrix} T_{00} & T_{01}\cos(2\tilde{\varphi}) & 0 \\ T_{10} & T_{11}\cos(2\tilde{\varphi}) & 0 \\ 0 & 0 & T_{22}\cos(2\tilde{\varphi}) \end{pmatrix}. \tag{5.56}$$

The superscript (ext, w) refers to an extended detector where a weighting function is included. The proper normalization is achieved, when the same weighting function is included in the calculation of the solid angle:

$$\Delta\Omega^{(w)} = \int_{-\frac{W}{2d}}^{\frac{W}{2d}} \mathrm{d}\hat{w} \int_{-\frac{H}{2d}}^{\frac{H}{2d}} \mathrm{d}\hat{h}\ \hat{L}^{-3} \cdot u(\hat{w}, \hat{h}). \tag{5.57}$$

One should note that any weighting function $u(\hat{w}, \hat{h})$ that is not even in $\hat{h}$ will cause that some of the zeroes in $T^{(ext,w)}$ have to be replaced by finite values. In the present thesis, this has been neglected because (i) the integrands in these terms are proportional to $\sin(2\tilde{\varphi})$ in a small $\tilde{\varphi}$-interval around zero and (ii) no pronounced asymmetry in the used weighting functions is observed, i.e. they are "almost" even in $\hat{h}$.

5.4.3 Reconstruction of the incident beam polarization

This section considers the scenario where a certain polarization of the scattered beam $\boldsymbol{P}_{scat}(\theta_{tar}, \varphi_{tar})$ is measured and from this, the polarization of the incident beam $\boldsymbol{P}_{inc}$ shall be determined. Starting point is the inversion of equation 5.41:

$$\boldsymbol{S}_{inc} = M^{-1}(\varphi_{tar}) \cdot T^{-1}(\theta_{tar}) \cdot \boldsymbol{S}_{scat}(\theta_{tar}, \varphi_{tar}). \tag{5.58}$$

As shown in section 5.4.1, detector size effects can be taken into account by simply replacing T by $T^{(ext)}$ or $T^{(ext,w)}$. Being a rotation matrix, M is always invertible with $M^{-1} = M^T$. For the invertability of T (and its integrated versions), only the upper left 3×3 part is considered. Any transfer matrix discussed in the present thesis is singular when its entry T_{22} vanishes. For T_C, this happens at $\theta_{tar} = 90°$. For all detector-target distances considered here, this singular point shifts to about 90.1° in $T_C^{(ext)}$. Additional singular points appear at $\theta_{tar} = 0°$ and 180°, but these are not relevant, as the detector would overlap with the primary beam there. The weighted transfer matrix $T_C^{(ext,w)}$ is singular at $\theta_{tar} \approx 90.16°$. The influence of this singularity will be further discussed in section 6.2.
At 175 keV, T_R is not invertible only at $\theta_{tar} \approx 84.2°$. For the different calculated versions of $T_R^{(ext)}$ and $T_R^{(ext,w)}$ this singular position shifts by not more than about ±1.3°. It is therefore sufficiently far away from all the angles that were covered in the experiment, so that $T_R^{(ext,w)}$ is invertible without problems at those positions. As for $T_C^{(ext)}$, $T_R^{(ext)}$ (and also $T_R^{(ext,w)}$) has additional singular points in regions where the detector would overlap with the primary beam.
If the transfer matrix is invertible, the expression for the relative Stokes vector of the incident beam is derived from equation 5.58 as

$$\boldsymbol{P}_{inc} = \frac{M^T(\varphi_{tar}) \cdot T^{-1}(\theta_{tar}) \cdot \boldsymbol{P}_{scat}(\theta_{tar}, \varphi_{tar})}{(1,0,0,0) \cdot M^T(\varphi_{tar}) \cdot T^{-1}(\theta_{tar}) \cdot \boldsymbol{P}_{scat}(\theta_{tar}, \varphi_{tar})}. \tag{5.59}$$

In this expression, the components in the fourth row and column of T^{-1} are set to zero.

5.4.4 Error estimation

This section discusses how the errors of $\left(\frac{\mathrm{d}\sigma}{\mathrm{d}\Omega}\right)_R$ (using equation 5.7), $\boldsymbol{P}_{scat}$ (using equation 5.42) and $\boldsymbol{P}_{inc}$ (using equation 5.59) are estimated. Uncertainties are taken into account of the scattering angles θ_{tar} and φ_{tar}, the target-detector distance d,

the weighting function u and the input Stokes parameters $P_{1,in}$ and $P_{2,in}$ (these are either $P_{i,inc}$ or $P_{i,scat}$, depending on what is calculated). Let y denote the respective output quantity and x_i the input quantities. The error of the i^{th} input parameter is Δx_i and its contribution to the error of y is labeled Δ_i. For the scattering angles and the input Stokes parameters, Δ_i is estimated by variation of x_i while the other parameters are kept constant:

$$\Delta_i = \max\left\{|y(x_i + \Delta x_i) - y(x_i)|,\ |y(x_i) - y(x_i - \Delta x_i)|\right\}. \tag{5.60}$$

The same procedure would be computationally expensive for the target-detector distance, as its variation requires a new integration according to equation 5.56. Therefore a simplifying approach is chosen:

$$\Delta_d = \frac{\partial y}{\partial d} \cdot \Delta d \qquad (\approx y(d + \Delta d) - y(d)). \tag{5.61}$$

The evaluation of $\frac{\partial y}{\partial d}$ involves derivatives with respect to d of the transfer matrix entries. These derivatives also require additional integrations, but when they occur on the level of transfer matrix entries, they can be decoupled from the evaluation of y. With this, the integration can be performed in a first (slow) step of the overall analysis and its result can be stored. The evaluation of y happens in a (fast) second step, which can be repeated easily if debugging is required.
The most challenging error estimation is the one associated with u as this is not a simple parameter, but a function. In principle, it is possible to estimate a statistical error induced by the measured u by resampling it within a bootstrap procedure. But this would require a new integration in each bootstrap iteration which is too expensive. Here, the deviation of y between two extreme cases of u – namely a point-like detector and one with uniform u – is used for a rough error estimation:

$$\Delta_u = \left[y(\text{uniform } u) - y(\text{point-like detector})\right]/2. \tag{5.62}$$

The overall error Δy is calculated from the individual contributions Δ_i as

$$\Delta y = \sqrt{\sum_i \Delta_i^2}. \tag{5.63}$$

6 Results and discussion

In this chapter, the results of the experiment are presented. The polarization of the Compton-scattered photons is considered in section 6.1. From this, the polarization of the incident beam is reconstructed (section 6.2). The Rayleigh scattering differential cross section and polarization of the Rayleigh-scattered photons are shown in section 6.3. The theoretical predictions for both quantities rely on the incident beam polarization. If the Rayleigh scattering theory is applied "inversely", the incident beam polarization can be reconstructed from the measured Rayleigh polarization. Results for this are given in section 6.4 and compared with the incident beam polarization reconstructed from the Compton polarization.

6.1 Linear polarization for Compton scattering

In order to determine the polarization of the Compton-scattered photons, double hits in the polarimeter are restricted to events where the energy of the photon scattered in the gold target is in an interval around the peak of the Compton profile (see figure 5.3). The peak position (and therefore the energy window) varies with θ_{tar} according to equation 2.4. Here, peak positions are at 147 keV ($\theta_{tar} = 65°$), 131 keV ($\theta_{tar} = 90°$) and 116 keV ($\theta_{tar} = 120°$). Almost all steps described in section 5.3 must be performed individually for each of these energies. Only the noise levels of the polarimeter strips (figure 5.5) can be reused for all energies. A difference regarding the analysis has already been pointed out in section 5.1.2: at $\theta_{tar} = 120°$, the scattered photon energy of 116 keV is too low for the coincidence condition to be applicable. This problem does not arise for 131 keV and 147 keV, so there the coincidence condition is applied. No inconsistencies due to this different treatment of the different data sets are found. Statistics are relatively good (compared to Rayleigh, see section 6.3), with an energy window of ±3 keV one has at least about 3000 events in the φ_{det}-spectrum. Therefore an error estimation beyond the purely statistical error is performed. For this, variations of the results (Stokes parameters $P^{(C)}_{1,scat}$ and $P^{(C)}_{2,scat}$) due to different energy windows are investigated. The chosen energy windows are ±1, ±2, ±3, ±4 and ±5 keV. Each energy window leads to a result x_i with statistical error Δx_i ($i = 1, \ldots, 5$ and $x = P^{(C)}_{1,scat}, P^{(C)}_{2,scat}$). The final

value x is then calculated as the weighted mean

$$x = \left[\sum_i \frac{x_i}{\Delta x_i}\right] \cdot \left[\sum_i \frac{1}{\Delta x_i}\right]^{-1} . \tag{6.1}$$

If the x_i were independent, the error of the weighted mean would be given by

$$\Delta x = \left[\sum_i 1\right]^{\frac{1}{2}} \cdot \left[\sum_i \frac{1}{\Delta x_i}\right]^{-1} . \tag{6.2}$$

Here – where the x_i cannot assumed to be independent – a more conservative error estimation is applied:

$$\Delta x = \max_i\{\max\{\Delta x_i,\ |x_i - x|\}\}. \tag{6.3}$$

The results for $P^{(C)}_{1,scat}$ and $P^{(C)}_{2,scat}$ are shown in figure 6.1. The largest uncertainty

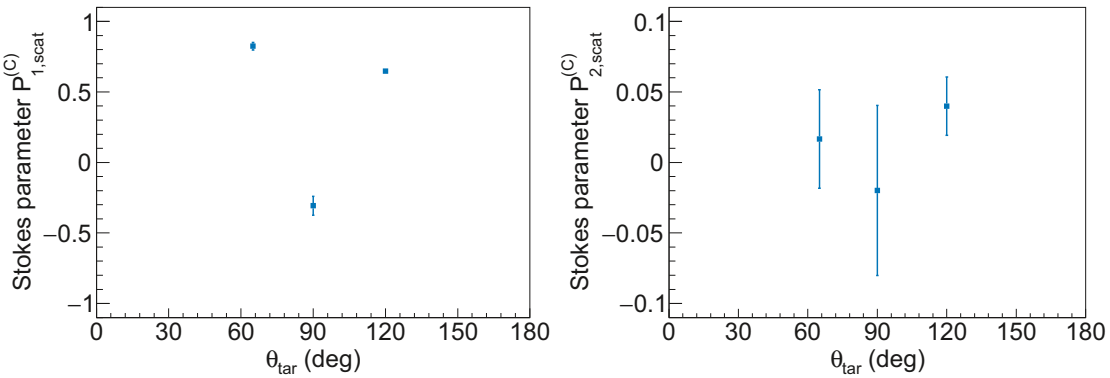

(a) (b)

Figure 6.1: Stokes parameters of the photons Compton-scattered in the gold target. (a) $P^{(C)}_{1,scat}$. (b) $P^{(C)}_{2,scat}$. Data points are weighted means of individual values obtained from different energy windows around the peak of the Compton profile.

occurs at $\theta_{tar} = 90°$. The first reason for that is, that the statistics are lowest for that measurement. Second, for $P^{(C)}_{1,scat}$, one has the additional difficulty of measuring a small (absolute) value. Then the uncertainty generally (for Compton polarimetry) tends to increase.

6.2 Linear polarization of incident beam from Compton

In this section, results for the reconstructed Stokes parameters of the incident beam $P_{1,inc}$ and $P_{2,inc}$ are presented. To obtain them, equation 5.59 with $T = T_C^{(ext,w)}$ and $\boldsymbol{P}_{scat} = \boldsymbol{P}_{scat}^{(C)}$ is applied. As the target-detector distance varies between runs (see table 4.1), $T_C^{(ext,w)}$ is calculated for each angle individually. The values for $\boldsymbol{P}_{scat}^{(C)}$ are the ones from figure 6.1. For the data point at $\theta_{tar} = 90°$, this procedure is problematic due to the close singularity of the transfer matrix at $\theta_{tar} \approx 90.16°$ (see section 5.4.3). As the singularity is within the uncertainty of θ_{tar}, the incident Stokes vector could be reconstructed, but would be meaningless due to the large errors. Therefore the reconstruction of $\boldsymbol{P}_{inc}$ is only performed at $\theta_{tar} = 65°$ and 120°. The results are shown in figure 6.2. Here it is assumed that the polarization of

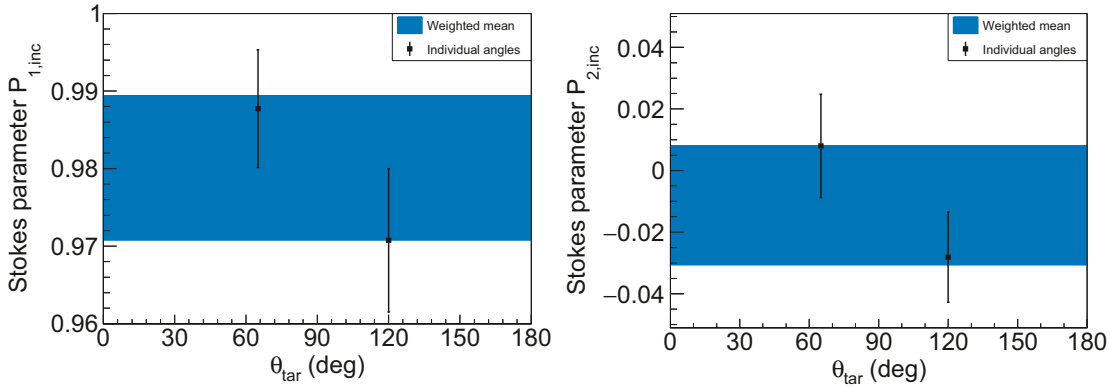

(a) (b)

Figure 6.2: Stokes parameters of the incident beam reconstructed from $\boldsymbol{P}_{scat}^{(C)}$. (a) $P_{1,inc}$. (b) $P_{2,inc}$. Data points for individual angles are shown together with their weighted mean.

the incident beam is constant over the time of the experiment. Therefore the results from the different scattering angles are combined by calculating again their weighted mean according to equation 6.1. The error of the weighted mean is estimated with the maximum deviation between an individual data point and the weighted mean. Table 6.1 summarizes the results. The value for $P_{2,inc}$ agrees with zero. This – together with $P_{1,inc}$ close to +1 – confirms the initial assumption that the incident beam is highly linearly polarized in the horizontal plane, so that the experiment was carried out in coplanar scattering geometry.

Table 6.1: Stokes parameters of the incident beam reconstructed from the polarization of the Compton-scattered photons. Given are weighted means over the scattering angles $\theta_{tar} = 65°$ and 120°.

Quantity	Value	Error
$P_{1,inc}$	0.9801	0.0093
$P_{2,inc}$	-0.011	0.019

6.3 Results for Rayleigh scattering

In this section, results for the experimentally observed quantities, that are related to Rayleigh scattering, are presented. These are the differential cross section and the Stokes parameters $P_{1,scat}^{(R)}$ and $P_{2,scat}^{(R)}$. It is found that $P_{2,scat}^{(R)}$ agrees with zero at all angles covered by the polarimeter. Due to the proportionality $P_{2,scat}^{(R)} \propto P_{2,inc}$, this is consistent with the result for $P_{2,inc}$ that also agrees with zero (see table 6.1). More detailed conclusions cannot be drawn from the results for $P_{2,scat}^{(R)}$, therefore the following discussion is restricted to $P_{1,scat}^{(R)}$ and $\left(\frac{d\sigma}{d\Omega}\right)_R$. The measured values of these quantities are shown in figure 6.3. The errors of $\left(\frac{d\sigma}{d\Omega}\right)_R$ reflect the uncertainties of the line strength ratio due to statistics and fit variations according to equation 5.23. For all data points in figure 6.3a, they are smaller than the point size on the given scale and smaller than the systematic error of 8 %. The statistics of the polarization measurement are relatively poor in the present experiment and are therefore expected to give the dominant contribution to the uncertainty of $P_{1,scat}^{(R)}$. Other error sources are not considered. This scheme has been applied for the same polarimeter, for example, in [40] where statistics were higher.

The theoretical predictions in figure 6.3 assume a point-like detector and use the Stokes parameters of the incident beam from table 6.1. While this procedure already gives a good overall agreement with the experimental data, it does not take into account the finite detector size and the uncertainty of the Stokes parameters of the incident beam. A detailed study of these effects is given in figure 6.4.

From figure 6.3, one sees that both $\left(\frac{d\sigma}{d\Omega}\right)_R$ and $P_{1,scat}^{(R)}$ show a pronounced dip at scattering angles around $\theta_{tar} = 90°$. For the cross section, this polarization effect can qualitatively be understood in the classical picture of Thomson scattering: the incident photon, described as a plane electromagnetic wave, induces an oscillation of a target electron parallel to the polarization direction of the wave. This oscillation is the acceleration of a charge, which leads to the emission of another electromagnetic wave. The emission pattern of the secondary (scattered) wave has dipole character

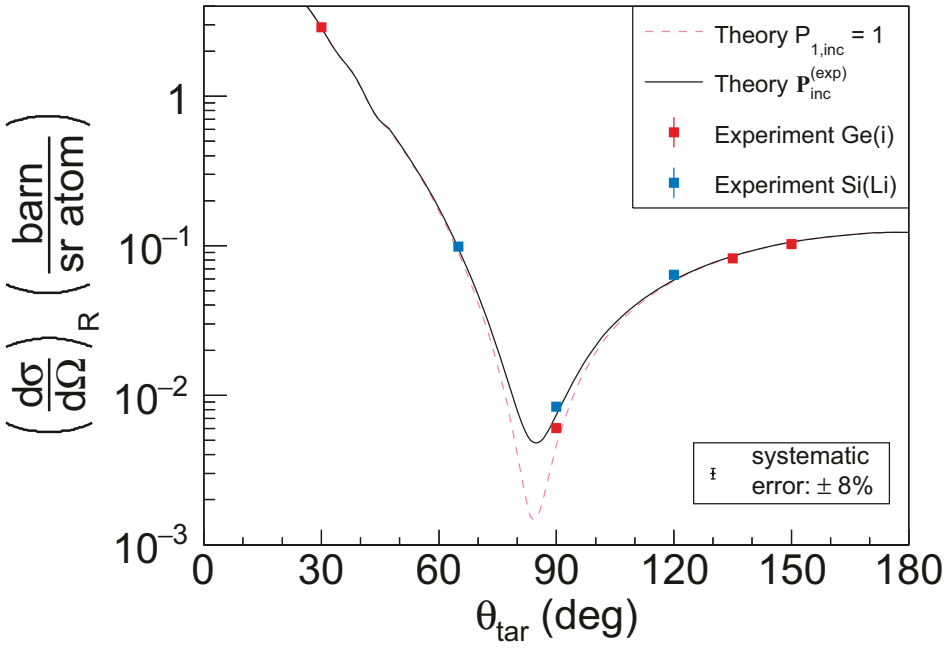

(a)

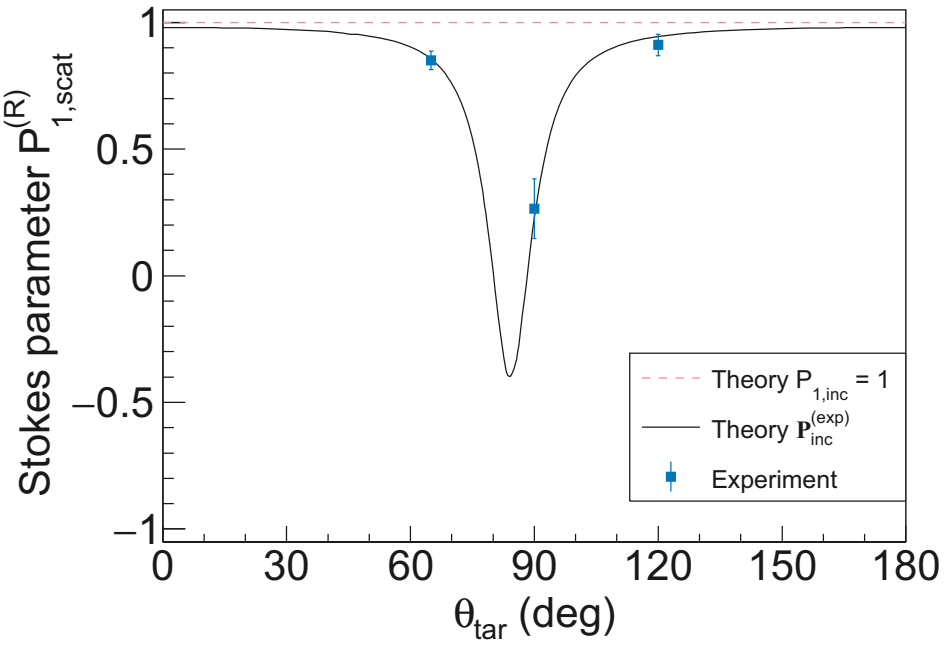

(b)

Figure 6.3: Experimental results for Rayleigh scattering. (a) Differential cross section. (b) Stokes parameter $P^{(R)}_{1,scat}$. The shown theory is for a point-like detector and with the Stokes parameters of the incident beam from table 6.1 (denoted $\boldsymbol{P}^{(exp)}_{inc}$). For comparison, also the predictions for a completely polarized incident beam are shown.

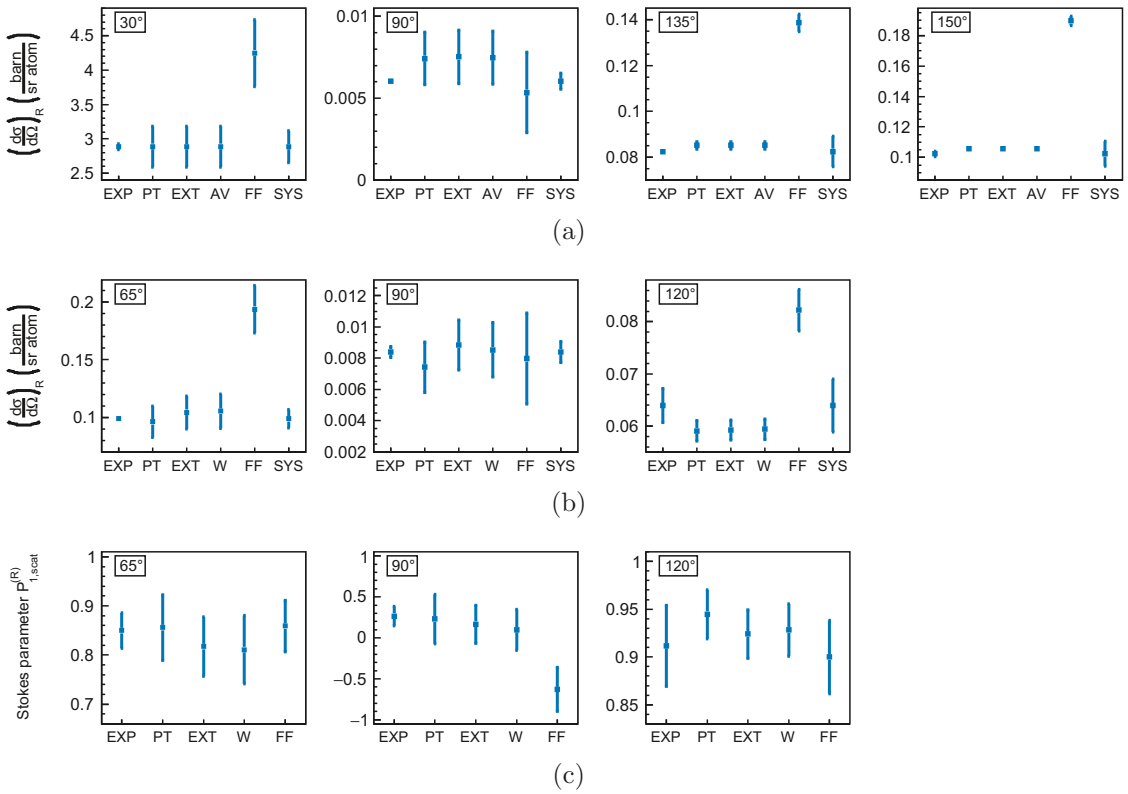

Figure 6.4: Comparison of experimental data with different theories. (a) Differential cross section measured with germanium detector. (b) Differential cross section measured with polarimeter. (c) $P_{1,scat}^{(R)}$. Abbreviations are: EXP: experimental data with statistical error. PT: theory with transfer matrix T_R (point-like detector). EXT: theory with $T_R^{(ext)}$ (extended detector). AV: mean of PT and EXT. W: theory with $T_R^{(ext,w)}$ (extended detector with weighting function). FF: form factor theory. SYS: experimental data with systematic error. The most elaborate predictions are W for the polarimeter and AV for the germanium detector. These are also assumed for FF.

and in particular, emission is forbidden in the direction of the oscillation, i.e. at $\theta_{tar} = 90°$ in the polarization plane of the incident photon. Therefore a vanishing differential cross section is predicted at $\theta_{tar} = 90°$ in an "ideal" setup ($\varphi_{tar} = 0°$, $P_{1,inc} = 1$) for Thomson scattering and any form factor theory. Assuming such an ideal setup allows to understand the existence of a cross section dip around $\theta_{tar} = 90°$, but not the finite value at that angle and especially not two non-agreeing values from the different detectors. Furthermore, an explanation of the measured $P_{1,scat}^{(R)}$ is completely impossible at $\theta_{tar} = 90°$ due to the (predicted) vanishing cross section. Within the same ideal setup, but at other angles than 90°, one obtains

the prediction $P^{(R)}_{1,scat} = 1$, a value that clearly disagrees with all experimental data points. From the considerations up to now, it is clear that a simple form factor theory in combination with an ideal setup is not sufficient to describe the measured data. A more refined description is achieved with the following modifications:

1. Apply fully relativistic S-matrix calculations instead of the form factor theory.
2. Use measured incident beam polarization for predictions.
3. Take into account the finite detector size.

When (2) and (3) are applied, partial agreement with the experiment is achieved (figure 6.4, see entries "FF"). Surprisingly, the cross section predicted by the form factor theory agrees at $\theta_{tar} = 90°$ with the experiment and not at all the other angles. For $P^{(R)}_{1,scat}$, the situation is vice versa. This result can be explained as follows: the cross section is proportional to the total scattered intensity I' which consists of photons polarized parallel and perpendicular to the scattering plane: $I' = I'_{\parallel} + I'_{\perp}$. At $\theta_{tar} = 90°$, the form factor theory clearly underestimates $I'_{\parallel} \propto |A_{\parallel}|^2 = 0$ (strictly only for point-like detector) and therefore an agreement with the experimental cross section can only be achieved, when $I'_{\perp}$ is overestimated, so that the deviations cancel. On the other hand, one has $P^{(R)}_{1,scat} \propto I'_{\parallel} - I'_{\perp}$. The same deviations in $I'_{\parallel}$ and $I'_{\perp}$ that cancel in the cross section, add up here. For angles sufficiently far away from 90°, $\cos^2(\theta_{tar})$ is large enough, so that both $I'_{\parallel}$, $I'_{\perp} \propto |f|^2$ are overestimated. Then deviations add up in the cross section and cancel in $P^{(R)}_{1,scat}$.
Applying (1) with or without (2): these cases are shown in figure 6.3. For $P^{(R)}_{1,scat}$, the prediction with $P_{1,inc} = 1$ fails for all angles. When the value from table 6.1 $P_{1,inc} = 0.98$ is used instead, the data are described well. This result shows that $P^{(R)}_{1,scat}$ is highly sensitive to $P_{1,inc}$, especially for scattering angles around 90°. This sensitivity leads to substantial uncertainties in the predictions for $P^{(R)}_{1,scat}$ at $\theta_{tar} = 90°$ and also 65°, see figure 6.4c. For these angles, the uncertainty of the prediction exceeds the one of the experiment. The same is not true at $\theta_{tar} = 120°$, which indicates a lower sensitivity to the incident beam polarization at that angle. As $P^{(R)}_{1,scat}$, also the cross section is very sensitive to $P_{1,inc}$ near $\theta_{tar} = 90°$, which can be seen by comparing the theory curves in figure 6.3a. The assumption $P_{1,inc} = 1$ is sufficient to describe the data at all angles, except at $\theta_{tar} = 90°$. There, a finite cross section is predicted by the S-matrix theory, but the value is not in agreement with either one of the two experimental data points. When $P_{1,inc} = 0.98$ is used,

the cross section prediction at $\theta_{tar} = 90°$ increases by about a factor of two. The uncertainty of the prediction is shown in figure 6.4. At $\theta_{tar} = 90°$, this uncertainty is large enough to achieve an agreement between the theory and both experimental data points. The uncertainty is also larger than the experimental one, the same is true for $\theta_{tar} = 30°$ and 65°. For these smaller angles, the large uncertainty of the prediction cannot be attributed to the uncertainty of $P_{1,inc}$ as the cross section is hardly sensitive to it there. Instead, the uncertainty in the scattering angle θ_{tar} is the main error source, which can be seen in figure 6.3a from the strong variation – even on a logarithmic scale.

The most elaborate predictions are achieved when all refinements (1), (2) and (3) are included. As discussed, the combination of only S-matrix theory and proper incident beam polarization leads to an agreement with all experimental data points. Now the finite detector size is additionally taken into account. As can be seen from figure 6.4a, this does not change the predictions for the germanium detector on the given scales (see entries "EXT", "AV", compare with "PT"). For the polarimeter (figures 6.4b and 6.4c), some variations are visible, but they are all within the respective uncertainties of the predictions. A general trend, which model for the detector size ("PT", "EXT" or "W") provides the best prediction, cannot be observed.

In order to gain some physical insights, it is instructive to investigate the effects from the individual atomic shells on the scattering process. In figure 6.5, the differential cross section is shown, when only part of the shells are included in the calculation. If only the K-shell is taken into account, the data for backward angles can already be described quite well. With inclusion of higher shells, the cross section hardly changes in that angular regime. The amplitudes for scattering from higher shells are small there, which is consistent with the qualitative picture obtained from the form factor approximation (see section 2.1.3): at large momentum transfers (large scattering angles) only inner-shell electrons contribute to the scattering amplitude. Another feature, that one sees when only the K-shell is included, is the shift of the cross section minimum from 90° to smaller angles. It was previously identified, that this shift is due to higher, non-dipole contributions (in the multipole expansion of equation 2.18) [171]. For scattering angles of 120° and smaller, it is mandatory to include at least the L-shell (in addition to the K-shell) to describe the experimental data. Not only increases this inclusion the cross section drastically (more than one order of magnitude in forward direction), it also introduces an additional shift of the cross section minimum to smaller angles. This shift due to the scattering of

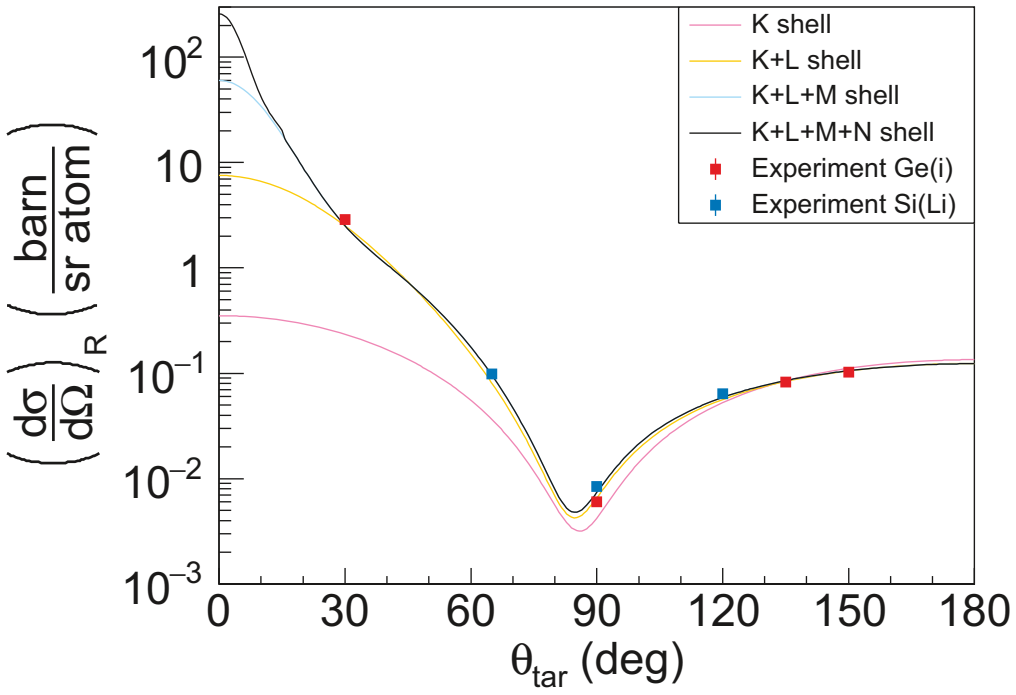

Figure 6.5: Predictions for the differential Rayleigh scattering cross section when the amplitudes from different shells are included. Values from table 6.1 are used for the incident Stokes parameters and a point-like detector is assumed.

weakly-bound outer-shell electrons was previously identified in [79].

It should be noted, that predictions in figure 6.5 were also provided by [106], but with a different screening potential than in the calculations that appeared up to now (before: Kohn-Sham, here: frozen Dirac-Fock). The only significant change introduced by this variation of the screening potential is a decrease of the cross section at $\theta_{tar} = 30°$ by about 10 %. This is still within the estimated overall accuracy of the theory, which is 5 to 10 % according to [106]. A deviation of that order can be considered good agreement in the present context [106].

In conclusion, the S-matrix theory is confirmed by the experiment, as it describes both the differential cross section and the linear polarization of the scattered photons correctly for all scattering angles. Including the detector size in the theoretical model has a negligible effect for the small germanium detector and leads to variations that are within the uncertainty of the prediction for the polarimeter. The form factor theory fails for all angles. Spurious agreement in either the cross section or the linear polarization was identified through a pronounced disagreement in the respective

other quantity. This finding stresses the importance of a simultaneous measurement of these observables for a stringent test of a certain theory. The approximation that the incident beam is 100 % polarized is not adequate to describe the measured polarization of the scattered photons at all angles. At $\theta_{tar} = 90°$, the disagreement is most pronounced and also present for the differential cross section. As the incident beam is found to be only slightly depolarized ($P_{1,inc} = 0.98$), one deduces a strong sensitivity of both $\left(\frac{\mathrm{d}\sigma}{\mathrm{d}\Omega}\right)_R$ and $P_{1,scat}^{(R)}$ to the polarization of the incident beam – especially near $\theta_{tar} = 90°$. This sensitivity causes that the uncertainty of $P_{1,inc}$ limits the precision in that angular region in the present experiment.

6.4 Linear polarization of incident beam from Rayleigh

As seen in section 6.3, $P_{1,scat}^{(R)}$ is highly sensitive to $P_{1,inc}$ near $\theta_{tar} = 90°$. Such a sensitivity can be exploited to precisely determine the polarization of the incident beam. As in section 6.2, this is done using equation 5.59, but now with $T_R^{(ext,w)}$ and $\boldsymbol{P}_{scat} = \boldsymbol{P}_{scat}^{(R)}$. In contrast to Compton scattering, now also the data point at $\theta_{tar} = 90°$ can be used, because $T_R^{(ext,w)}$ has no close-lying singularity. Due to the high sensitivity there, this is the most interesting point for the reconstruction of the polarization of the incident beam. The weighted mean over the data points of all angles and its uncertainty is determined as in section 6.2. Results are shown in figure 6.6. For both $P_{1,inc}$ and $P_{2,inc}$, the values for the different scattering angles agree well with each other also with the previously determined values from $\boldsymbol{P}_{scat}^{(C)}$ in table 6.1. At $\theta_{tar} = 120°$, the uncertainty of $P_{1,inc}$ is considerably higher than at the other two angles. This effect can be explained with the angle-dependent sensitivity of $P_{1,scat}^{(R)}$ to $P_{1,inc}$. The relatively low sensitivity at $\theta_{tar} = 120°$ results in a large uncertainty of the reconstructed $P_{1,inc}$. With a higher sensitivity at $\theta_{tar} = 65°$, the uncertainty decreases. Even though the sensitivity is even higher at $\theta_{tar} = 90°$, no further decrease of the uncertainty is observed. This is due to the higher uncertainty of the input value $P_{1,scat}^{(R)}$ at that angle (see figure 6.3b).
In order to further illustrate the sensitivity to the polarization of the incident beam, the theoretical predictions for $P_{1,scat}^{(R)}$ are plotted as a function of $P_{1,inc}$ for various scattering angles and the ideal case of a point-like detector in figure 6.7. In such a representation, a high sensitivity is found in regions with a steep derivative, which is the case near $P_{1,inc} = 1$. This is true for both Rayleigh (figure 6.7a) and Compton

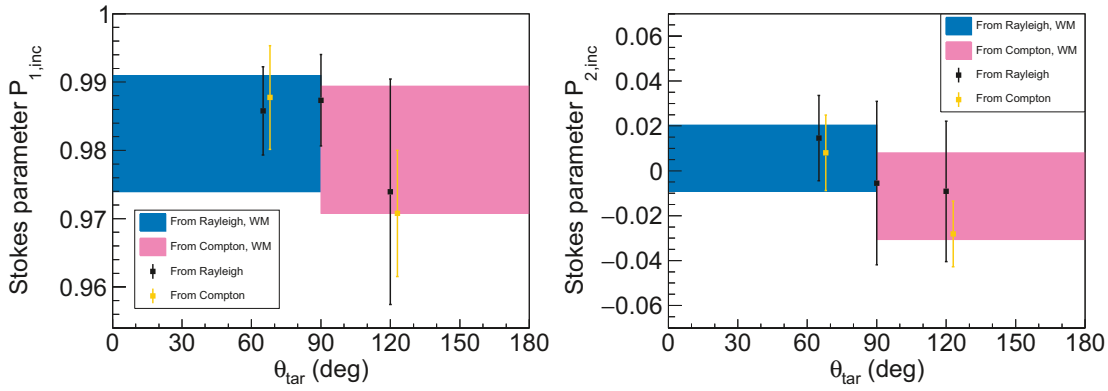

(a) (b)

Figure 6.6: Stokes parameters of the incident beam reconstructed from $\boldsymbol{P}_{scat}^{(R)}$. (a) $P_{1,inc}$. (b) $P_{2,inc}$. For comparison, the values for the incident beam polarization reconstructed from $\boldsymbol{P}_{scat}^{(C)}$ are also shown (drawn with a shift of +3°). Weighted means over all angles are labeled WM.

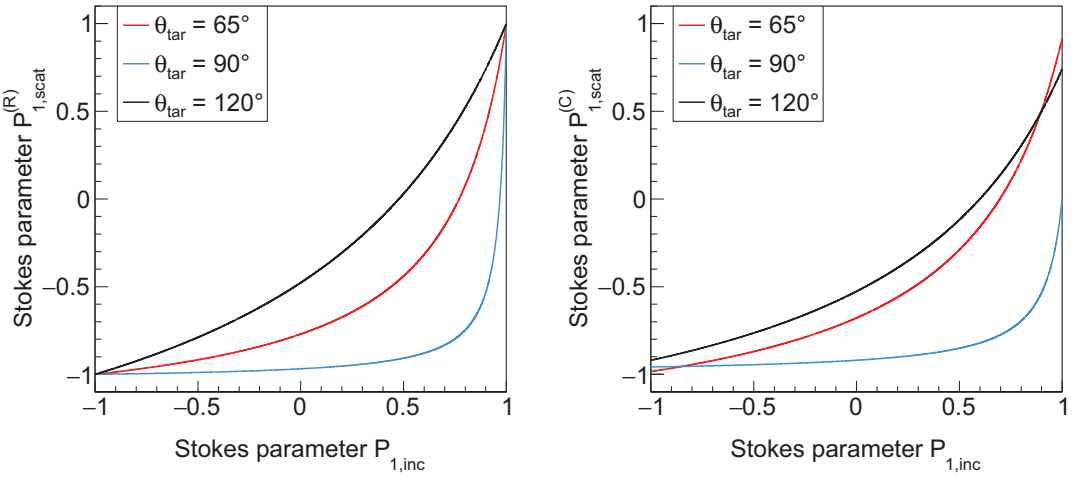

(a) (b)

Figure 6.7: Stokes parameter $P_{1,scat}$ as a function of $P_{1,inc}$ for fixed scattering angles in the case of (a) Rayleigh and (b) Compton scattering. The detector is point-like.

scattering (figure 6.7b). A comparison of the two processes indicates that $P_{1,scat}^{(R)}$ attains higher values than $P_{1,scat}^{(C)}$ at $P_{1,inc} = 1$ and also steeper derivatives in its vicinity. This would make Rayleigh scattering the more sensitive process of the two and for diagnostics, it has the additional advantage, that the higher values of $P_{1,scat}^{(R)}$ can be measured with better precision.

More details require a zoom to the sensitive region, which is given in figure 6.8. That also allows to see effects of the detector size. At the scattering angles $\theta_{tar} = 65°$

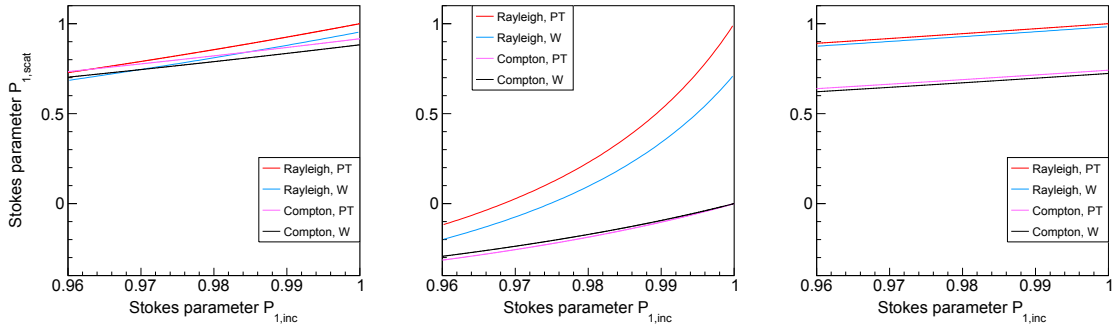

(a) (b) (c)

Figure 6.8: Stokes parameter $P_{1,scat}$ as a function of $P_{1,inc}$ at (a) $\theta_{tar} = 65°$, (b) $\theta_{tar} = 90°$ and (c) $\theta_{tar} = 120°$. Calculations for a point-like (PT) and an extended detector with weighting function (W) are compared.

and 120° and for incident beam polarizations between 0.96 and 1, the effect of the detector size is on the order of 5 % and less for both Compton and Rayleigh scattering. The sensitivity of the two processes is comparable at these angles and essentially not varying as a function of $P_{1,inc}$. At $\theta_{tar} = 120°$ though, the value of $P_{1,scat}$ is substantially higher for Rayleigh- than for Compton scattering. This last feature is also observed at $\theta_{tar} = 90°$ – there additionally with a significant difference between the Rayleigh scattering prediction for a point-like and an extended detector (figure 6.8b). The effect of the detector size for Compton scattering at $\theta_{tar} = 90°$ is on the same order as for the other angles. The most interesting aspect at $\theta_{tar} = 90°$ is the sensitivity: it is (i) not constant as a function of $P_{1,inc}$, (ii) significantly lower for Compton scattering and (iii) clearly reduced for Rayleigh scattering at the highest values for $P_{1,inc}$ when an extended detector is assumed instead of a point-like one.

7 Summary

In the present thesis, the elastic scattering of highly linearly polarized hard x-rays was investigated experimentally. A linear polarization transfer from the incident to the scattered photons was observed, which is highly sensitive to the polarization of the incident beam.

The experiment was conducted at the High Energy Materials Science beamline P07 at the synchrotron radiation source PETRA III, where an intense beam of 175-keV photons was provided. Selecting this energy permitted to study Rayleigh scattering – the elastic scattering from bound electrons – as the other elastic scattering contributions such as Delbrück- and nuclear scattering are negligible then. Furthermore, combining that energy with a high-Z scattering target (gold) allowed the identification of relativistic effects in the Rayleigh process. The target was constructed as a thin foil (~ 1 μm) which was mounted in a dedicated vacuum chamber. With this setup, both multiple scattering in the target and scattering in air were kept to a minimum. Solid state detectors were employed to measure the scattered radiation. These detectors were placed at different scattering angles in the horizontal plane, which corresponds to the polarization plane of the incident PETRA III beam, so that a coplanar scattering geometry was considered. The angle-differential cross section for Rayleigh scattering was measured with an HPGe detector, whereas the linear polarization of the Rayleigh-scattered photons was detected with a dedicated Si(Li) strip Compton polarimeter for hard x-rays. This was – to the author's knowledge – the first (linear) polarization-resolved elastic scattering experiment in the hard x-ray regime with a highly linearly polarized incident beam. It only became feasible through the use of state-of-the-art technologies, namely a third-generation synchrotron radiation source in combination with a highly-efficient x-ray polarimeter, as these components ensure sufficient statistics in the recorded data. For the determination of the differential cross section, a relative measurement was performed. The intensity of the Rayleigh-scattered photons was normalized to the intensity of the isotropic $K\alpha_1$ fluorescence radiation from the gold target. In such a scheme, effects from the geometry of the setup as well as from possible variations in the incident beam intensity cancel. A theoretical value for the $K\alpha_1$ cross section and a ratio of (relative) detector efficiencies has to be provided to obtain an absolute differential cross section. It was found that the systematic error of 8 %, which was

introduced by this normalization, was larger than the uncertainty from statistics and fitting procedure at all angles.
Since the polarimeter allows an energy-resolved measurement, the linear polarizations of Rayleigh- and Compton-scattered photons (in the target) were measured simultaneously. In order to extract the linear polarization from the data of the strip detector, a refined algorithm for the treatment of detector effects (compared to previous experiments with such detectors) was applied. Using the additivity of the Stokes parameters for incoherent beams, the polarimeter response was modeled as a linear combination of four Monte Carlo simulated responses. The bootstrap resampling method was employed to estimate statistical errors of the measured polarizations. With that scheme, no further assumptions about the correlation between P_1 and P_2 are required for error estimation.
Here, the polarization of the Compton-scattered photons was treated as an "auxiliary" quantity which was required to obtain an independent estimation for the linear polarization of the incident beam using the transfer matrix formalism. This was necessary to provide meaningful theoretical predictions for the differential cross section and the polarization of the Rayleigh-scattered photons, as both quantities strongly depend on the polarization of the incident beam. In particular at a scattering angle of 90°, it was found that the approximation of a completely linearly polarized incident beam was not sufficient to describe the experimental results (differential cross section and Rayleigh polarization). For the Rayleigh polarization, a value of $P_{1,scat}^{(R)} = 1$ is predicted, but at 90° a value of $P_{1,scat}^{(R)} = 0.26$ was measured. The large discrepancy was resolved with a prediction based on the obtained estimation of $P_{1,inc} \approx 0.98$ for the polarization of the incident beam. It could therefore be observed that this small deviation from a 100 % polarized incident beam modifies substantially the differential cross section and the Rayleigh polarization, indicating a strong polarization sensitivity of the Rayleigh process. Additionally, this sensitivity, together with the uncertainty of the incident beam polarization, leads to uncertainties in the predictions at 90° that exceed the experimental errors (both differential cross section and Rayleigh polarization). The experimental results and theoretical predictions – both with their respective uncertainties – are summarized in figure 7.1. Agreement is achieved at all data points.
Furthermore, results were compared to the predictions of the form factor theory which does not entirely take into account relativistic effects arising from a strong electron binding and a high photon energy. The form factor theory fails to describe

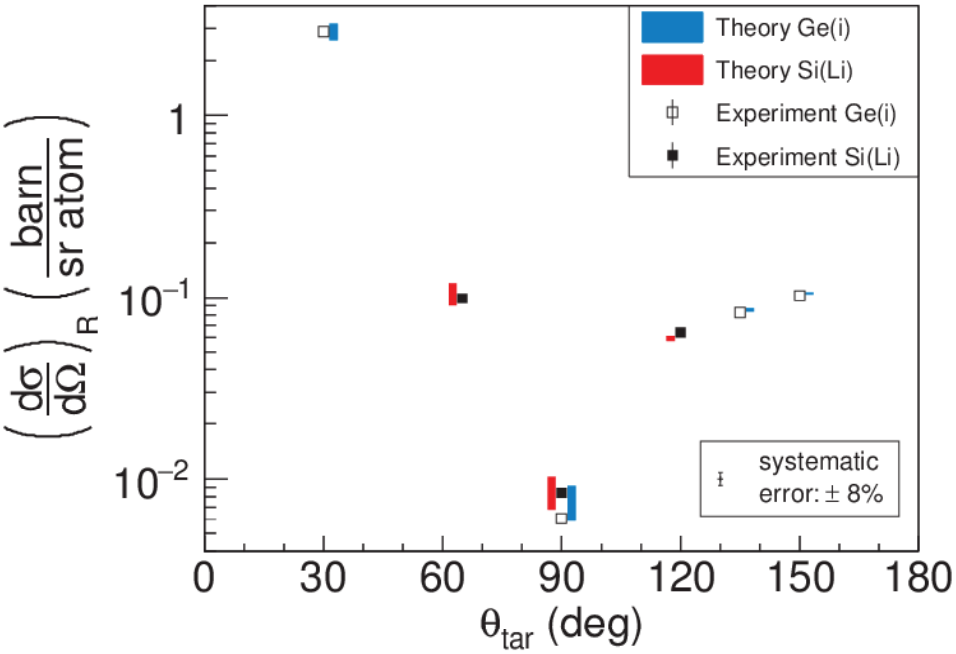

(a)

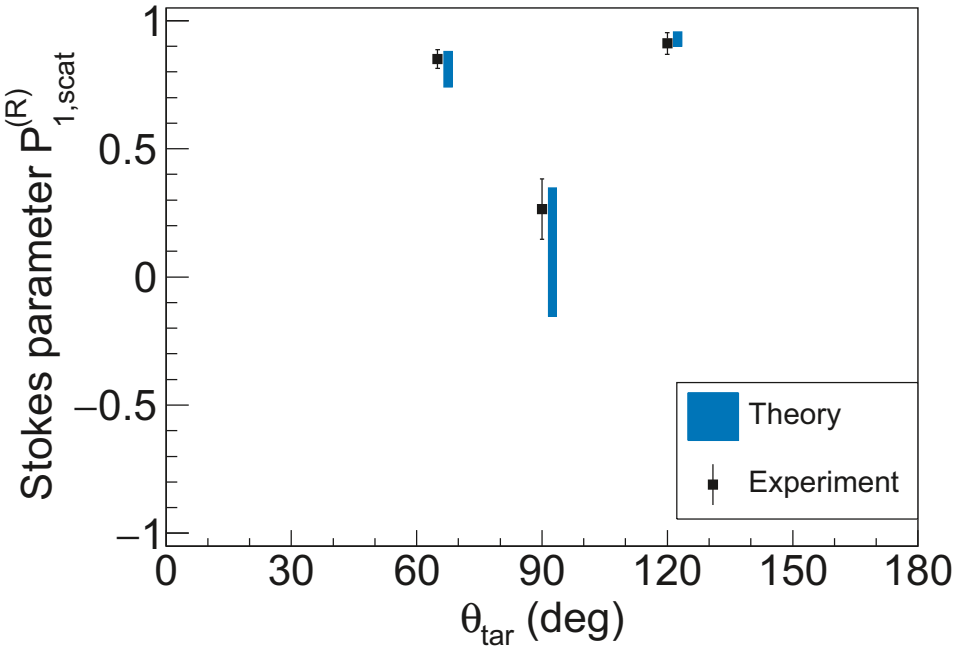

(b)

Figure 7.1: Results of this thesis. (a) Differential Rayleigh scattering cross section. (b) Stokes parameter P_1 of the Rayleigh-scattered photons. The uncertainties of the predictions arise from uncertainties in the polarization of the incident beam and the experimental geometry.

the experimental data at all angles that were considered, therefore confirming that relativistic effects play in important role in the present scenario. The combined measurement of differential cross section and linear polarization was crucial to identify spurious agreement of the form factor theory with the experiment, which resulted from cancellations of errors.

The strong sensitivity to the polarization of the incident beam – in particular of $P_{1,scat}^{(R)}$ – can be exploited to diagnose the former. For this scheme, the same transfer matrix formalism as for Compton scattering was applied and a more accurate result was obtained from the measured polarization of the Rayleigh-scattered photons than from the polarization of the Compton-scattered photons. It still has to be verified how the sensitivity of the two scattering processes differs as a function of photon energy and target material. In principle, the proposed polarization diagnostics scheme (passive scatterer combined with a polarization measurement of the scattered radiation) works for Rayleigh- and Compton scattering and both can even be measured simultaneously (as in this experiment) if an energy-dispersive polarimeter is used.

A strong sensitivity of the scattering process (both Rayleigh and Compton) to the polarization of the incident beam translates also into a strong sensitivity to the azimuthal scattering angle. Therefore, effects of the detector covering a certain angular interval were investigated. It was found that for the geometry of the present experiment, results based on a point-like and an extended detector, respectively, only differed within the experimental uncertainties.

8 Outlook

In the present thesis linear polarization effects in elastic photon-atom scattering were investigated at 175 keV – a regime where Rayleigh scattering is the dominant elastic process. A logical step would now be to extend such polarization studies to different energies to probe other effects of the elastic photon-matter interaction. At photon energies in the region around 1 MeV, Delbrück scattering starts to become important and can be accessed in polarization experiments. The γ-ray regime introduces challenges both for the photon source and the detector (polarimeter). Nowadays highly polarized γ-rays can be produced via laser Compton (back-) scattering and this has already been applied in several experiments, see for example [172] and references therein. The Si(Li) polarimeter employed in the present experiment is not expected to be efficient enough at γ-ray energies. A possible solution could be to use a germanium strip detector instead. Such devices are available in our group and were already characterized [173, 174] and applied as Compton polarimeters [36, 39], but only for hard x-rays. Furthermore – as they were originally not designed as Compton polarimeters – their pixels are non-square and small (1.165×0.25 mm^2). The small pixels drastically increase charge sharing, especially at high energies. A dedicated germanium polarimeter with larger, square pixels would therefore be desirable, following for example the design used in [175].

Another interesting scenario to investigate is elastic scattering near the K-shell ionization threshold of high-Z targets. In this energy region, electron correlations in the target become important which leads to a failure of the independent particle approximation. The theoretical treatment is therefore quite challenging and experimental data are strongly required. As the energies for such an experiment are below the 175 keV used in the present scenario, intense beams of polarized photons are readily available at synchrotron radiation facilities. Using also the quasi-monochromaticity and tunability of such sources, a scan over the ionization threshold is feasible. For a polarization measurement of the scattered photons, the same Si(Li) polarimeter as in the present experiment can in principle be employed. But the lower energies limit the applicability of the time coincidence condition, as has been observed here at 116 keV (sections 5.1.2 and 6.1). This is due to the fact that the electronic noise level requires a relatively large CFD threshold. If the energy is below $\approx$ 70 keV, a polarization measurement is not possible at all as the Compton recoil electron

energies are on the same order as the noise. An extension of Compton polarimetry with strip detectors to lower energies is currently realized with the construction of a new Si(Li) strip detector (having the same spatial dimensions as the one used in the present experiment) that operates with cryogenic preamplifiers. For this device, a reduction of the electronic noise by 50 % or more is expected. This will not only allow polarization measurements a lower energies, but also the resolution of close-lying lines.

In the present thesis, the polarization transfer in Rayleigh scattering has been identified as a potential diagnostic scheme for the linear polarization of intense, highly linearly polarized hard x-ray beams which are available, for example, at synchrotron radiation facilities. Such a method promises to cover a broad energy range (some 100s keV), therefore complementing the highly polarization-sensitive channel-cut crystals which are currently limited to energies below 20 keV [130]. Furthermore, one has a lot of flexibility to optimize the diagnostics setup according to the photon energy and also intensity: scattering angles θ_{tar} and φ_{tar}, target material and thickness, polarimeter type, size and distance from the target. Further studies are required to determine the energy range (and also the range of the polarization to be diagnosed) where the method is feasible and how the mentioned parameters can be optimized for a certain scenario.

The current GSI and future FAIR facility are specialized on ion- and antiproton- rather than on photon beams. In particular, spin-polarized ion beams will be available and used in several planned experiments of the SPARC collaboration, for example concerning parity violation [176, 177]. It is then of utmost importance to experimentally control (diagnose) the spin-polarization of the ion beam. A scheme that has been proposed for this task is to cross the beam with a gas jet target (low-Z) and measure the linear polarization of the emitted K-REC photons [72]. The Stokes parameter P_2 is then directly proportional to the degree of spin-polarization of the beam of highly charged projectiles.

Finally, two important examples for planned experiments at FAIR with unpolarized ion beams that include hard x-ray polarization measurements shall be mentioned. The first one investigates K-REC into an initially bare heavy ion. Such an experiment was performed for a uranium beam with kinetic energies 98 MeV/u [34, 36] and 400 MeV/u [34]. At FAIR, a beam energy of 800 MeV/u will be available – a regime, for which the so-called cross-over effect is predicted [178]: a sign change of the Stokes parameter P_1 for emission angles below 90°. An experimental ver-

ification is still pending. The second example is Coulomb excitation of a heavy (projectile) ion in collisions with a gas target. This process was already studied for a hydrogen-like uranium projectile [179], enabling precise tests of atomic structure theories. In [179], Lyman x-rays emitted by excited U^{91+} ions were detected in anticoincidence [180] with down-charged U^{90+} ions. From the angular distribution of the Lyα_1/Lyα_2 intensity ratio one can determine the alignment parameter $\mathcal{A}_2$ that describes the non-statistical population of the magnetic substates (for excitation to $2p_{\frac{3}{2}}$). At FAIR, such an experiment is planned to be conducted with a higher beam energy – a scenario, for which a larger value of $\mathcal{A}_2$ is predicted [181].

Bibliography

[1] P. C. Johns. "Coherent scatter in diagnostic radiology". *Medical Physics* **10** 40 (1983). DOI: 10.1118/1.595443. (Cit. on p. 4).

[2] R. Cesareo et al. "Interaction of keV photons with matter and new applications". *Physics Reports* **213** 117–178 (1992). DOI: 10.1016/0370-1573(92)90086-F. (Cit. on p. 4).

[3] M. S. Westmore. "Angular-dependent coherent scatter measured with a diagnostic x-ray image intensifier-based imaging system". *Medical Physics* **23** 723 (1996). DOI: 10.1118/1.597720. (Cit. on p. 4).

[4] G. Harding and B. Schreiber. "Coherent X-ray scatter imaging and its applications in biomedical science and industry". *Radiation Physics and Chemistry* **56** 229–245 (1999). DOI: 10.1016/S0969-806X(99)00283-2. (Cit. on p. 4).

[5] G. Goerigk et al. "Anomalous small-angle X-ray scattering in materials science". *Journal of Applied Crystallography* **36** 425–429 (2003). DOI: 10.1107/S0021889803000542. (Cit. on p. 4).

[6] J. Karle. "Macromolecular Structure from Anomalous Dispersion". *Physics Today* **42** 22 (1989). DOI: 10.1063/1.881170. (Cit. on p. 4).

[7] M. Y. Sfeir. "Probing Electronic Transitions in Individual Carbon Nanotubes by Rayleigh Scattering". *Science* **306** 1540–1543 (2004). DOI: 10.1126/science.1103294. (Cit. on p. 4).

[8] R. Luggar and W. Gilboy. "Recent developments in industrial applications of elastic scatter X-ray inspection". *Radiation Physics and Chemistry* **56** 213–227 (1999). DOI: 10.1016/S0969-806X(99)00278-9. (Cit. on p. 4).

[9] M. Born and E. Wolf. *Principles of optics: electromagnetic theory of propagation, interference and diffraction of light*. 6th ed. Oxford ; New York: Pergamon Press, 1980. ISBN: 978-0-08-026481-3 978-0-08-026482-0. URL: http://www.sciencedirect.com/science/book/9780080264820 (cit. on p. 4).

[10] S. C. Roy, R. H. Pratt, and L. Kissel. "Rayleigh scattering by energetic photons: Development of theory and current status". *Radiation Physics and Chemistry* **41** 725–738 (1993). DOI: 10.1016/0969-806X(93)90320-T. (Cit. on pp. 4, 16).

[11] H. J. W. Strutt. "XV. On the light from the sky, its polarization and colour". *Philosophical Magazine Series 4* **41** 107–120 (1871). DOI: 10.1080/14786447108640452. (Cit. on pp. 4, 15).

[12] H. J. W. Strutt. "XXXVI. On the light from the sky, its polarization and colour". *Philosophical Magazine Series 4* **41** 274–279 (1871). DOI: 10.1080/14786447108640479. (Cit. on pp. 4, 15).

[13] H. J. W. Strutt. "LVIII. On the scattering of light by small particles". *Philosophical Magazine Series 4* **41** 447–454 (1871). DOI: 10.1080/14786447108640507. (Cit. on pp. 4, 15).

[14] R. K. Pradhan. "Does Rayleigh scattering explain the Blueness of Sky?" *Science Horizon* **28** 31 (2015) (cit. on p. 4).

[15] L. Meitner and H. Kösters. "Über die Streuung kurzwelliger γ-Strahlen". *Zeitschrift für Physik* **84** 137–144 (1933). DOI: 10.1007/BF01333827. (Cit. on pp. 4, 18).

[16] V. Costantini, B. De Tollis, and G. Pistoni. "Nonlinear effects in quantum electrodynamics". *Il Nuovo Cimento A Series 11* **2** 733–787 (1971). DOI: 10.1007/BF02736745. (Cit. on p. 4).

[17] S. Vavilov. "On the Attempt to Detect Collisions of Photons". *Physical Review* **36** 1590–1590 (1930). DOI: 10.1103/PhysRev.36.1590. (Cit. on pp. 4, 18).

[18] O. Halpern. "Scattering Processes Produced by Electrons in Negative Energy States". *Physical Review* **44** 855–856 (1933). DOI: 10.1103/PhysRev.44.855.2. (Cit. on pp. 4, 18).

[19] H. Euler and B. Kockel. "Über die Streuung von Licht an Licht nach der Diracschen Theorie". *Die Naturwissenschaften* **23** 246–247 (1935). DOI: 10.1007/BF01493898. (Cit. on pp. 4, 18).

[20] S. Z. Akhmadaliev et al. "Experimental Investigation of High-Energy Photon Splitting in Atomic Fields". *Physical Review Letters* **89** 061802 (2002). DOI: 10.1103/PhysRevLett.89.061802. (Cit. on pp. 5, 18).

[21] R. Lee. "Photon splitting in atomic fields". *Physics Reports* **373** 213–246 (2003). DOI: 10.1016/S0370-1573(02)00030-3. (Cit. on pp. 5, 18).

[22] V. Costantini, G. Pistoni, and B. De Tollis. "On the nonlinear effects in quantum electrodynamics: the coalescence of photons in a nuclear coulomb field". *Il Nuovo Cimento A* **46** 684–689 (1966). DOI: 10.1007/BF02857514. (Cit. on pp. 5, 18).

[23] G. Kirilin and I. Terekhov. "Coulomb corrections to the Delbrück scattering amplitude at low energies". *Physical Review A* **77** 032118 (2008). DOI: 10.1103/PhysRevA.77.032118. (Cit. on p. 5).

[24] P. Papatzacos and K. Mork. "Delbrück scattering". *Physics Reports* **21** 81–118 (1975). DOI: 10.1016/0370-1573(75)90048-4. (Cit. on pp. 5, 19).

[25] Z. Berant, R. Moreh, and S. Kahane. "Nuclear Thomson scattering of 5.5–7.2 MeV photons". *Physics Letters B* **69** 281–283 (1977). DOI: 10.1016/0370-2693(77)90545-7. (Cit. on pp. 5, 20).

[26] E. G. Fuller and E. Hayward. "The nuclear photoeffect in holmium and erbium". *Nuclear Physics* **30** 613–635 (1962). DOI: 10.1016/0029-5582(62)90081-0. (Cit. on pp. 5, 20).

[27] S. Kahane and R. Moreh. "Elastic scattering cross sections of 11.4 MeV photons from ^{206,207,208}Pb , ^{209}Bi, and ^{181}Ta". *Physical Review C* **50** 2000–2009 (1994). DOI: 10.1103/PhysRevC.50.2000. (Cit. on pp. 5, 20).

[28] P. P. Kane et al. "Elastic scattering of γ-rays and X-rays by atoms". *Physics Reports* **140** 75–159 (1986). DOI: 10.1016/0370-1573(86)90018-9. (Cit. on pp. 5, 14, 36).

[29] D. A. Bradley, O. D. Gonçalves, and P. P. Kane. "Measurements of photon-atom elastic scattering cross-sections in the photon energy range 1 keV to 4 MeV". *Radiation Physics and Chemistry* **56** 125–150 (1999). DOI: 10.1016/S0969-806X(99)00276-5. (Cit. on p. 5).

[30] S. Agostinelli et al. "Geant4—a simulation toolkit". *Nuclear Instruments and Methods in Physics Research Section A: Accelerators, Spectrometers, Detectors and Associated Equipment* **506** 250–303 (2003). DOI: 10.1016/S0168-9002(03)01368-8. (Cit. on p. 5).

[31] M. Batič et al. "Photon Elastic Scattering Simulation: Validation and Improvements to Geant4". *IEEE Transactions on Nuclear Science* **59** 1636–1664 (2012). DOI: 10.1109/TNS.2012.2203609. (Cit. on pp. 5, 36).

[32] J. H. Hubbell and P. M. Bergstrom. *Delbrück scattering: a bibliography, and some numerical comparisons with other photon interaction processes*. Tech. rep. 7115. NIST, 2004. URL: http://nvlpubs.nist.gov/nistpubs/ir/2004/ir7115.pdf (cit. on p. 5).

[33] S. Tashenov. "Hard X-Ray polarimetry with position sensitive germanium detectors - studies of the recombination transitions into highly charged ions". PhD thesis. Johann Wolfgang Goethe - Universität Frankfurt a. M., 2005. URL: http://web-docs.gsi.de/~stoe_exp/theses/tashenov_thesis.pdf (cit. on p. 5).

[34] S. Tashenov et al. "First Measurement of the Linear Polarization of Radiative Electron Capture Transitions". *Physical Review Letters* **97** 223202 (2006). DOI: 10.1103/PhysRevLett.97.223202. (Cit. on pp. 5, 99).

[35] H. Bräuning et al. "Polarization Measurements of Radiative Electron Capture Transitions in Highly Charged Ions". *AIP Conference Proceedings* **1099** 117–120 (2009). DOI: http://dx.doi.org/10.1063/1.3119992. (Cit. on p. 5).

[36] S. Hess. "Compton - Polarimetrie mit ortsauflösenden Röntgendetektoren". PhD thesis. Johann Wolfgang Goethe - Universität Frankfurt a. M., 2009. URL: http://web-docs.gsi.de/~stoe_exp/theses/hess_diss.pdf (cit. on pp. 5, 40, 98, 99).

[37] S. Hess et al. "Polarization studies of radiative electron capture into highly-charged uranium ions". *Journal of Physics: Conference Series* **163** 012072 (2009). DOI: 10.1088/1742-6596/163/1/012072. (Cit. on p. 5).

[38] S. Hess et al. "Polarized tunable monoenergetic x-rays produced by radiative electron capture into the K-shell of Xe^{54+}". *Journal of Physics: Conference Series* **194** 012025 (2009). DOI: 10.1088/1742-6596/194/1/012025. (Cit. on p. 5).

[39] G. Weber. "Untersuchung zur Anisotropie und linearen Polarisation radiativer Prozesse in energiereichen Ion-Atom-Stößen". PhD thesis. Ruprecht-Karls-Universität Heidelberg, 2010. URL: http://web-docs.gsi.de/~stoe_exp/theses/gweber_Diss.pdf (cit. on pp. 5, 40, 98).

[40] G. Weber et al. "Direct Determination of the Magnetic Quadrupole Contribution to the Lyman-α_1 Transition in a Hydrogenlike Ion". *Physical Review*

Letters **105** 243002 (2010). DOI: 10.1103/PhysRevLett.105.243002. (Cit. on pp. 5, 51, 85).

[41] F. Lei, A. J. Dean, and G. L. Hills. "Compton Polarimetry in Gamma-Ray Astronomy". *Space Science Reviews* **82** 309–388 (1997). DOI: 10.1023/A:1005027107614. (Cit. on pp. 5, 49).

[42] H. S. Krawczynski et al. "Scientific prospects for hard X-ray polarimetry". *Astroparticle Physics* **34** 550–567 (2011). DOI: 10.1016/j.astropartphys.2010.12.001. (Cit. on p. 5).

[43] M. Beilicke et al. "First flight of the X-ray polarimeter X-Calibur". *Aerospace Conference, 2015 IEEE*. 2015, 1–10. DOI: 10.1109/AERO.2015.7118915 (cit. on p. 5).

[44] M. C. Weisskopf et al. "Measurement of the X-ray polarization of the Crab Nebula". *The Astrophysical Journal* **208** L125 (1976). DOI: 10.1086/182247. (Cit. on p. 5).

[45] M. C. Weisskopf et al. "A precision measurement of the X-ray polarization of the Crab Nebula without pulsar contamination". *The Astrophysical Journal* **220** L117 (1978). DOI: 10.1086/182648. (Cit. on p. 5).

[46] A. J. Dean et al. "Polarized Gamma-Ray Emission from the Crab". *Science* **321** 1183–1185 (2008). DOI: 10.1126/science.1149056. (Cit. on p. 5).

[47] M. Forot et al. "Polarization of the Crab Pulsar and Nebula as Observed by the *INTEGRAL* /IBIS Telescope". *The Astrophysical Journal* **688** L29–L32 (2008). DOI: 10.1086/593974. (Cit. on p. 5).

[48] M. Chauvin et al. "POLARIMETRY IN THE HARD X-RAY DOMAIN WITH *INTEGRAL* SPI". *The Astrophysical Journal* **769** 137 (2013). DOI: 10.1088/0004-637X/769/2/137. (Cit. on p. 5).

[49] M. Chauvin et al. "Observation of polarized hard X-ray emission from the Crab by the *PoGOLite Pathfinder*". *Monthly Notices of the Royal Astronomical Society: Letters* **456** L84–L88 (2016). DOI: 10.1093/mnrasl/slv177. (Cit. on p. 5).

[50] D. Brini et al. "Elastic scattering of polarized photons". *Il Nuovo Cimento* **7** 877–890 (1958). DOI: 10.1007/BF02745592. (Cit. on p. 6).

[51] D. Brini et al. "Rayleigh scattering of polarized photons". *Il Nuovo Cimento* **11** 533–545 (1959). DOI: 10.1007/BF02726522. (Cit. on p. 6).

[52] D. R. S. Somayajulu and V. Lakshminarayana. "Rayleigh scattering of polarized photons". *Journal of Physics A: General Physics* **1** 228–235 (1968). DOI: 10.1088/0305-4470/1/2/307. (Cit. on p. 6).

[53] G. E. Ice, M. H. Chen, and B. Crasemann. "Photon-scattering cross sections of H_2 and He measured with synchrotron radiation". *Physical Review A* **17** 650–658 (1978). DOI: 10.1103/PhysRevA.17.650. (Cit. on p. 6).

[54] F. Smend et al. "Large-angle Rayleigh scattering of linearly polarized, hard synchrotron x rays by krypton and xenon". *Physical Review A* **36** 5189–5199 (1987). DOI: 10.1103/PhysRevA.36.5189. (Cit. on p. 6).

[55] E. Fuschini, D. S. R. Murty, and P. Veronesi. "Polarization effects in the elastic scattering of photons". *Il Nuovo Cimento* **15** 847–849 (1960). DOI: 10.1007/BF02732701. (Cit. on p. 6).

[56] D. R. S. Somayajulu, J. Rama Rao, and V. Lakshminarayana. "Polarization of elastically scattered gamma rays". *Il Nuovo Cimento B Series 10* **54** 281–292 (1968). DOI: 10.1007/BF02710746. (Cit. on p. 6).

[57] R. Moreh and J. Rajewski. "Polarization measurements of resonantly scattered capture gamma rays". *Nuclear Instruments and Methods* **98** 13–20 (1972). DOI: 10.1016/0029-554X(72)90418-1. (Cit. on p. 6).

[58] B. S. Sood. "Polarization of 0.411, 0.662 and 1.25 MeV γ-Rays Elastically Scattered by Lead". *Proceedings of the Royal Society A: Mathematical, Physical and Engineering Sciences* **247** 375–380 (1958). DOI: 10.1098/rspa.1958.0191. (Cit. on p. 6).

[59] G. Manuzio and S. Vitale. "Diffusione elastica di raggi γ di 1.25 MeV in piombo". *Il Nuovo Cimento* **20** 638–647 (1961). DOI: 10.1007/BF02731556. (Cit. on p. 6).

[60] M. Singh, S. Anand, and B. S. Sood. "Linear polarization of elastic scattering of 662 keV γ-rays". *Il Nuovo Cimento* **35** 1047–1051 (1965). DOI: 10.1007/BF02735523. (Cit. on p. 6).

[61] M. Singh and B. S. Sood. "Measurements of the linear polarization of elastically scattered gamma rays". *Nuclear Physics* **64** 502–512 (1965). DOI: 10.1016/0029-5582(65)90575-4. (Cit. on p. 6).

[62] R. A. Williams and K. G. McNeill. "POLARIZATION OF ELASTICALLY SCATTERED 1.33-MeV PHOTONS". *Canadian Journal of Physics* **43** 1078–1087 (1965). DOI: 10.1139/p65-107. (Cit. on p. 6).

[63] M. Cooper and W. Stirling. "Magnetic X-ray scattering". *Radiation Physics and Chemistry* **56** 85–99 (1999). DOI: 10.1016/S0969-806X(99)00275-3. (Cit. on p. 6).

[64] S. Tashenov et al. "Measurement of the Correlation between Electron Spin and Photon Linear Polarization in Atomic-Field Bremsstrahlung". *Physical Review Letters* **107** 173201 (2011). DOI: 10.1103/PhysRevLett.107.173201. (Cit. on p. 7).

[65] R. Märtin. "Röntgenpolarimetrie angewandt zur Untersuchung der Bremsstrahlung spinpolarisierter Elektronen". PhD thesis. Ruprecht-Karls-Universität Heidelberg, 2011. URL: http://web-docs.gsi.de/~stoe_exp/theses/thesis_rmaertin.pdf (cit. on pp. 7, 40).

[66] R. Märtin et al. "Polarization Transfer of Bremsstrahlung Arising from Spin-Polarized Electrons". *Physical Review Letters* **108** 264801 (2012). DOI: 10.1103/PhysRevLett.108.264801. (Cit. on pp. 7, 51).

[67] R. Märtin et al. "Target-thickness effects in electron–atom bremsstrahlung". *Physica Scripta* **T156** 014070 (2013). DOI: 10.1088/0031-8949/2013/T156/014070. (Cit. on p. 7).

[68] S. Tashenov et al. "Observation of the spin–orbit interaction in bremsstrahlung". *Physica Scripta* **T156** 014071 (2013). DOI: 10.1088/0031-8949/2013/T156/014071. (Cit. on p. 7).

[69] O. Kovtun et al. "Spin-orbit interaction in bremsstrahlung and its effect on the electron motion in a strong Coulomb field". *Physical Review A* **92** 062707 (2015). DOI: 10.1103/PhysRevA.92.062707. (Cit. on p. 7).

[70] S. Tashenov et al. "Bremsstrahlung polarization correlations and their application for polarimetry of electron beams". *Physical Review A* **87** 022707 (2013). DOI: 10.1103/PhysRevA.87.022707. (Cit. on p. 7).

[71] S. Tashenov et al. "Electron polarimetry with bremsstrahlung". *Journal of Physics: Conference Series* **488** 012057 (2014). DOI: 10.1088/1742-6596/488/1/012057. (Cit. on p. 7).

[72] A. Surzhykov et al. “Application of Radiative Electron Capture for the Diagnostics of Spin-Polarized Ion Beams at Storage Rings”. *Physical Review Letters* **94** 203202 (2005). DOI: 10.1103/PhysRevLett.94.203202. (Cit. on pp. 7, 99).

[73] W. Henning. “FAIR — An International Accelerator Facility for Research with Ions and Antiprotons”. *AIP Conference Proceedings* **773** 3–5 (2005). DOI: http://dx.doi.org/10.1063/1.1949487. (Cit. on p. 7).

[74] N. L. Manakov et al. “Circular dichroism effects in atomic x-ray scattering”. *Physical Review A* **61** 032711 (2000). DOI: 10.1103/PhysRevA.61.032711. (Cit. on pp. 7, 36).

[75] N. L. Manakov et al. “Photon-polarization effects and their angular dependence in relativistic two-photon bound-bound transitions”. *Journal of Physics B: Atomic, Molecular and Optical Physics* **33** 4425–4446 (2000). DOI: 10.1088/0953-4075/33/20/317. (Cit. on pp. 7, 35, 36).

[76] L. Safari et al. “Relativistic polarization analysis of Rayleigh scattering by atomic hydrogen”. *Physical Review A* **86** 043405 (2012). DOI: 10.1103/PhysRevA.86.043405. (Cit. on p. 7).

[77] A. Surzhykov et al. “Polarization correlations in the elastic Rayleigh scattering of photons by hydrogenlike ions”. *Physical Review A* **88** 062515 (2013). DOI: 10.1103/PhysRevA.88.062515. (Cit. on pp. 7, 17).

[78] L. Safari et al. “Spin effects probed by Rayleigh X-ray scattering off hydrogenic ions”. *Radiation Physics and Chemistry* **106** 271–277 (2015). DOI: 10.1016/j.radphyschem.2014.08.007. (Cit. on p. 7).

[79] A. Surzhykov et al. “Rayleigh x-ray scattering from many-electron atoms and ions”. *Journal of Physics B: Atomic, Molecular and Optical Physics* **48** 144015 (2015). DOI: 10.1088/0953-4075/48/14/144015. (Cit. on pp. 7, 17, 90).

[80] A. V. Volotka et al. “Many-electron effects on x-ray Rayleigh scattering by highly charged He-like ions”. *Physical Review A* **93** 023418 (2016). DOI: 10.1103/PhysRevA.93.023418. (Cit. on pp. 7, 18).

[81] M. J. Berger et al. *NIST XCOM: Photon Cross Sections Database*. URL: http://www.nist.gov/pml/data/xcom/ (visited on 05/06/2015) (cit. on pp. 9, 65).

[82] W. R. Leo. *Techniques for Nuclear and Particle Physics Experiments*. Berlin, Heidelberg: Springer Berlin Heidelberg, 1994. ISBN: 978-3-540-57280-0 978-3-642-57920-2. URL: http://link.springer.com/10.1007/978-3-642-57920-2 (visited on 12/02/2015) (cit. on pp. 10, 23, 42).

[83] A. H. Compton. "A Quantum Theory of the Scattering of X-rays by Light Elements". *Physical Review* **21** 483–502 (1923). DOI: 10.1103/PhysRev.21.483. (Cit. on p. 11).

[84] G. Drake, ed. *Springer Handbook of Atomic, Molecular, and Optical Physics*. New York, NY: Springer New York, 2006. ISBN: 978-0-387-20802-2 978-0-387-26308-3. URL: http://link.springer.com/10.1007/978-0-387-26308-3 (visited on 08/19/2015) (cit. on p. 11).

[85] O. Klein and Y. Nishina. "Über die Streuung von Strahlung durch freie Elektronen nach der neuen relativistischen Quantendynamik von Dirac". *Zeitschrift für Physik* **52** 853–868 (1929). DOI: 10.1007/BF01366453. (Cit. on p. 11).

[86] P. M. Bergstrom and R. H. Pratt. "An overview of the theories used in compton scattering calculations". *Radiation Physics and Chemistry* **50** 3–29 (1997). DOI: 10.1016/S0969-806X(97)00022-4. (Cit. on pp. 12, 13).

[87] B. Chatterjee, L. LaJohn, and S. Roy. "Investigations on compton scattering: New directions". *Radiation Physics and Chemistry* **75** 2165–2173 (2006). DOI: 10.1016/j.radphyschem.2006.03.073. (Cit. on p. 12).

[88] R. Ribberfors. "Relationship of the relativistic Compton cross section to the momentum distribution of bound electron states". *Physical Review B* **12** 2067–2074 (1975). DOI: 10.1103/PhysRevB.12.2067. (Cit. on p. 13).

[89] R. Ribberfors and K. F. Berggren. "Incoherent-x-ray-scattering functions and cross sections $(\mathrm{d}\sigma/\mathrm{d}\Omega')_{\mathrm{incoh}}$ by means of a pocket calculator". *Physical Review A* **26** 3325–3333 (1982). DOI: 10.1103/PhysRevA.26.3325. (Cit. on p. 13).

[90] J. H. Hubbell et al. "Atomic form factors, incoherent scattering functions, and photon scattering cross sections". *Journal of Physical and Chemical Reference Data* **4** 471 (1975). DOI: 10.1063/1.555523. (Cit. on pp. 13, 15).

[91] Y. Namito et al. "Compton scattering of 20- to 40-keV photons". *Physical Review A* **51** 3036–3043 (1995). DOI: 10.1103/PhysRevA.51.3036. (Cit. on p. 13).

[92] J. H. Hubbell. "Summary of existing information on the incoherent scattering of photons, particularly on the validity of the use of the incoherent scattering function". *Radiation Physics and Chemistry* **50** 113–124 (1997). DOI: 10.1016/S0969-806X(97)00049-2. (Cit. on p. 13).

[93] S. C. Roy, L. Kissel, and R. H. Pratt. "Elastic scattering of photons". *Radiation Physics and Chemistry* **56** 3–26 (1999). DOI: 10.1016/S0969-806X(99)00286-8. (Cit. on pp. 13, 16, 17).

[94] J. J. Thomson. *Conduction of electricity through gases*. 2nd ed. Cambridge Physical series. Cambridge: Cambridge University Press, 1906 (cit. on p. 15).

[95] W. Franz. "Rayleighsche Streuung harter Strahlung an schweren Atomen". *Zeitschrift für Physik* **98** 314–320 (1935). DOI: 10.1007/BF01331074. (Cit. on p. 15).

[96] J. H. Hubbell and I. Øverbø. "Relativistic atomic form factors and photon coherent scattering cross sections". *Journal of Physical and Chemical Reference Data* **8** 69 (1979). DOI: 10.1063/1.555593. (Cit. on p. 15).

[97] D. Schaupp et al. "Small-Angle Rayleigh Scattering of Photons at High Energies: Tabulations of Relativistic HFS Modified Atomic Form Factors". *Journal of Physical and Chemical Reference Data* **12** 467 (1983). DOI: 10.1063/1.555690. (Cit. on p. 15).

[98] L. Kissel et al. "The validity of form-factor, modified-form-factor and anomalous-scattering-factor approximations in elastic scattering calculations". *Acta Crystallographica Section A Foundations of Crystallography* **51** 271–288 (1995). DOI: 10.1107/S010876739400886X. (Cit. on pp. 16, 20).

[99] A. Surzhykov et al. "Photon polarization in the two-photon decay of heavy hydrogen-like ions". *The European Physical Journal Special Topics* **169** 29–34 (2009). DOI: 10.1140/epjst/e2009-00969-8. (Cit. on p. 16).

[100] A. Surzhykov, R. H. Pratt, and S. Fritzsche. "Two-photon decay of inner-shell vacancies in heavy atoms". *Physical Review A* **88** 042512 (2013). DOI: 10.1103/PhysRevA.88.042512. (Cit. on p. 16).

[101] G. E. Brown and J. B. Woodward. "Coherent Scattering of Gamma-Rays by Bound Electrons". *Proceedings of the Physical Society. Section A* **65** 977–980 (1952). DOI: 10.1088/0370-1298/65/12/303. (Cit. on p. 16).

[102] G. E. Brown, R. E. Peierls, and J. B. Woodward. "The Coherent Scattering of γ-rays by K Electrons in Heavy Atoms. I. Method". *Proceedings of the Royal Society A: Mathematical, Physical and Engineering Sciences* **227** 51–58 (1954). DOI: 10.1098/rspa.1954.0279. (Cit. on p. 16).

[103] S. Brenner, G. E. Brown, and J. B. Woodward. "The Coherent Scattering of γ-rays by K Electrons in Heavy Atoms. II. The Scattering of 0.32 mc^2 γ-rays in Mercury". *Proceedings of the Royal Society A: Mathematical, Physical and Engineering Sciences* **227** 59–72 (1954). DOI: 10.1098/rspa.1954.0280. (Cit. on p. 16).

[104] G. E. Brown and D. F. Mayers. "The Coherent Scattering of γ-rays by K Electrons in Heavy Atoms. III. The Scattering of 0.64 mc^2 γ-Rays in Mercury". *Proceedings of the Royal Society A: Mathematical, Physical and Engineering Sciences* **234** 387–390 (1956). DOI: 10.1098/rspa.1956.0042. (Cit. on p. 16).

[105] G. E. Brown and D. F. Mayers. "The Coherent Scattering of γ-rays by K Electrons in Heavy Atoms. IV. The Scattering of 1.28 and 2.56mc^2 γ-rays in Mercury". *Proceedings of the Royal Society A: Mathematical, Physical and Engineering Sciences* **242** 89–95 (1957). DOI: 10.1098/rspa.1957.0155. (Cit. on p. 16).

[106] A. Surzhykov, V. A. Yerokhin, and S. Fritzsche. *Private communication.* 2014 (cit. on pp. 16, 36, 90, 134).

[107] P. A. M. Dirac. *The principles of quantum mechanics.* 3rd ed. London: Oxford University Press, 1947 (cit. on p. 17).

[108] R. H. Pratt. "Tutorial on fundamentals of radiation physics:" *Radiation Physics and Chemistry* **70** 595–603 (2004). DOI: 10.1016/j.radphyschem.2003.12.032. (Cit. on p. 17).

[109] M. Schumacher. "Delbrück scattering". *Radiation Physics and Chemistry* **56** 101–111 (1999). DOI: 10.1016/S0969-806X(99)00289-3. (Cit. on p. 18).

[110] W. Muckenheim and M. Schumacher. "Delbruck and Rayleigh scattering by uranium investigated at photon energies between 0.1 and 1.5 MeV". *Journal of Physics G: Nuclear Physics* **6** 1237 (1980). URL: http://iopscience.iop.org/0305-4616/6/10/010 (visited on 06/27/2012) (cit. on p. 19).

[111] P. Rullhusen et al. "Test of vacuum polarization by precise investigation of Delbrück scattering". *Physical Review C* **23** 1375 (1981). URL: http://prc.aps.org/abstract/PRC/v23/i4/p1375_1 (visited on 06/27/2012) (cit. on p. 20).

[112] R. Capote et al. "RIPL – Reference Input Parameter Library for Calculation of Nuclear Reactions and Nuclear Data Evaluations". *Nuclear Data Sheets* **110** 3107–3214 (2009). DOI: 10.1016/j.nds.2009.10.004. (Cit. on p. 20).

[113] R. Capote et al. *RIPL-3: Reference Input Parameter Library*. URL: https://www-nds.iaea.org/RIPL-3/ (visited on 12/27/2015) (cit. on p. 20).

[114] J. H. Hubbell. "Electron–positron pair production by photons: A historical overview". *Radiation Physics and Chemistry* **75** 614–623 (2006). DOI: 10.1016/j.radphyschem.2005.10.008. (Cit. on p. 21).

[115] H. F. Beyer, H.-J. Kluge, and V. P. Shevelko. *X-Ray Radiation of Highly Charged Ions*. Berlin, Heidelberg: Springer Berlin Heidelberg, 1997. ISBN: 978-3-642-08323-5 978-3-662-03495-8. URL: http://link.springer.com/10.1007/978-3-662-03495-8 (visited on 12/02/2015) (cit. on p. 22).

[116] V. V. Balashov, A. N. Grum-Grzhimailo, and N. M. Kabachnik. *Polarization and Correlation Phenomena in Atomic Collisions*. Boston, MA: Springer US, 2000. ISBN: 978-1-4419-3328-7 978-1-4757-3228-3. URL: http://link.springer.com/10.1007/978-1-4757-3228-3 (visited on 01/12/2016) (cit. on p. 22).

[117] L. Meitner. "Über die Entstehung der β-Strahl-Spektren radioaktiver Substanzen". *Zeitschrift für Physik* **9** 131–144 (1922). DOI: 10.1007/BF01326962. (Cit. on p. 22).

[118] P. Auger. "Sur les rayons β secondaires produits dans un gaz par des rayons X". *Compt. Rend.* **180** 65–68 (1925). URL: http://gallica.bnf.fr/ark:/12148/bpt6k3133k/f65.image.langEN (cit. on p. 22).

[119] M. F. Hasoglu. "Calculations of K-shell fluorescence yields and photoabsorption cross sections for carbon ions at the K-edge". PhD thesis. Western Michigan University, 2008 (cit. on p. 22).

[120] G. Wentzel. "Über strahlungslose Quantensprünge". *Zeitschrift für Physik* **43** 524–530 (1927). DOI: 10.1007/BF01397631. (Cit. on p. 22).

[121] J. C. Russ. *Fundamentals of energy dispersive x-ray analysis*. Butterworths monographs in materials. London; Boston: Butterworths, 1984. ISBN: 978-0-408-11031-0 (cit. on p. 22).

[122] A. Einstein. "The motion of elements suspended in static liquids as claimed in the molecular kinetic theory of heat". *Annalen der Physik* **17** 549–560 (1905). ISSN: 0003-3804 (cit. on p. 25).

[123] J. Durst. "Modellierung und Simulation physikalischer Eigenschaften photonenzählender Röntgenpixeldetektoren für die Bildgebung". PhD thesis. Friedrich-Alexander-Universität Erlangen-Nürnberg, 2008. URL: http://www.ecap.nat.uni-erlangen.de/publications/pub/2008_Durst_Dissertation.pdf (cit. on pp. 25, 65).

[124] A. Korn. "Spektrale und bildgebende Eigenschaften photonenzählender Röntgendetektoren am Beispiel des Medipix-Detektors". PhD thesis. Friedrich-Alexander-Universität Erlangen-Nürnberg, 2007. URL: https://opus4.kobv.de/opus4-fau/files/447/AlexanderKornDissertation.pdf (cit. on p. 25).

[125] DESY. *Wiggler (schematic)*. URL: http://photon-science.desy.de/sites/site_photonscience/content/e62/e189219/e189248/e189389/e196698/e189410/wiggler_eng.png (visited on 08/31/2015) (cit. on p. 26).

[126] DESY. *Undulator (schematic)*. URL: http://photon-science.desy.de/sites/site_photonscience/content/e62/e189219/e189248/e189389/e196698/e189412/undulator_eng.png (visited on 08/30/2015) (cit. on p. 26).

[127] D. T. Attwood. *Soft x-rays and extreme ultraviolet radiation: principles and applications*. 1. paperback version, digitally printed (with amendments). Cambridge: Cambridge Univ. Press, 2007. ISBN: 978-0-521-02997-1 978-0-521-65214-8 (cit. on pp. 25, 26).

[128] G. G. Stokes. "On the Composition and Resolution of Streams of Polarized Light from different Sources". *Transactions of the Cambridge Philosophical Society* **9** 399 (1852) (cit. on p. 29).

[129] W. H. McMaster. "Matrix Representation of Polarization". *Reviews of Modern Physics* **33** 8–28 (1961). DOI: 10.1103/RevModPhys.33.8. (Cit. on pp. 29, 33, 34).

[130] B. Marx et al. “High-Precision X-Ray Polarimetry”. *Physical Review Letters* **110** 254801 (2013). DOI: 10.1103/PhysRevLett.110.254801. (Cit. on pp. 30, 99).

[131] U. Fano. “Remarks on the Classical and Quantum-Mechanical Treatment of Partial Polarization”. *Journal of the Optical Society of America* **39** 859 (1949). DOI: 10.1364/JOSA.39.000859. (Cit. on pp. 34, 67).

[132] J. P. J. Carney et al. “Elastic photon scattering from excited states of atoms and ions”. *Radiation Physics and Chemistry* **51** 371–372 (1998). DOI: 10.1016/S0969-806X(97)00142-4. (Cit. on p. 36).

[133] L. Kissel. “RTAB: the Rayleigh scattering database”. *Radiation Physics and Chemistry* **59** 185–200 (2000). DOI: 10.1016/S0969-806X(00)00290-5. (Cit. on p. 36).

[134] L. Kissel. *RTAB (Rayleigh Scattering Database)*. URL: http://starship.org/RTAB/RTAB.php (visited on 12/16/2015) (cit. on p. 36).

[135] D. E. Cullen, J. H. Hubbell, and L. Kissel. *Photon and Electron Interaction Data*. URL: https://www-nds.iaea.org/epdl97/ (visited on 01/03/2016) (cit. on p. 36).

[136] *Helmholtz Association of German Research Centres*. URL: http://www.helmholtz.de/en/ (visited on 01/22/2016) (cit. on p. 38).

[137] DESY. *PETRA III - Facility Information*. URL: http://photon-science.desy.de/facilities/petra_iii/facility_information/index_eng.html (visited on 08/31/2015) (cit. on p. 38).

[138] N. Schell et al. “The High Energy Materials Science Beamline (HEMS) at PETRA III”. *Materials Science Forum* **772** 57–61 (2013). DOI: 10.4028/www.scientific.net/MSF.772.57. (Cit. on p. 38).

[139] DESY. *PETRA III - P07 - Unified Data Sheet*. URL: http://photon-science.desy.de/facilities/petra_iii/beamlines/p07_high_energy_materials_science/unified_data_sheet_p07/index_eng.html (visited on 08/31/2015) (cit. on p. 38).

[140] DESY. *PETRA III - P07 - Optics*. URL: http://photon-science.desy.de/facilities/petra_iii/beamlines/p07_high_energy_materials_science/optics/index_eng.html (visited on 08/31/2015) (cit. on p. 38).

[141] DESY. *PETRA III - P07 - Optics (schematic).* URL: http://photon-science.desy.de/sites/site_photonscience/content/e58/e176720/e177229/e178413/e178435/e178439/Optik_eng.pdf (visited on 08/31/2015) (cit. on pp. 38, 39).

[142] ORTEC. *GLP Series Planar HPGe Low-Energy Detector Product Configuration Guide.* URL: www.ortec-online.com/download/glp.pdf (visited on 08/31/2015) (cit. on p. 39).

[143] T. Stöhlker et al. "SPARC: The Stored Particle Atomic Research Collaboration At FAIR". *AIP Conference Proceedings* **1336** 132–137 (2011). DOI: http://dx.doi.org/10.1063/1.3586073. (Cit. on p. 40).

[144] D. Protić et al. "Large-volume Si(Li) orthogonal-strip detectors for Compton-effect-based instruments". *IEEE Transactions on Nuclear Science* **52** 3181–3185 (2005). DOI: 10.1109/TNS.2005.862930. (Cit. on p. 40).

[145] S. Chu, L. Ekström, and R. Firestone. *The Lund/LBNL Nuclear Data Search.* URL: http://nucleardata.nuclear.lu.se/toi/ (visited on 09/04/2015) (cit. on p. 45).

[146] F. Metzger and M. Deutsch. "A Study of the Polarization-Direction Correlation of Successive Gamma-Ray Quanta". *Physical Review* **78** 551–558 (1950). DOI: 10.1103/PhysRev.78.551. (Cit. on p. 49).

[147] S. P. Collins et al. "A polarimeter for circularly polarised synchrotron radiation". *Nuclear Instruments and Methods in Physics Research Section A: Accelerators, Spectrometers, Detectors and Associated Equipment* **290** 254–256 (1990). DOI: 10.1016/0168-9002(90)90370-L. (Cit. on p. 49).

[148] R. A. Sareen et al. "High-resolution integrated germanium Compton polarimeter for the γ-ray energy range 80 keV–1 MeV". *Review of Scientific Instruments* **66** 3653 (1995). DOI: 10.1063/1.1145483. (Cit. on p. 49).

[149] P. Soffitta et al. "Techniques and detectors for polarimetry in X-ray astronomy". *Nuclear Instruments and Methods in Physics Research Section A: Accelerators, Spectrometers, Detectors and Associated Equipment* **510** 170–175 (2003). DOI: 10.1016/S0168-9002(03)01694-2. (Cit. on p. 49).

[150] S. Tashenov. "Circular polarimetry with gamma-ray tracking detectors". *Nuclear Instruments and Methods in Physics Research Section A: Accelerators, Spectrometers, Detectors and Associated Equipment* **640** 164–169 (2011). DOI: 10.1016/j.nima.2011.03.011. (Cit. on p. 50).

[151] S. Tashenov et al. "Hard X-ray polarimetry by means of Rayleigh scattering". *Nuclear Instruments and Methods in Physics Research Section A: Accelerators, Spectrometers, Detectors and Associated Equipment* **600** 599–603 (2009). DOI: 10.1016/j.nima.2008.11.145. (Cit. on p. 50).

[152] G. Weber et al. "Performance of a position sensitive Si(Li) x-ray detector dedicated to Compton polarimetry of stored and trapped highly-charged ions". *Journal of Instrumentation* **5** C07010–C07010 (2010). DOI: 10.1088/1748-0221/5/07/C07010. (Cit. on p. 51).

[153] G. Weber et al. "Compton polarimeters for the study of hard X-rays arising from energetic collisions of electrons and ions with matter". *AIP Conference Proceedings* **1438** 73–79 (2012). DOI: http://dx.doi.org/10.1063/1.4707858. (Cit. on p. 51).

[154] S. Puri et al. "Differential cross section measurements for the elastic scattering of 59.5 keV photons by elements in the atomic region $13 \leq Z \leq 82$". *Nuclear Instruments and Methods in Physics Research Section B: Beam Interactions with Materials and Atoms* **111** 209–214 (1996). DOI: 10.1016/0168-583X(95)01341-5. (Cit. on p. 54).

[155] J. Shahi et al. "Large-angle elastic scattering of 59.54-keV photons by elements with $12 \leq Z \leq 92$". *Physical Review A* **57** 4327–4334 (1998). DOI: 10.1103/PhysRevA.57.4327. (Cit. on p. 54).

[156] A. C. Thompson et al. *X-ray Data Booklet*. 3rd ed. Lawrence Berkeley Laboratory, 2009. URL: http://xdb.lbl.gov/ (cit. on pp. 55, 59, 62).

[157] R. Helmer and M. Lee. "Analytical functions for fitting peaks from Ge semiconductor detectors". *Nuclear Instruments and Methods* **178** 499–512 (1980). DOI: 10.1016/0029-554X(80)90830-7. (Cit. on pp. 57, 58).

[158] G. W. Phillips and K. W. Marlow. "Automatic analysis of gamma-ray spectra from germanium detectors". *Nuclear Instruments and Methods* **137** 525–536 (1976). DOI: 10.1016/0029-554X(76)90472-9. (Cit. on p. 58).

[159] L. Longoria et al. “Analytical peak fitting for gamma-ray spectrum analysis with Ge detectors”. *Nuclear Instruments and Methods in Physics Research Section A: Accelerators, Spectrometers, Detectors and Associated Equipment* **299** 308–312 (1990). DOI: 10.1016/0168-9002(90)90797-A. (Cit. on p. 58).

[160] P.-M. Hillenbrand and D. Banaś. *Private communication*. 2014 (cit. on pp. 60, 134).

[161] H. Hirayama et al. *The EGS5 code system*. United States. Department of Energy, 2005. URL: http://ccdb5fs.kek.jp/tiff/2005/0524/0524008.pdf (visited on 07/09/2012) (cit. on p. 61).

[162] G. Weber. *Private communication*. 2015 (cit. on pp. 61, 134).

[163] G. Weber et al. “Monte Carlo simulations for the characterization of position-sensitive x-ray detectors dedicated to Compton polarimetry”. *Physica Scripta* **T144** 014034 (2011). DOI: 10.1088/0031-8949/2011/T144/014034. (Cit. on p. 61).

[164] W. Verkerke and D. Kirkby. “The RooFit toolkit for data modeling”. *ArXiv Physics e-prints* (2003). URL: http://adsabs.harvard.edu/abs/2003physics...6116V (cit. on p. 61).

[165] A. Surzhykov. *Private communication*. 2014 (cit. on pp. 62, 134).

[166] M. O. Krause. “Atomic radiative and radiationless yields for K and L shells”. *Journal of Physical and Chemical Reference Data* **8** 307 (1979). DOI: 10.1063/1.555594. (Cit. on p. 62).

[167] T. Stöhlker et al. “Angular Distribution Studies for the Time-Reversed Photoionization Process in Hydrogenlike Uranium: The Identification of Spin-Flip Transitions”. *Physical Review Letters* **82** 3232–3235 (1999). DOI: 10.1103/PhysRevLett.82.3232. (Cit. on p. 63).

[168] R. Brun and F. Rademakers. “ROOT — An object oriented data analysis framework”. *Nuclear Instruments and Methods in Physics Research Section A: Accelerators, Spectrometers, Detectors and Associated Equipment* **389** 81–86 (1997). DOI: 10.1016/S0168-9002(97)00048-X. (Cit. on p. 66).

[169] L. Devroye. *Non-uniform random variate generation*. New York: Springer-Verlag, 1986. ISBN: 0-387-96305-7 978-0-387-96305-1 3-540-96305-7 978-3-540-96305-9. URL: http://luc.devroye.org/rnbookindex.html (cit. on p. 66).

[170] B. Efron. "Bootstrap Methods: Another Look at the Jackknife". *The Annals of Statistics* **7** 1–26 (1979). DOI: 10.1214/aos/1176344552. (Cit. on p. 72).

[171] L. Safari et al. "Relativistic total cross section and angular distribution for Rayleigh scattering by atomic hydrogen". *Physical Review A* **85** 043406 (2012). DOI: 10.1103/PhysRevA.85.043406. (Cit. on p. 89).

[172] K. Horikawa et al. "Neutron angular distribution in (γ, n) reactions with linearly polarized γ-ray beam generated by laser Compton scattering". *Physics Letters B* **737** 109–113 (2014). DOI: 10.1016/j.physletb.2014.08.024. (Cit. on p. 98).

[173] U. Spillmann et al. "Performance of a Ge-microstrip imaging detector and polarimeter". *Review of Scientific Instruments* **79** 083101 (2008). DOI: 10.1063/1.2963046. (Cit. on p. 98).

[174] U. Spillmann. "Charakterisierung und erster experimenteller Einsatz von ortsauflösenden, energiedispersiven Germanium-Detektoren zur Präzisionsspektroskopie an schweren Ionen". PhD thesis. Johann Wolfgang Goethe - Universität Frankfurt a. M., 2009. URL: http://web-docs.gsi.de/~stoe_exp/theses/spillmann_thesis.pdf (cit. on p. 98).

[175] K. Vetter, M. Burks, and L. Mihailescu. "Gamma-ray imaging with position-sensitive HPGe detectors". *Nuclear Instruments and Methods in Physics Research Section A: Accelerators, Spectrometers, Detectors and Associated Equipment* **525** 322–327 (2004). DOI: 10.1016/j.nima.2004.03.087. (Cit. on p. 98).

[176] A. Bondarevskaya et al. "Theory of the polarization of highly charged ions in storage rings: Production, preservation, observation and application to the search for a violation of the fundamental symmetries". *Physics Reports* **507** 1–42 (2011). DOI: 10.1016/j.physrep.2011.06.001. (Cit. on p. 99).

[177] T. Stöhlker et al. "SPARC experiments at the high-energy storage ring". *Physica Scripta* **T156** 014085 (2013). DOI: 10.1088/0031-8949/2013/T156/014085. (Cit. on p. 99).

[178] J. Eichler and A. Ichihara. "Polarization of photons emitted in radiative electron capture by bare high- Z ions". *Physical Review A* **65** 052716 (2002). DOI: 10.1103/PhysRevA.65.052716. (Cit. on p. 99).

[179] A. Gumberidze et al. “Electron- and Proton-Impact Excitation of Hydrogen-like Uranium in Relativistic Collisions”. *Physical Review Letters* **110** 213201 (2013). DOI: 10.1103/PhysRevLett.110.213201. (Cit. on p. 100).

[180] A. Gumberidze et al. “Shell- and subshell-resolved projectile excitation of hydrogenlike Au^{78+} ions in relativistic ion-atom collisions”. *Physical Review A* **82** 052712 (2010). DOI: 10.1103/PhysRevA.82.052712. (Cit. on p. 100).

[181] D.-C. Ionescu and T. Stöhlker. “Asymptotic energy dependence of projectile excitation in relativistic ion-atom collisions”. *Physical Review A* **67** 022705 (2003). DOI: 10.1103/PhysRevA.67.022705. (Cit. on p. 100).

List of Figures

List of Tables

A Derivation of the transfer matrix from the differential cross section

Starting point is the differential Rayleigh scattering cross section given by equation 3.25. Using the definitions

$$\begin{aligned} d_1 &:= \frac{1}{4} \cdot \left(\left| A_\parallel \right|^2 + \left| A_\perp \right|^2 \right), \\ d_2 &:= \frac{1}{4} \cdot \left(\left| A_\parallel \right|^2 - \left| A_\perp \right|^2 \right), \\ d_3 &:= \frac{1}{2} \cdot \Re \left\{ A_\parallel \cdot A_\perp^* \right\}, \\ d_4 &:= \frac{1}{2} \cdot \Im \left\{ A_\parallel \cdot A_\perp^* \right\}, \end{aligned} \tag{A.1}$$

the differential cross section is given by

$$\frac{\mathrm{d}\sigma}{\mathrm{d}\Omega} = d_1 \cdot (1 + \xi_1 \xi_1') + d_2 \cdot (\xi_1 + \xi_1') + d_3 \cdot (\xi_2 \xi_2' + \xi_3 \xi_3') + d_4 \cdot (\xi_2 \xi_3' - \xi_3 \xi_2'). \tag{A.2}$$

Defining the Stokes vector for a single photon

$$\boldsymbol{\xi} := \begin{pmatrix} 1 \\ \xi_1 \\ \xi_2 \\ \xi_3 \end{pmatrix} \tag{A.3}$$

allows to use an even more compact form for the differential cross section:

$$\frac{\mathrm{d}\sigma}{\mathrm{d}\Omega}(\boldsymbol{\xi}', \boldsymbol{\xi}) = \boldsymbol{\xi}'^T \cdot H \cdot \boldsymbol{\xi} \tag{A.4}$$

with the matrix

$$H = \begin{pmatrix} d_1 & d_2 & 0 & 0 \\ d_2 & d_1 & 0 & 0 \\ 0 & 0 & d_3 & -d_4 \\ 0 & 0 & d_4 & d_3 \end{pmatrix}. \tag{A.5}$$

Equation A.4 will in the following be used to derive the relation between the Stokes vectors $\boldsymbol{S}$ (incident beam) and $\boldsymbol{S}'$ (scattered beam). For this, both the incident

and the scattered beam are decomposed into portions with orthogonal polarization states (here shown for the incident beam, for the scattered beam simply add primes to all quantities):

$$\begin{aligned} S_0 &= I_\parallel + I_\perp \qquad (\parallel \text{ and } \perp \text{ to the scattering plane}) \\ &= I_\nearrow + I_\searrow \qquad (\pm 45^\circ \text{ with respect to the scattering plane}) \\ &= I_R + I_L \qquad (\text{right- and left-handed circular polarization}) \end{aligned} \tag{A.6}$$

The partial intensities I_x are directly connected to certain choices of the (single-photon) Stokes parameters ξ_i:

$$\begin{aligned} I_\parallel &= I(\xi_1 = 1), \qquad I_\perp = I(\xi_1 = -1), \\ I_\nearrow &= I(\xi_2 = 1), \qquad I_\searrow = I(\xi_2 = -1), \\ I_R &= I(\xi_3 = 1), \qquad I_L = I(\xi_3 = -1). \end{aligned} \tag{A.7}$$

For all these cases, the respective other Stokes parameters vanish according to equation 3.11. The single-photon Stokes vector can then be written as

$$\boldsymbol{\xi}_{j,m} = \boldsymbol{e}_0 + \lambda_m \cdot \boldsymbol{e}_j, \qquad j = 1,2,3 \text{ and } \lambda_m = \begin{cases} +1 & m = 1 \\ -1 & m = 2 \end{cases}, \tag{A.8}$$

where the $\boldsymbol{e}_\mu$ are four-component standard unit vectors ($\mu = 0,1,2,3$). Using the relations from equations 3.12 and A.6 together with the notation given by equation A.7, one finds for all $j = 1,2,3$:

$$\begin{aligned} S_0 &= I(\xi_j = 1) + I(\xi_j = -1), \\ S_j &= I(\xi_j = 1) - I(\xi_j = -1). \end{aligned} \tag{A.9}$$

In matrix form, equation A.9 reads:

$$\begin{pmatrix} S_0 \\ S_j \end{pmatrix} = G \cdot \begin{pmatrix} I(\xi_j = 1) \\ I(\xi_j = -1) \end{pmatrix} \tag{A.10}$$

with

$$G = \begin{pmatrix} 1 & 1 \\ 1 & -1 \end{pmatrix} = 2 \cdot G^{-1}. \tag{A.11}$$

The next step will be to relate the partial intensities $I(\xi_j = \lambda_m)$ of the incident and scattered beam. For any combination $i, j = 1, 2, 3$, one has:

$$\begin{aligned} I(\xi_i' = \lambda_m) &= \sum_{n=1,2} \frac{\mathrm{d}\sigma}{\mathrm{d}\Omega}(\xi_i' = \lambda_m, \xi_j = \lambda_n) \cdot I(\xi_j = \lambda_n) \\ &= \sum_{n=1,2} \boldsymbol{\xi}_{i,m}'^T H \boldsymbol{\xi}_{j,n} \cdot I(\xi_j = \lambda_n). \end{aligned} \tag{A.12}$$

Equation A.12 corresponds to a summation over two orthogonal states of the incident beam represented by $\xi_j = \pm 1$. Combining the two cases $m = 1, 2$ leads to the matrix form of equation A.12:

$$\begin{pmatrix} I(\xi_i' = 1) \\ I(\xi_i' = -1) \end{pmatrix} = U \cdot \begin{pmatrix} I(\xi_j = 1) \\ I(\xi_j = -1) \end{pmatrix}. \tag{A.13}$$

The entries of the matrix U are given by

$$\begin{aligned} U_{mn} &= \boldsymbol{\xi}_{i,m}'^T \cdot H \cdot \boldsymbol{\xi}_{j,n} \\ &= \left[\boldsymbol{e}_0 + \lambda_m \cdot \boldsymbol{e}_i\right]^T \cdot H \cdot \left[\boldsymbol{e}_0 + \lambda_n \cdot \boldsymbol{e}_j\right] \\ &= H_{00} + \lambda_m \cdot H_{i0} + \lambda_n \cdot H_{0j} + \lambda_m \cdot \lambda_n \cdot H_{ij} \\ &= \begin{pmatrix} 1 & \lambda_m \end{pmatrix} \cdot \begin{pmatrix} H_{00} & H_{0j} \\ H_{i0} & H_{ij} \end{pmatrix} \cdot \begin{pmatrix} 1 \\ \lambda_n \end{pmatrix}. \end{aligned} \tag{A.14}$$

Using the notation $|m\rangle$ for the m^{th} two-component standard unit vector allows to write

$$\begin{aligned} U &= \left[\sum_{m=1,2} |m\rangle \langle m|\right] U \left[\sum_{n=1,2} |n\rangle \langle n|\right] \\ &= \sum_{m=1,2} \sum_{n=1,2} |m\rangle U_{mn} \langle n| \\ &= \sum_{m=1,2} \sum_{n=1,2} |m\rangle \begin{pmatrix} 1 & \lambda_m \end{pmatrix} \cdot \begin{pmatrix} H_{00} & H_{0j} \\ H_{i0} & H_{ij} \end{pmatrix} \cdot \begin{pmatrix} 1 \\ \lambda_n \end{pmatrix} \langle n| \\ &= \left[\sum_{m=1,2} |m\rangle \begin{pmatrix} 1 & \lambda_m \end{pmatrix}\right] \begin{pmatrix} H_{00} & H_{0j} \\ H_{i0} & H_{ij} \end{pmatrix} \cdot \left[\sum_{n=1,2} \begin{pmatrix} 1 \\ \lambda_n \end{pmatrix} \langle n|\right] \end{aligned} \tag{A.15}$$

It can easily be verified that the sums over m and n evaluate to

$$\left[\sum_{m=1,2} |m\rangle \begin{pmatrix} 1 & \lambda_m \end{pmatrix}\right] = \left[\sum_{n=1,2} \begin{pmatrix} 1 \\ \lambda_n \end{pmatrix} \langle n|\right] = G. \tag{A.16}$$

With this result, equation A.13 reads:

$$\begin{pmatrix} I(\xi_i' = 1) \\ I(\xi_i' = -1) \end{pmatrix} = G \cdot \begin{pmatrix} H_{00} & H_{0j} \\ H_{i0} & H_{ij} \end{pmatrix} \cdot G \cdot \begin{pmatrix} I(\xi_j = 1) \\ I(\xi_j = -1) \end{pmatrix}. \tag{A.17}$$

The last step involves the application of the relation between the partial intensities and (beam) Stokes parameters given by equation A.10 – for both incident and scattered beam:

$$\begin{aligned} \begin{pmatrix} S_0' \\ S_i' \end{pmatrix} &= G \cdot \begin{pmatrix} I(\xi_i' = 1) \\ I(\xi_i' = -1) \end{pmatrix} \\ &= GG \cdot \begin{pmatrix} H_{00} & H_{0j} \\ H_{i0} & H_{ij} \end{pmatrix} \cdot G \cdot \begin{pmatrix} I(\xi_j = 1) \\ I(\xi_j = -1) \end{pmatrix} \\ &= 2 \cdot \begin{pmatrix} H_{00} & H_{0j} \\ H_{i0} & H_{ij} \end{pmatrix} \cdot \begin{pmatrix} S_0 \\ S_j \end{pmatrix}. \end{aligned} \tag{A.18}$$

From equation A.18, one immediately reads the final result:

$$T_{\mu\nu} = 2H_{\mu\nu} \qquad \forall \mu, \nu = 0, 1, 2, 3. \tag{A.19}$$

B Alternative polarization determination approaches

In section 5.3.3, the experimental φ_{det}-spectrum is fitted with a linear combination of Monte Carlo simulated φ_{det}-spectra to determine the Stokes vector $\boldsymbol{P}_{Lab}$ of the beam incident on the strip detector. Similar procedures that were discussed in the course of the present thesis, but not yet implemented, are the following:

- Instead of converting the Δn_x-Δn_y-spectra into φ_{det}-spectra and then fitting the latter, one could fit directly a linear combination of the simulated Δn_x-Δn_y-spectra to the experimental one.

- The Stokes vectors $\boldsymbol{S}_1, \ldots, \boldsymbol{S}_4$ defined in equation 5.37 are not linearly independent. To form a basis, three vectors are required, these can be for example $\boldsymbol{S}_1, \boldsymbol{S}_3$ and

$$\boldsymbol{S}_0 = \begin{pmatrix} S_{0,0} \\ 0 \\ 0 \\ 0 \end{pmatrix} \tag{B.1}$$

  where $\boldsymbol{S}_0$ represents an unpolarized beam. With these the components of $\boldsymbol{V}$ can be directly obtained from equation 5.39 as

$$\begin{aligned} V_0(\varphi_{det,i}) &= \frac{I'_0(\varphi_{det,i})}{S_{0,0}}, \\ V_1(\varphi_{det,i}) &= \frac{I'_1(\varphi_{det,i})}{S_{0,1}} - V_0(\varphi_{det,i}), \\ V_2(\varphi_{det,i}) &= \frac{I'_3(\varphi_{det,i})}{S_{0,3}} - V_0(\varphi_{det,i}). \end{aligned} \tag{B.2}$$

  The fit function is written as

$$I'(\varphi_{det,i}) = S_{0,Lab} \cdot \boldsymbol{V}^T(\varphi_{det,i}) \cdot \boldsymbol{P}_{Lab}. \tag{B.3}$$

  The absolute intensity $S_{0,Lab}$ is eliminated using the normalization to the total

number of experimental counts N:

$$N = S_{0,Lab} \cdot \left[\sum_{i'} \boldsymbol{V}^T(\varphi_{det,i'}) \right] \cdot \boldsymbol{P}_{Lab}, \tag{B.4}$$

where i' runs over all bins of the φ_{det}-spectrum. This gives the fit function

$$I'(\varphi_{det,i}) = N \cdot \frac{\boldsymbol{V}^T(\varphi_{det,i}) \cdot \boldsymbol{P}_{Lab}}{[\sum_{i'} \boldsymbol{V}^T(\varphi_{det,i'})] \cdot \boldsymbol{P}_{Lab}}, \tag{B.5}$$

which only contains the two fit parameters $P_{1,Lab}$ and $P_{2,Lab}$.

- The previously mentioned methods can be combined.

Danksagung

Abschließend möchte ich all denjenigen meinen Dank aussprechen, die diese Arbeit durch ihre Unterstützung erst möglich gemacht haben.
Der erste Dank gebührt meinem Betreuer Prof. Dr. Thomas Stöhlker. In zahlreichen Gesprächen hat er immer wieder Anregungen gegeben und mein physikalisches Verständnis erweitert.
Das in dieser Arbeit vorgestellte Experiment wäre ohne die Hilfe meiner Kollegen nicht durchführbar gewesen, daher ein großer Dank an Max Schwemlein, Tobias Gassner, Dr. Alexandre Gumberidze, Thorsten Groß, Dr. Sergiy Trotsenko, Dr. Renate Märtin und ganz speziell an Dr. Uwe Spillmann, der selbst zu den unmenschlichsten Uhrzeiten die Elektronik wieder zum Laufen brachte. Besonders bedanken möchte ich mich auch bei Dr. Günter Weber, der mich auch nach dem Experiment immer wieder unterstützt hat, indem er die Auswertung mit mir diskutierte, Simulationscode zur Verfügung stellte, unermüdlich Korrektur las und mir immer wieder einfache und schwierige physikalische Sachverhalte erklärte.
Selbstverständlich war es auch essenziell für das Experiment, dass von Seiten der Synchrotronstrahlungsquelle alles funktionierte, daher vielen Dank an Dr. Norbert Schell, der uns bei DESY mit Informationen versorgte und eventuell auftretende Probleme beseitigte.
Danke an Dr. Pierre-Michel Hillenbrand, der mir die Effizienzkurve des Germaniumdetektors übermittelt hat.
For the theoretical predictions, I would like to express my gratitude to Prof. Dr. Stephan Fritzsche, Dr. Vladimir Yerokhin and in particular to Dr. Andrey Surzhykov who not only provided both calculations and explanations always in a timely manner, but also joined several discussions on the results. Danke an Dr. Daniel Seipt, der mir beim Verständnis der Transfermatrix behilflich war.
Für das Korrekturlesen dieser Arbeit möchte ich mich bei Prof. Dr. Thomas Stöhlker, Prof. Dr. Siegbert Hagmann, Dr. Günter Weber und Dr. Uwe Spillmann bedanken.
Danke für die freundliche Büroatmosphäre an Dr. Günter Weber, Christoph Hahn, Stefan Ringleb, Ye Lin und Hao Ding.
Vielen Dank für die Hilfe bei administrativen Fragen – sowohl bei GSI als auch in Jena – an Stefanie Lüttges, Barbara Kirchner, Sandra Hundack, Cornelia Kabis und

Jessica Golm.
Schließlich möchte ich meiner Familie danken, die mich in allem unterstützt hat und dies weiterhin tut. Danke besonders an meine Frau, die mich immer begleitet.
Mein Dank geht auch an alle, die ich in der Aufzählung vergessen habe. Bitte vezeiht es mir!

Ehrenwörtliche Erklärung

Ich erkläre hiermit ehrenwörtlich, dass ich die vorliegende Arbeit selbstständig, ohne unzulässige Hilfe Dritter und ohne Benutzung anderer als der angegebenen Hilfsmittel und Literatur angefertigt habe. Die aus anderen Quellen direkt oder indirekt übernommenen Daten und Konzepte sind unter Angabe der Quelle gekennzeichnet.

Bei der Auswahl und Auswertung folgenden Materials haben mir die nachstehend aufgeführten Personen in der jeweils beschriebenen Weise unentgeltlich geholfen:

1. Die Vorbereitung des Experiments bei DESY erfolgte hauptsächlich durch Max Schwemlein, Dr. Uwe Spillmann und Dr. Renate Märtin.

2. Das Experiment bei DESY wurde zusammen mit Max Schwemlein, Tobias Gassner, Dr. Alexandre Gumberidze, Thorsten Groß, Dr. Uwe Spillmann, Dr. Sergiy Trotsenko, Dr. Günter Weber und Dr. Renate Märtin durchgeführt.

3. Als Beamline Scientist hat Dr. Norbert Schell das Experiment bei DESY unterstützt.

4. Die für die vorliegende Arbeit benötigten theoretischen Vorhersagen (Rayleigh-Streuung 175 keV auf Gold) wurden von Dr. Andrey Surzhykov, Dr. Vladimir Yerokhin und Prof. Dr. Stephan Fritzsche gemacht (Referenz [106]).

5. Der K-Schalen-Ionisationsquerschnitt von Gold bei 175 keV wurde von Dr. Andrey Surzhykov berechnet (Referenz [165]).

6. Die Parameter für die Effizienz des Germaniumdetektors habe ich von Dr. Pierre-Michel Hillenbrand erhalten, die entsprechende Messung wurde von Dr. Dariusz Banaś durchgeführt (Referenz [160]).

7. Der für die EGS5 Simulationen verwendete Code wurde von Dr. Günter Weber geschrieben (Referenz [162]).

8. Fachliche Diskussionen wurden mit den am Experiment beteiligten Kollegen (Punkt 2) sowie Dr. Andrey Surzhykov, Dr. Daniel Seipt und meinem Betreuer Prof. Dr. Thomas Stöhlker geführt.

9. Die vorliegende Arbeit wurde von Prof. Dr. Thomas Stöhlker, Prof. Dr. Siegbert Hagmann, Dr. Günter Weber und Dr. Uwe Spillmann korrekturgelesen.

Weitere Personen waren an der inhaltlich-materiellen Erstellung der vorliegenden Arbeit nicht beteiligt. Insbesondere habe ich hierfür nicht die entgeltliche Hilfe von Vermittlungs- bzw. Beratungsdiensten (Promotionsberater oder andere Personen) in Anspruch genommen. Niemand hat von mir unmittelbar oder mittelbar geldwerte Leistungen für Arbeiten erhalten, die im Zusammenhang mit dem Inhalt der vorgelegten Dissertation stehen.

Die Arbeit wurde bisher weder im In- noch im Ausland in gleicher oder ähnlicher Form einer anderen Prüfungsbehörde vorgelegt.

Die geltende Promotionsordnung der Physikalisch-Astronomischen Fakultät ist mir bekannt.

Ich versichere ehrenwörtlich, dass ich nach bestem Wissen die reine Wahrheit gesagt und nichts verschwiegen habe.

Jena, den

.....

Karl-Heinz Blumenhagen